NATURAL CONVECTION AND RADIATION HEAT TRANSFER IN SMALL ENCLOSURES WITH A NON-ATTACHED OBSTRUCTION

A Thesis

by

JIMMY L. LLOYD

Submitted to the Office of Graduate Studies of
Texas A&M University
in partial fulfillment of the requirements for the degree of

MASTER OF SCIENCE

December 2003

Major Subject: Mechanical Engineering

NATURAL CONVECTION AND RADIATION HEAT TRANSFER IN SMALL ENCLOSURES WITH A NON-ATTACHED OBSTRUCTION

A Thesis

by

JIMMY L. LLOYD

Submitted to the Office of Graduate Studies of
Texas A&M University
in partial fulfillment of the requirements for the degree of

MASTER OF SCIENCE

Approved as to style and content by

Dennis O'Neal
(Chair of Committee)

Warren Heffington
(Member)

Roy E. Hogan, Jr.
(Member)

Calvin Parnell, Jr.
(Member)

Dennis O' Neal
(Interim Head of Department)

December 2003

Major Subject: Mechanical Engineering

ABSTRACT

Natural Convection and Radiation in Small Enclosures with a Non-Attached Obstruction.

(December 2003)

Jimmy L. Lloyd, B.S., Texas A&M University

Chair of Advisory Committee: Dr. Dennis O'Neal

Numerical simulations were used to investigate natural convection and radiation interactions in small enclosures of both two and three-dimensional geometries. The objectives of the research were to (1) determine the relative importance of natural convection and radiation, and to (2) estimate the natural convection heat transfer coefficients. Models are generated using Gambit, while numerical computations were conducted using the CFD code FLUENT. Dimensions for the two-dimensional enclosure were a height of 2.54 cm (1 inch), and a width that varied between 5.08 cm and 10.16 cm (2 inches and 4 inches). The three-dimensional model had a depth of 5.08 cm (2 inches) with the same height and widths as the two-dimensional model. The obstruction is located at the centroid of the enclosure and is represented as a circle in the two-dimensional geometry and a cylinder in the three-dimensional geometry. Obstruction diameters varied between .51 cm and 1.52 cm (0.2 inches and 0.6 inches).

Model parameters used in the investigation were average surface temperatures, net total heat flux, and net radiation heat flux. These parameters were used to define percent temperature differences, percent heat flux contributions, convective heat transfer coefficients, Nusselt numbers, and Rayleigh numbers. The Rayleigh numbers varied between 0.005 and 300, and the convective heat transfer coefficients ranged between 2 and 25 W/m^2K depending on the point in the simulation. The simulations were conducted with temperatures ranging between 310 K and 1275 K on the right boundary. For right boundary temperatures above 800 K, the estimated error on the obstruction temperature is less than 6.1% for neglecting natural convection and conduction from the heat transfer analysis. Lower right boundary temperatures such as 310 K had significant contributions, over 50%, from heat transfer modes other than radiation. For lower right boundary temperatures, a means of including natural convection should be included. When a bulk fluid temperature and average surface temperature values are available, a time average heat transfer coefficient of 6.73 W/m^2K is proposed for simplifying the numerical calculations. In the transient right boundary temperature analysis, all modes of heat transfer other than radiation can be neglected to have an error below 8.1%.

DEDICATION

To my friends and family who have provided me with support and encouragement.

ACKNOWLEDGEMENTS

Funding for this project was provided by Sandia National Laboratories and the National Physical Science Consortium. I would like to thank the two organizations for their financial support.

Appreciation is extended to those who have helped me in successfully finishing my research. In particular, thanks go to Dr. Dennis O'Neal, Dr. Roy E. Hogan, Dr. Darryl James Dr. Warren Heffington, and Dr. Calvin Parnell. Dr. O'Neal not only helped me in my research, but also helped me in my academic and career endeavors. Dr. Hogan always had an encouraging word and some sort of advice on a different method or technique to try in the research. Successful use of the CFD code FLUENT was made possible by help from Dr. James, while Dr. Heffington and Dr. Parnell graced me with being on my committee and greeting me with friendly faces when I went to see them.

Praise is due to all the computer technical services at both Sandia National Laboratories and Texas A&M University. Whenever a problem was encountered, the staff would always be prompt in helping solve the problem.

TABLE OF CONTENTS

Page

CHAPTER

LIST OF FIGURES

Page

Page

LIST OF TABLES

CHAPTER I

INTRODUCTION

Coupling of natural convection and radiation heat transfer occurs in various engineering problems. One of the largest examples of natural convection and radiation coupling is the cooling of electronic components such as laptops, CD players, and cell phones. These listed devices put a premium on power conservation to reduce the drain on the battery power. Other examples of applications for coupled natural convection and radiation heat transfer include water quality management, environmental planning in coastal regions (Lei and Patterson 2002), furnaces (Yang 1986), solar energy (Fusegi et al. 1990a), crystal growth (Kohno and Tanahashi 2002), and room fires (Khalifa and Abdullah 1999). Many of these systems can be evaluated through experiments, but experiments can be costly, time consuming, and limiting on the variation that may be investigated.

Modern computers and simulation programs are used to augment experiments in evaluating and designing engineering systems. Because the simulation programs are benchmarked against experiments, sometimes only simulations are performed and experiments are avoided entirely. A problem with numerical simulations is the calculations can become complicated and computationally intensive for simulations where natural convection and radiation heat transfer are included. If one of the heat transfer modes (natural convection, conduction, or radiation) can be neglected, the

---

This thesis follows the style and format of *American Society of Heating, Refrigeration and Air-Conditioning Engineers Transactions*.

calculations may be simplified: reducing computation times and resources. A heat transfer mode may be neglected when its contribution is small compared to other heat transfer modes.

This study investigates the interaction of natural convection and radiation by examining system temperatures and heat flux. Values for temperatures and heat fluxes are used for defining percent differences, percent contributions, and heat transfer coefficient relations: each of which help in understanding the interaction. The model used for the investigation is a simple enclosure with an obstruction at the enclosure's centroid. The region around the obstruction is a fluid region: specified as nitrogen gas. Nitrogen is, in most situations, a non-participating gas, allowing for enclosure radiation (also known as surface to surface radiation) models to be used. Both two and three-dimensional enclosures are considered in order to determine the effect of the end boundaries on the overall heat transfer. A desirable aspect of two-dimensional simulations is that they take less time and resources than a three-dimensional simulation, but at a cost of ignoring the effect from the boundaries in the third dimension. To the author's knowledge, no research is available regarding natural convection and radiation effects on a mass disconnected from the boundaries in an enclosure. A literature review has provided information regarding natural convection and radiation in simple enclosures and enclosures with baffles.

1.1 Literature Review

The effects and contributions of natural convection and radiation have been studied in many forms over the years ranging from pure natural convection to natural convection with participating media. The importance of radiation heat transfer interacting with natural convection is generally well recognized (Raycraft et al. 1990). Radiation typically has a larger impact on natural convection than for forced convection (Krishnaprakas and Narayana 1999). This is due to forced convection having higher heat transfer coefficients than the relatively low values of natural convection. Ramesh and Venkateshan (1999) and Velusamy et al. (2001) found that radiative heat transfer was substantial at temperatures as low as 273 K in systems coupled with natural convection.

Researchers wishing to study pure natural convection have had to be very careful to avoid any effects from radiation. Duluc et al. (2003) used liquid nitrogen (temperature of 77 K) in experiments to determine the natural convection around a heated cylinder made of bronze. Thermo-resistive properties of bronze were used to determine the temperature of the cylinder. Hsieh and Yang (1996) conducted a time dependent natural convection experiment in a 150 x 50 x 60 mm rectangular enclosure. Two isothermal baths were used to set the temperatures on two opposing surfaces while the top and bottom surfaces were insulated. The front and rear sufaces were Plexiglas to allow for flow visualization of the silicon oil in the system. In the worst-case scenario, the system was placed under a temperature difference of 60°C (T_{max}–$T_{ambient}$ = 333 K - 273 K) with the ambient temperature at 25°C (maximum system temperature was estimated at around 333 K). Under these conditions, radiation from the hot surface to the cold surface was around two percent. Their results indicated that radiation contributed at relatively low temperatures even when precautions were taken to minimize radiation heat transfer.

Radiative heat transfer is categorized into two broad classifications: participating and non-participating media. Optical thickness (optical thickness = αL, where L is the length parameter and α is the absorptivity) is often cited as the criteria for whether the fluid is radiatively participating or not. If a fluid has a relatively large optical thickness, participating media calculations should be performed. Participating media reduces heat transfer at the boundaries because the fluid medium has a more uniform temperature than without participating media (Yang 1986). Borjini et al. (1999) looked at heat transfer between two concentric cylinders for different optical thickness. Conditions for the simulations were $(T_i - T_o) / T_o = 1$, $Pr = 0.7$, emissivity of the inner cylinder was 0.9, and the outer cylinder emissivity was 0.4. Increasing the optical thickness reduced the radiation heat transfer in a decreasing exponential manner.

Fluids such as air, nitrogen, and the inert gasses are essentially non-emitting and non-absorbing. These two characteristics make these fluids effectively non-participating. This criteria holds as long as temperatures are not high enough for either ionization or electronic excitation to occur, such as in the bow shock wave of a spacecraft in reentry (Mills 1999) or a nuclear explosion (Glasstone 1977). More studies appear to be available for enclosures filled with participating media than non-participating media. Ramesh and Venkateshan (1999) had similar findings in their literature review.

The majority of the research coupling natural convection and radiation heat transfer was for steady state conditions (Han and Baek 1999, Velusamy et al. 2001, Yang 1986, Yücel and Acharya 1990) where one surface was set as the “hot” surface while the other surface was set as the "cold" surface. Some research delved into transient natural convection and radiation interaction (Lei and Patterson 2002, Li and Durbetaki 1990). Li and Durbetaki (1990) found in their numerical simulations that retaining time derivative terms improved the rate of convergence of their simulations. Time derivative terms are differentials in the equations defined by a quantity change over a time change. They also found that after a certain mesh and time step size, the benefits of refining the mesh or decreasing time step sizes were offset by round off errors in the computer.

A typical system for simulating and conducting experiments for combined natural convection and radiation is a simple rectangular enclosure. Velusamy et al. (2001) performed two-dimensional steady state simulations in a simple rectangular enclosure with a non-participating media. The enclosure was described as a rectangle with width W and height H. The top and bottom surfaces were insulated while the left surface was set as the "cold" surface and the right surface was set as the "hot" surface. Rayleigh numbers ranged from 10^9 to 10^{12}, emissivity was between 0 to 0.9, initial temperature (T_o) was between 223 to 423 K, temperature difference (ΔT) between the hot and cold surface was ranged from 10 to 250 K, and the aspect ratio (enclosure height divided by length) varied from 1 to 200. In all of the simulations, air was the working fluid.

Results showed the surface-to-surface radiation modified the temperature on the top and bottom surfaces, which in turn affected the natural convection heat transfer in the enclosure. The top surface served to cool the fluid and then to re-emit the heat flux to other surfaces as radiation. The bottom surface absorbed radiation and heated the fluid by convection. Heating of the fluid along the bottom surface reduced the temperature difference between the hot surface and the boundary layer. Velocity and turbulence levels were enhanced by surface radiation resulting in higher convective heat transfer.

Fusegi et al. (1990a and 1990b) took the simple two-dimensional rectangular enclosure and expanded it to three-dimensions. Directions x and y were the original edges that formed a square, while z represents the expansion into three dimensions forming the cube. In the simulations, the cold temperature (T_C) was 278 K, and the hot temperature (T_H) was 833K. Fluid properties were taken at the reference temperature of 555 K. The height for the cube enclosure varied from $2.57x10^{-2}$ m to $4.66x10^{-1}$ m. Carbon dioxide was the working fluid with a Prandlt number of 0.68. Under these conditions, carbon dioxide was treated as a participating media. To account for the participating media, the P-1 radiation model was selected. This model uses spherical harmonic approximations for radiation intensity to predict both temperature and heat transfer (Ratzel and Howell 1982). A limitation to the model is the need for optically thick media: materials with appreciable αL values.

Several heat transfer models were considered by Fusegi et al. (1990a and 1990b) for running simulations. One option was to neglect radiation. Results show that the temperature field varied only slightly in the z direction, while the velocity field had weak secondary flows in the corners. Steady state solutions were not reached in the natural convection mode. With radiation included, steady state solutions could be acquired. The presence of the end surfaces and radiation had a large effect on the formation of three-dimensional flow fields. Secondary flows reached a higher intensity and the secondary vortex corners moved towards the symmetry plane. Surface radiation was attributed to causing variations in the temperature field near the back surface mainly due to an increase in the surface temperature. (Fusegi et al. 1990b)

Comparing the results obtained in two-dimensional simulations performed by Fusegi and Farouk (1989) and Fusegi et al. (1990b) three-dimensional work, heat transfer was approximately 15 to 20 percent less than for the two dimensional counterpart. End surface temperatures in the three-dimensional model reached a maximum value relative to all temperatures the surfaces will reach which reduced the total radiative flux from the isothermal surfaces and cause the difference in heat transfer. As for the flow fields, Lei and Patterson (2003) found that two-dimensional simulations were able to capture the major features of the flow development. For full understanding of the flow field and instabilities, three-dimensional simulations are needed.

Simulations and experiments available for simple enclosures provide large amounts of information, especially for systems that are simple enclosures such as windows, but do not adequately capture more complicated systems where there are partitions and obstacles. Room fire phenomena as discussed by Yang (1986) and the experimental model for the research being presented have blocking features and more complicated heat transfer interactions. Yücel and Acharya (1990) looked at a square enclosure containing baffles extending from the top and bottom surface (Figure 1) and a participating media.

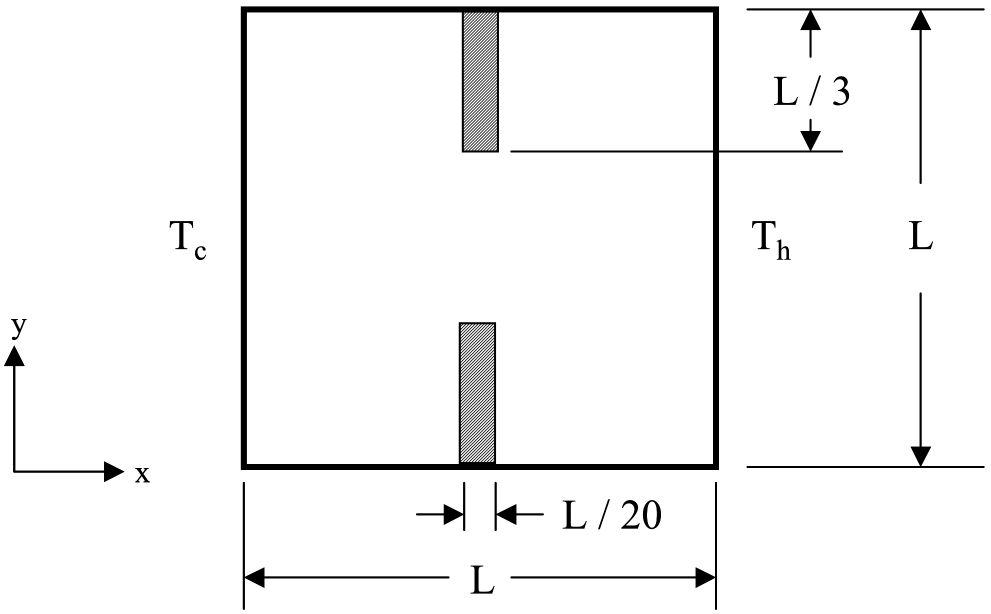

Figure 1: Simulation model used by Yücel and Acharya (1990)

Keeping the simulations generalized, the following non-dimensional numbers and ratios were used: temperature ratio (T_c/T_h) = 2/3, Pr = 0.71, and a Rayleigh base case = 3.3×10^5. For their simulations, radiation was the dominant heat transfer mode accounting for around 65-75% of the heat transfer on the hot surface and 45-65% of the heat transfer from the cold surface. Radiation interaction on the enclosure surfaces was important in influencing the temperature distributions near the baffles as well as the flow fields behind the baffles.

Changing the baffle position and type had a significant effect on the fluid flow fields. Khalifa and Abdullah (1999) studied natural convection in an enclosure with an aspect ratio of 0.5 and changeable partitions. The experiments were conducted using air as the working fluid and the Rayleigh number varied between 6×10^7 and 1.3×10^8. Changing the partition so that the air passage between the chambers was different in size or position changed the heat transfer in the system. A study similar to Yücel and Acharya (1990), conducted by Han and Baek (2000), had the baffles offset from each other (Figure 2). The left hand surface was selected as the "hot" surface while the right surface was the "cold" surface.

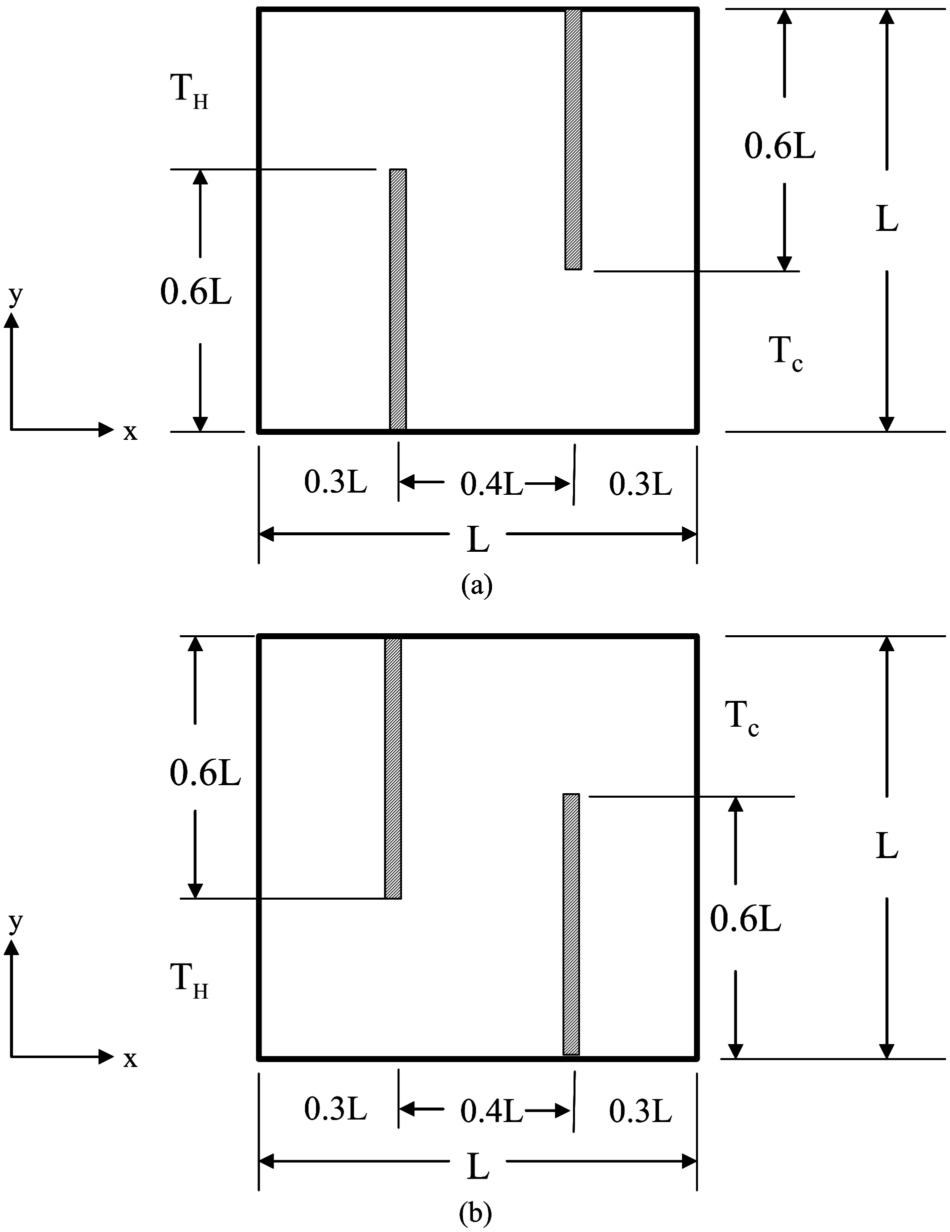

Figure 2: Case I (a) and case II (b) models from Han and Baek (2000)

Three distinct calculations were performed: radiation neglected, surface radiation only, and surface and gas radiation. In the calculations, the temperatures were held at T_c = 300 K and T_H = 900 K. Properties for the fluid were determined from the reference temperature of 600 K. The corresponding Prandlt number was 0.684 with a Grashof value held at 10^5.

Several points were concluded from the simulations. The first was surface radiation had a more important role in heat transfer than gas radiation. Also, the baffle configuration affected the flow and thermal fields. Case I models (Figure 2a) formed two distinct convective cells while the case II models (Figure 2b) had the two convective cells merge. In the radiation models, the temperature near the hot surface was more uniform but the region near the cold surface was more thermally affected than near the hot surface. Radiation was shown to be the main heat transfer mode near the hot surface, while convective heat transfer was the main heat transfer mode near the cold surface. This was because of blockage from the baffles.

The studies in this section create a basis regarding heat transfer in a system with natural convection and radiation. Furthering the investigation of the interaction of natural convection and radiation, the current work expands on the baffled enclosure work to examine combined natural convection and radiation for a geometry with an obstruction at the centroid of a small enclosure. Results come from numerical simulations performed in a commercially available computational fluid dynamics (CFD) code FLUENT.

1.2 Computational Tool

A variety of computational fluid dynamics (CFD) codes exist today, many of which are commercially available. One such CFD code is called FLUENT. FLUENT is a control volume, finite element method code that solves modeling equations of continuity, momentum, and energy that have been temporally and spatially discretized. The work presented in this thesis was done with FLUENT, version 6.0, which provided all the features needed for conducting an investigation of natural convection and radiation in small enclosures. Detailed descriptions of the features in FLUENT that make it attractive for use in this research are found in the following section. After which, a section containing basic mathematical formulations in FLUENT is provided.

1.2.1 FLUENT Capabilities

FLUENT is capable of performing an assortment of fluid dynamic calculations for different fluid types. Of interest are incompressible Newtonian fluids. In performing fluid flow calculations, the calculations may be either laminar or turbulent. Buoyancy induced flow calculations can also be performed. FLUENT calculates buoyancy induced flow calculations through one of the user selected buoyancy models. Three of these models are the ideal gas model, incompressible ideal gas model, and Boussinesq approximation model. The buoyancy induced flow can be coupled to the heat transfer to simulate natural convection.

FLUENT can model natural convection, conduction, forced convection (with the correct boundary conditions), and radiation. Radiation models include both participating media and enclosure radiation. The latter being the parameter that weighted heavily into the decision to use FLUENT. FLUENT also has several miscellaneous features that make it desirable for performing the simulations. Both two-dimensional and three-dimensional model geometries are allowed in FLUENT. Another flexibility of FLUENT is the inclusion of both steady state and transient solvers.

A nice feature in FLUENT is the built in post processor. This post processor allows a user to view results between calculation runs without having to perform specific file exports and open an external post processor to view results. Almost all basic post-processor features are included, allowing for extensive analysis of a problem from within FLUENT. The post-processor does have limited capabilities and some problems were encountered in using certain post-processing features. Overall, FLUENT is attractive for performing simulations and viewing the results.

1.2.2 Mathematical Formulations in FLUENT

Key modeling equations in FLUENT for fluid flow and heat transfer from natural convection and radiation are the conservation of mass, momentum, and energy. Coupled with the conservation equations are supporting equations such as radiation heat transfer, viewfactor, and density equations. These equations come in the form of partial differential and integral equations. Discretizing these equations is done via several numerical schemes which then allow the problem to be solved via an approximate set of equations.

Because FLUENT is a control volume, finite element program, a well defined control volume is crucial to formulating modeling equations in FLUENT. Using a Cartesian coordinate system, Figure 3 shows a representative control volume. Faces on the control volume are important because they are a key part of the discretization process. The τ_{ij} in the figure represent the shear forces on the i^th^ surface in the j^th^ direction. The labels for the shear forces on the back side have been left off, but they are the same as the front side terms but in the opposite direction. Terms shown as ρu_i are mass flow terms. The last significant term is the $\rho u_i u_j$ term, which is the momentum carried into the control volume by the flow. Body forces have been completely neglected from the diagram for clarity. Several of the terms on the figure are used in defining the following conservation equations.

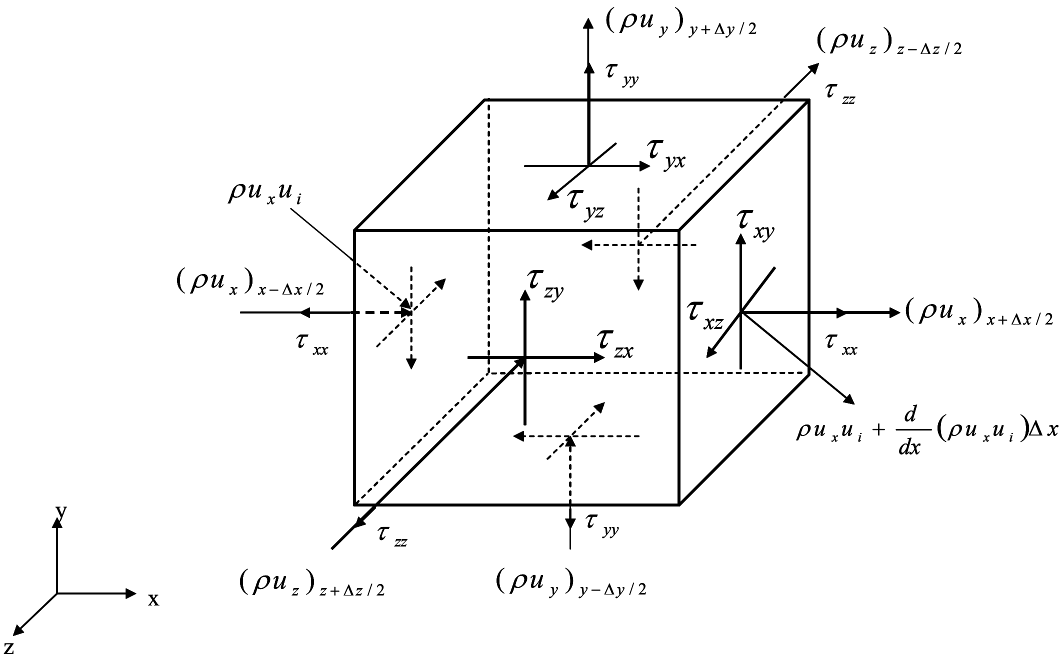

Figure 3: Control volume

The conservation of mass, also known as the continuity equation, may be written in the tensor format as:

$$\frac{\partial \rho}{\partial t} + \frac{\partial}{\partial x_i}(\rho u_i) = S \tag{1.1}$$

In this equation, ρ represents the fluid density, t is time, x_i is the direction tensor, u_i is the velocity in the direction i, and the S represents a source term. The source term is included for use with user-defined boundary conditions such as inlet and outlet mass flows.

Conservation of momentum for a control volume can be written in tensor form:

$$\frac{\partial}{\partial t}(\rho u_i) + \frac{\partial}{\partial x_j}(\rho u_i u_j) = \frac{-\partial P}{\partial x_i} + \frac{\partial}{\partial x_j}\left[\mu\left(\frac{\partial u_i}{\partial x_j} + \frac{\partial u_j}{\partial x_i}\right) - \frac{2}{3}\mu\frac{\partial u_l}{\partial x_l}\delta_{ji}\right] + B_i + F_i \tag{1.2}$$

where

$$\frac{\partial u_l}{\partial x_l} = \frac{\partial u_i}{\partial x_i} + \frac{\partial u_j}{\partial x_j} + \frac{\partial u_k}{\partial x_k} \tag{1.3}$$

B_i is the buoyancy force term, F_i is the body force term, P is pressure, and μ is the dynamic viscosity. The δ_ji is a Durac delta function that equals one when i equals j and zero otherwise. Physical meanings to the components are as follows. On the left side of equation (1.2), the first term is the time rate of momentum increase in the control volume while the second term is the net momentum carried out of the control volume by fluid flow ρu_j. The right hand side of equation (1.2) contains the pressure force, net viscous forces, buoyancy force, and body force.

To simplify calculations and help reach a converged solution faster, the incompressible ideal gas model is implemented. This model makes density a function of temperature and is represented in the equation:

$$\rho = \frac{P_{op}}{\Re T} \tag{1.4}$$

The symbol T is the fluid temperature, $\Re$ is the universal ideal gas constant divided by the molecular weight value, and P_{op} is the operating pressure specified by the user. This approximation holds valid as long as the actual density change and pressure changes in the system are small.

For a fluid, the energy equation can be written as:

$$\frac{\partial}{\partial t}(\rho E)+\frac{\partial}{\partial x_i}(u_i(\rho E+P))=\frac{\partial}{\partial x_i}\left(k_{eff}\frac{\partial T}{\partial x_i}-\sum_{j'}h_{j'}W_{j'}+u_j(\tau_{ji})_{eff}\right)+S_h \tag{1.5}$$

where

$$\tau_{ji}=\left(\mu\left(\frac{\partial u_i}{\partial x_j}+\frac{\partial u_j}{\partial x_i}\right)-\frac{2}{3}\mu\frac{\partial u_l}{\partial x_l}\delta_{ji}\right) \tag{1.6}$$

and

$$E=h-\frac{P}{\rho}+\frac{u_i^2}{2} \tag{1.7}$$

The enthalpy term, h, is approximated by:

$$h=c_pT \tag{1.8}$$

In equation (1.5), k_{eff} is the effective conductivity of the material, $W_{j'}$ is the diffusion flux of species j', τ_{ij} is the shear force. The two terms on the left side of the equation physically represent the time rate change in energy found in the control volume and net advection of energy out of the control volume with mass crossing the control surfaces. On the right side of the equation the first three terms are the energy transfer due to conduction, species diffusion, and viscous dissipation. S_h represents net radiation heat flux for the scope of the research.

Radiation can have several formulations. For a non-participating media, enclosure (known as surface-to-surface in FLUENT) radiosity equations are used.

Kirchoff's law, which states emissivity is equal to absorptivity ($\varepsilon = \alpha$), is used to simplify the problem. A graphical representation for surface radiosity in a simple, gray, three-body system is shown in Figure 4.

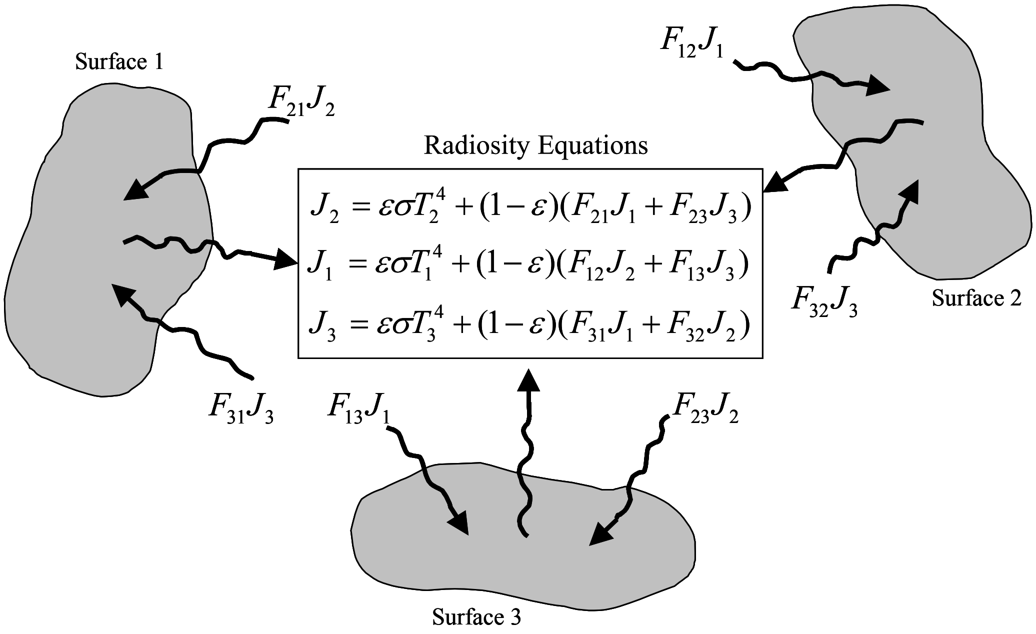

Figure 4: Three surface radiosity balance

These radiosity equations include a radiation viewfactor parameter. The definition for the viewfactor F_{ij}, as given by Incropera (1996), is the fraction of the radiation leaving surface i that is intercepted by surface j. This is graphically viewed in Figure 5.

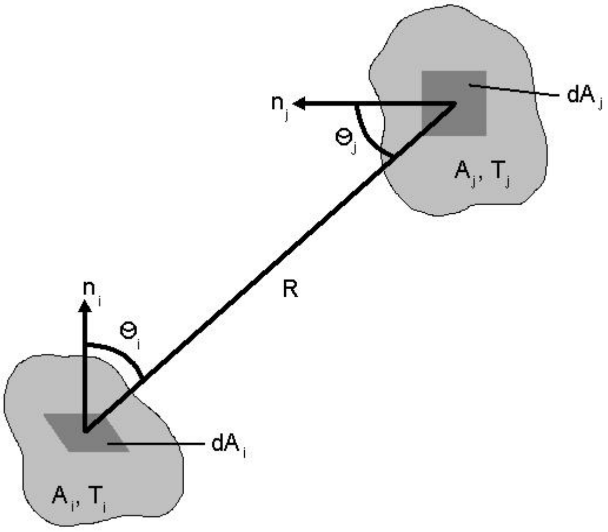

Figure 5: Viewfactor schematic

The radiosity equations in Figure 4 can be re-written in a generic form as:

$$J_k = \varepsilon_k \sigma T_k^4 + (1-\varepsilon)\sum_{j=1}^{N} F_{jk} J_j \tag{1.9}$$

This describes the radiosity from surface k into a system with N other surfaces, each of which is radiating its own amount. Expanding the equation for all the surfaces, the resultant system of algebraic equations can be written in a matrix format and solved.

Calculation of viewfactors is done using equation (1.10):

$$F_{ji} = \frac{1}{A_i} \int_{A_i}\int_{A_j} \left(\frac{\cos(\theta_i)\sin(\theta_j)}{\pi R^2} \right) \partial A_i \partial A_j \tag{1.10}$$

Subscripts i and j represent surface numbers. *A* is defined as the area of a surface and θ is the angle formed from the normal of the surface towards the other surface. The *R* term is the distance between the surfaces. These variables are shown on Figure 5. As the number of surfaces increase, the number of viewfactors calculated increases as N^2.

Efficient algorithms for computing viewfactors may reduce this effort to the order of N**ln*(N). A serious draw back to using radiosity equations is the computational resources needed to determine the viewfactors and the storage needed to save their values. Once viewfactors are calculated, enclosure radiation calculations are quite efficient.

Each of the modeling equations are presented in differential or integral form. FLUENT uses several methods to discretize the equation into approximate discrete algebraic equations. Temporal discretization is done through a simple differencing equation with three terms. Using ϕ as a generic value, the first order backward differencing version of the temporal derivative is written as:

$$\frac{\partial \phi}{\partial t} \approx \frac{\phi^{s+1} - \phi^{s}}{\Delta t} \tag{1.11}$$

While the second order discretization is written as:

$$\frac{\partial \phi}{\partial t} \approx \frac{3\phi^{s+1} - 4\phi^{s} - \phi^{s-1}}{2\Delta t} \tag{1.12}$$

In these equations the superscripts represent indexes for a specific time and the Δt is the time step duration.

Spatial derivatives are formulated by integrating the steady state modeling equations over the control volume. An example from the FLUENT5 User Guide is presented. Equation (1.13) is the steady-state conservation equation for the transport of a scalar quantity ϕ.

$$\rho \phi v \cdot dA = \Gamma_{\phi} \nabla \phi \cdot dA + S_{\phi} dV \tag{1.13}$$

Integrating equation (1.13) over the control volume and breaking into summations results in equation (1.15).

$$\oint \rho\phi v \cdot dA = \oint \Gamma_\phi \nabla\phi \cdot dA + \int_V S_\phi dV \qquad (1.14)$$

$$\sum_f^{N_{faces}} \phi v_f A_f = \sum_f^{N_{faces}} \Gamma_\phi (\nabla\phi)_n A_f + S_\phi V \qquad (1.15)$$

In these equations, the subscript, *f,* represents a face and N_{faces} is the total number of faces. For tetrahedral meshes, N_{faces} is equal to four, while hexagonal meshes have an N_{faces} value of six. The values for the area and volume come from the control volume formulation. Integration in equation (1.14) occurs at each surface of the control volume, while the volume is over the entire control volume domain.

Two other parameters of FLUENT mathematic modeling are parameter storage and under-relaxation. Discrete values are stored in the center node of the control volume. Because the discretizing of the modeling equations is done at the surfaces, interpolation between adjacent cells the surfaces separate is done to find the surface value. Several methods for interpolating have been developed: first-order upwind scheme, second-order upwind scheme, power-law scheme, and the QUICK scheme. To aid in obtaining a converged solution, it is sometimes necessary to use a relaxation factor. This factor affects the change from the old value to a new value by multiplying the change in a value by a set quantity. Equation (1.16) shows how the new value φ is equal to the old value ϕ plus the relaxation factor times the change in φ, Δ φ.

$$\phi_{new} = \phi_{old} + r\Delta\phi \qquad (1.16)$$

Where φ represents a generic variable and *r* is the relaxation factor.

1.3 Objectives

The main objectives of this research are: (1) to determine the relative importance of radiation and natural convection on an obstruction centered in a small enclosure, and (2) to estimate the natural convection heat transfer coefficients. FLUENT is used to perform the numerical calculations used to estimate the bulk natural convection and radiation heat transfer as well as to estimate the convective heat transfer coefficients. The resulting data and analyses are used to determine whether more simplified heat transfer models can be used such as neglecting a heat transfer mode.

CHAPTER II

COMPUTATIONAL MODELS

Computational models used for this study consist of three parts: the geometry, time stepping, and meshing. Each of these parts has a significant impact on the results. The geometry affects how the heat transfer modes interact, while time stepping and meshing affects the simulation's numerical accuracy and convergence characteristics. Material properties also affect the heat transfer, but they are not addressed in this research. In this chapter, the geometry is discussed in detail first. Time stepping and how time steps are selected are then discussed. Finally, the chapter concludes with details regarding meshing.

2.1 Geometry

Both two-dimensional and three-dimensional geometries are considered. The difference between the two categories is the three-dimensional model has a finite depth and end surfaces; the two-dimensional model assumes an infinite depth and the end surfaces effects are negligible. This change has a profound impact on the simulation, particularly in meshing, calculating viewfactors, and most importantly, solving the problem. These issues are discussed in the meshing section at the end of this chapter and the results chapter. The basic shape of the enclosure is a rectangle with a circular obstruction at the rectangle's centroid (Figure 6 and Figure 7).

Referencing the geometries of both the two-dimensional and three-dimensional models is done via the aspect ratio (AR) formed by taking the height and dividing it by

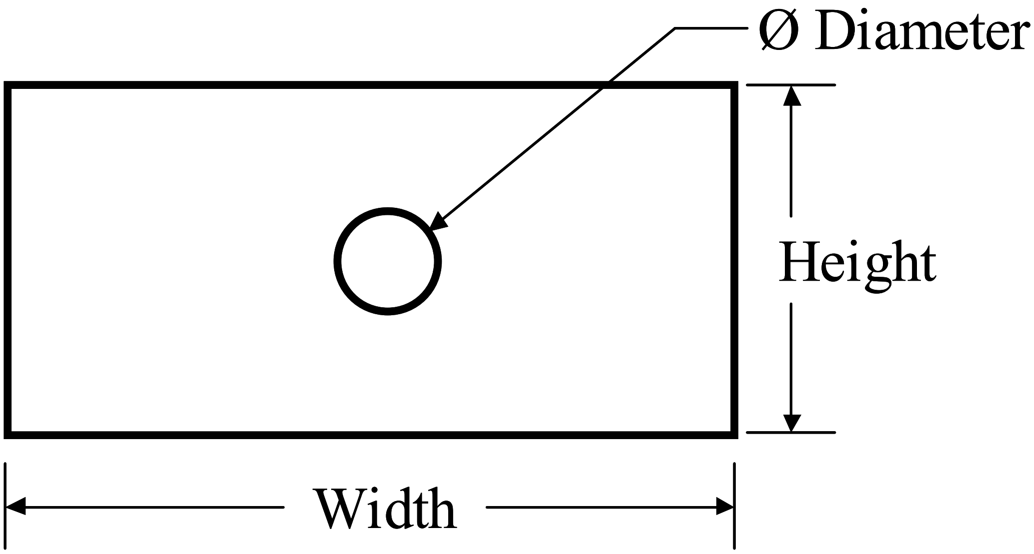

Figure 6: Two-dimensional enclosure for temperature and aspect ratio simulations

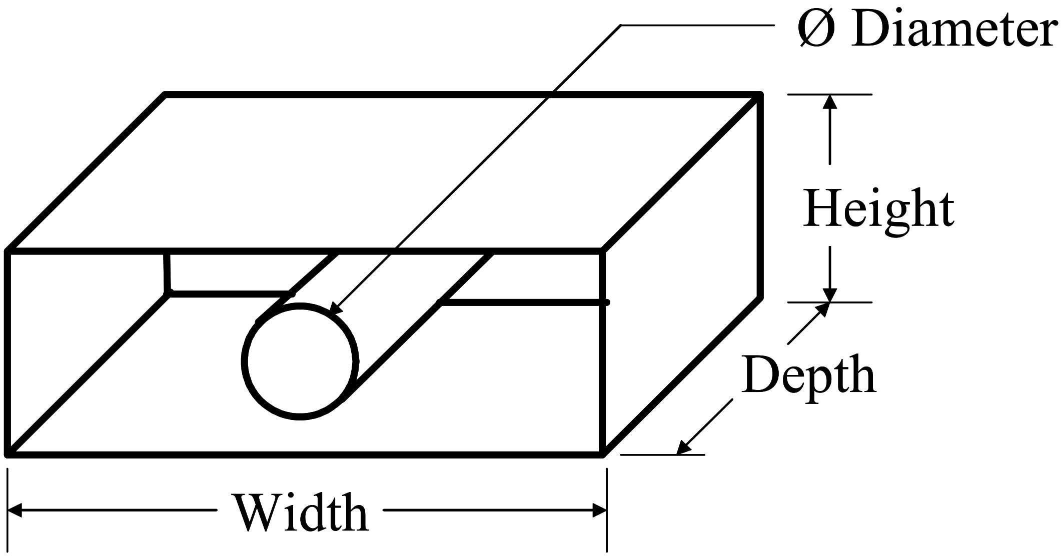

Figure 7: Three-dimensional enclosure for temperature and aspect ratio simulations

the width. Definitions for the height and width are seen on Figure 6 and Figure 7. Expanding on the classification system is the shaft ratio (SR), which is defined as the shaft diameter divided by the enclosure's height. The depth on the three-dimensional enclosure is kept constant; therefore it did not need any method to reference it.

Defining the aspect and shaft ratios aids in describing the enclosure. Aspect ratios are varied from 1/4 to 1/2. Three shaft ratios are used: SR=1/5, SR=2/5, and SR=3/5. The majority of the simulations are performed at an aspect ratio of 1/3 and a shaft ratio of 2/5. Placing physical numbers to these ratios, the height is kept constant at 2.54 cm (1 inch), the depth is kept at 5.08 cm (2 inches) on the three-dimensional model, and the width is varied between 5.08 cm and 10.16 cm (2 inches and 4 inches). The shaft diameter varies between .51 cm and 1.52 cm (0.2 inches and 0.6 inches). Corresponding dimensions for the most common simulation configuration are a height of 2.54 cm (1 inch), width of 7.62 cm (3 inches), and shaft diameter of 1.02 cm (0.4 inches).

Several reasons exist for the selection of these dimensions. The primary reason is that these dimensions correspond to the sizes of typical components encountered in a control system used at Sandia National Laboratories. A second reason is the small size keeps the length aspect on the Reynolds number low, which helps the flow to remain laminar. Laminar flow is important in simplifying the calculations. Using nitrogen gas properties and a length scale of 2.54 cm, the velocities would need to be in excess of 280 m/s for the flow to be turbulent, assuming turbulence occurs at Reynolds number of $5*10^5$. This velocity is very unlikely to occur in a buoyancy driven flow problem. The calculation of the flow velocity is found in Appendix A.

Selection of an obstruction with a circular cross section stems from many actual enclosures obstructions possessing circular cross sections. Some examples include springs, shafts, wires, and tubes for fluid flow. Representing all obstruction in the enclosure as a simple object with a circular cross section simplifies the calculations and makes it where the obstruction does not radiate to itself. Using a circular cross section also simplifies model creation. Inside the enclosure has also been simplified by removing any rounds or fillets, which may be present after metal working or machining to create the part, leaving an interior with 90° corners. Effects from the rounds and fillets have been assumed to be insignificant.

2.2 Time Stepping

Selection of an appropriate time step is crucial to obtain proper convergence without performing excessive and time consuming calculations. The FLUENT5 User Guide provides some guidance in the selection of time steps for reaching steady state conditions. From the manual, the times steps should be:

$$\Delta t \approx \frac{L}{4\sqrt{g\beta\Delta TL}} \tag{2.1}$$

Where L is the length scale, g is gravity, β is the thermal expansion coefficient, and ΔT is the change in temperature for overall problem. For L = 0.0254 m, g = 9.81 m/s^2, β = 0.0009 1/K, and ΔT = 800 K; the time step time is estimated to be about 0.0079 seconds. Even at a temperature difference of ΔT = 1 K, the time steps are estimated to be less than 0.5 seconds.

Desired transient simulations of about one hour are required for this study. The time steps estimated by equation (2.1) for a converged steady state solution were taken as starting points for time steps for a transient solution. To determine acceptable transient time steps, a simulation is run for an arbitrary time-step until a certain end time is reached, the solution is saved to a file and the starting conditions would be restored. A simulation is run using a larger time step to reach the same end time. The results of the two simulations are compared, and if the results are within a specified tolerance, less than 0.25 K, the smaller time step is considered acceptable and its results are used as the starting point for the next time-step. Table 1 shows the final time-stepping scheme selected for running the simulations. Time steps are set up to allow for data saves at specific times.

2.3 Meshing

An acceptable mesh is crucial in reaching a correctly converged solution that captures all the key parameters of a simulation. For the current simulations, enough nodes need to be placed near the boundaries to capture boundary layer flow, as well as the temperature gradient. Too many nodes in the system may increase the computational resources and time without providing additional resolution. For these two reasons, a mesh fine enough to accurately capture the appropriate details of the fluid flow and heat transfer, but coarse enough not to be overly computationally intensive is desired.

Table 1: Simulation Time Steps and Data Save Times

Time-Step [s]	Number of Steps	End Time [s]
0.00714	14	0.09996
0.00789	190	1.59906
0.008	310	4.07906
0.024	350	12.47906
0.042	300	25.07906
0.065	310	45.22906
0.08	311	70.10906
0.15	316	117.50906
0.2	313	180.10906
0.6	258	334.90906
0.85	200	504.90906
1	100	604.90906
1.35	297	1005.85906
1.6	250	1405.85906
1.25	400	1905.85906
1.25	400	2405.85906
2	250	2905.85906
2	250	3405.85906
1.5	200	3705.85906

Refined meshes are good for capturing details around boundaries, or anywhere the mesh is refined around, while also providing a means of reducing the total number of nodes for the overall simulations. Lei and Patterson (2002) found that a mesh size of 81 X 61 X 41 (202581 elements) was sufficient for the purpose of determining flow development in an enclosure of 0.6 m X 0.3 m X 0.06 m (23.6 inches X 11.8 inches X 2.36 inches). Element side lengths are 0.74 cm X 0.49 cm X 0.15 cm (0.29 inches X 0.19 inches X 0.06 inches). Complications in meshing and running the simulations cause the two-dimensional and three-dimensional models to be meshed differently.

Two-dimensional meshes have a value of 0.0008 m for the major element side length. For the two-dimensional models, this creates meshes ranging from 31 X 31 to 127 X 31. To increase the accuracy of the simulation and capture the boundary layer flows better, a refined grid is implemented for a depth of 0.003 m (0.118 inches) from the boundaries. This refined area has ten element layers with a growth ratio of 1.2 extending from the boundary. Figure 8 shows the resulting mesh on a two-dimensional model created with GAMBIT.

A convergence study is used to determine if a particular mesh is at an acceptable refinement for simulation convergence and if changes to the mesh affect the solution significantly. Because of the refined mesh, mesh parameters are given as element side lengths, depth of refinement, number of refinements and growth ratio instead of a uniform mesh format of elements X elements X elements. Element side lengths used in the convergence study are 0.0005 m, 0.0008 m, 0.001 m, and 0.002 m (0.0197 inch, 0.0315 inch, 0.0394 inch, and 0.0787 inch). The refined mesh of depth 0.003 m (0.118 inch), 10 element layers, and growth ratio 1.2 was used on all meshes. A special case of

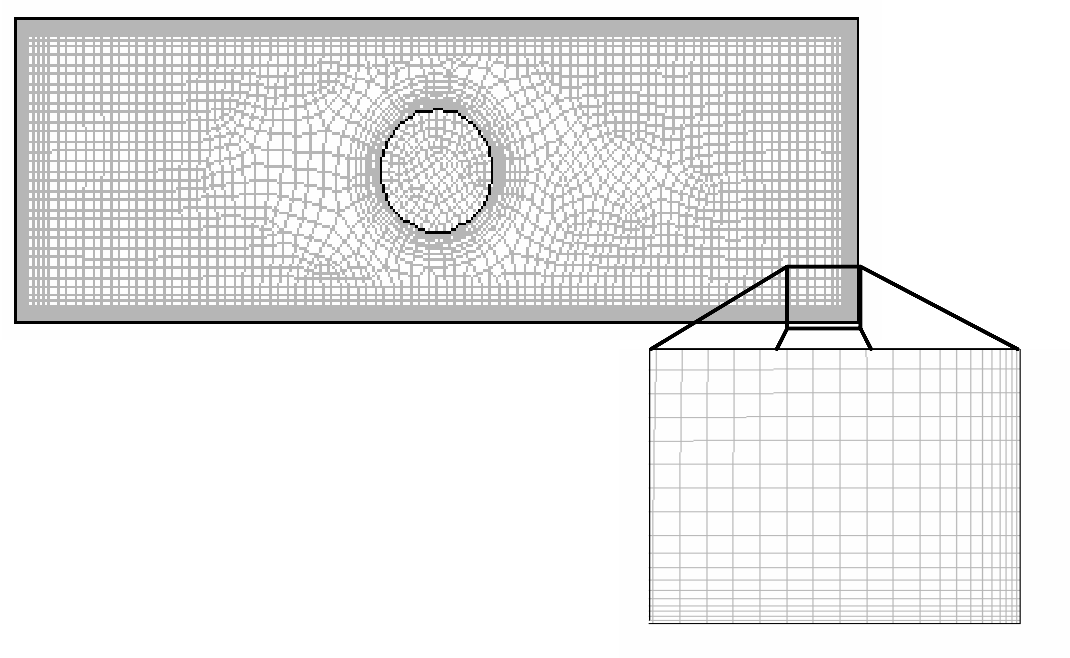

Figure 8: Two-dimensional model created and meshed in GAMBIT, lower right corner zoomed to show refined mesh with 1.2 growth ratio

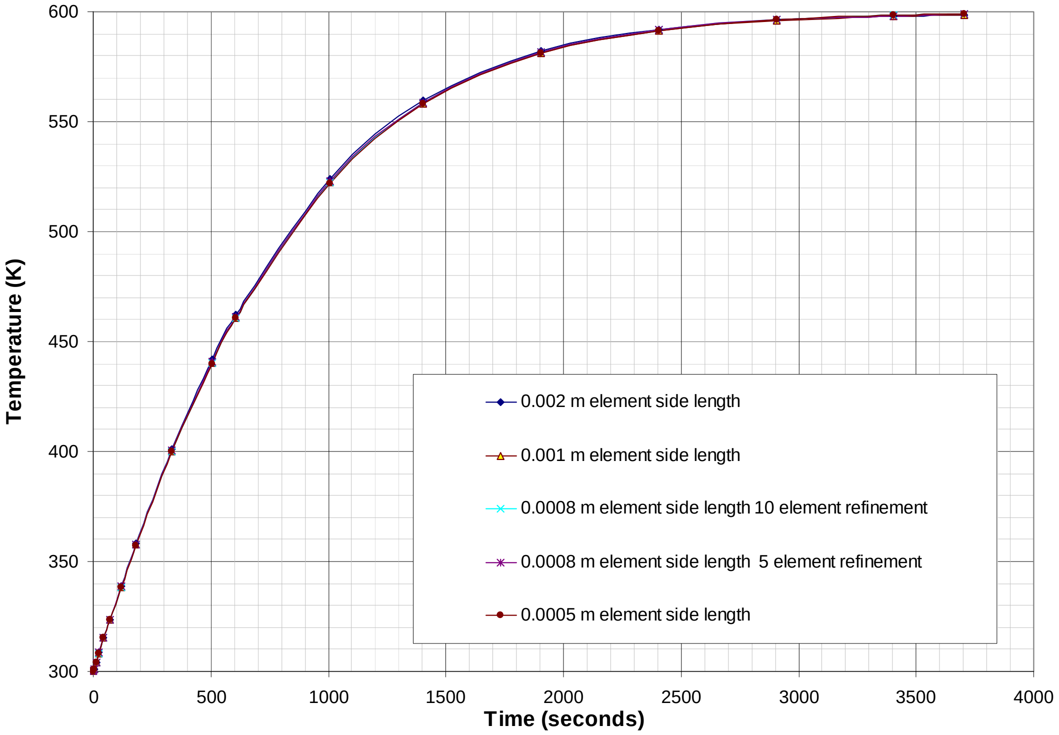

Figure 9: Convergence study results for average obstruction surface temperature. All meshes have 10 element refined mesh unless otherwise stated

element size 0.0008 m (0.0315 inch), 5 element layers, and growth ratio of 1.2 is also included. The average surface temperatures of the obstruction are nearly identical for all the simulations (Figure 9). Results from the special case mesh are not as clean to view around the boundaries because there are fewer nodes. This highlights the use of the 10 element layer for 0.003 m (0.118 inch) refined mesh.

Convergence study results show that the selected mesh is sufficient to produce converged results. The refinement depth size is limited by boundaries facing each other, like the obstruction and the top or bottom boundary. Increasing this depth and the number of division elements would capture the boundary flow better, but the current refinement is sufficient to capture the boundary layer addiquately. Final node numbers for the selected mesh range from 3462 nodes to 6358 nodes for the two-dimensional models.

Meshing the three-dimensional models requires taking the computational resource requirements for the simulation into account. Each face of an element on a boundary is included in a viewfactor calculation. For three-dimensional models, the number of mesh elements on a boundary can be extensive. To help reduce the computation demands, FLUENT allows adjacent mesh elements to be lumped together and only a single viewfactor calculated for the group. Even with this simplification, viewfactor calculations can become unwieldy in terms of computation time and storage. Also, for all the nodes on a two-dimensional plane, the number has to be multiplied by the number of nodes in the third dimension. From problems associated with mesh and node numbers, an element side length of 0.002 m (0.0787 inch) is used with a refinement of 10 elements layers for a depth of 0.003 m (0.118 inch) and growth ratio of 1.2. 86613 nodes result from using this mesh on a model with the dimensions of 2.54 cm X 7.62 cm X 5.08 cm (1 inch X 3 inches X 2 inches).

CHAPTER III

BOUNDARY CONDITION AND MODELING SPECIFICATIONS

Materials, boundary conditions, and tolerances affect the type and manner in which a simulation is conducted. Boundary conditions are crucial in CFD codes to specify how to perform calculations at the boundary. Lastly, the iteration tolerances determine when a calculation is considered converged and the next iteration may commence. Each of these issues is discussed below.

3.1 Material Selection

Three entities in this research require material properties to be specified for them: the fluid, the obstruction, and the outside boundaries.

3.1.1 Fluid

Nitrogen gas is selected as the working fluid within the enclosure. For simulation purposes, the density of nitrogen is calculated using the derivation of the ideal gas law given in equation (1.4). Other properties for nitrogen are summarized in Table 2 on page 33. Nitrogen was selected for the fluid because it is an inert gas that is often used in sealed electro-mechanical devices and is a non-participating media for radiation. For nitrogen gas to participate in radiation, the nitrogen molecules must be excited to the ionized state. Bond et al. (1965) showed nitrogen is effectively non-participating.

Total volume rate of emission in all directions is given by Bond et al. (1965).

$$4\pi P_r = 4\mu_p \sigma T^4 \tag{3.1}$$

Here, P_r is the volume rate of emission, μ_p is the Planck mean opacity defined in equation (3.2), σ is Boltzmann's constant of $5.6687*10^{-8}$ W/m^{2}K^4, and T is the gas temperature.

$$\varepsilon = a\mu_p \tag{3.2}$$

Nitrogen gas has an emissivity (ε) value of 0.01 and a is a correction factor that generally has a value of 1.8. Solving equation (3.2) for μ_p and substituting into equation (3.1) yields an equation for the total volume rate of emission (TVR):

$$TVR = 4\pi P_r = 4\frac{\varepsilon\sigma T^4}{a} \tag{3.3}$$

Substituting in the values for the constants produces:

$$TVR = 1.26*10^{-5}T^4 \tag{3.4}$$

The amount of radiation predicted for a steel surface at temperature T is given by $q=\varepsilon\sigma T^4$, where ε is the emissivity for steel. Comparing the amount of radiation the steel should emit and the gas should absorb for a given T shows the gas would absorb 36 times less radiation than the surface emits. The difference in absorbed radiation to radiation emitted is an appreciable, helping confirm statements that nitrogen is non-participating, and the use of the enclosure radiation model is supported.

3.1.2 Solids

Material selection for the solids is generic steel. This material is applied to both the external boundaries and the obstruction. Logic behind the selection of generic steel is it is a possible material in components of interest. Also, for the model under investigation, steel has a high enough thermal conductivity to allow for lumped capacitance to be assumed on the obstruction. This is shown below.

Lumped capacitance is assumed when the Biot number is less than 0.1. The Biot number is defined as:

$$Bi = \frac{hL_c}{k} \tag{3.5}$$

where

$$L_c = \frac{Volume}{SurfaceArea} \tag{3.6}$$

The thermal conductivity of the generic steel is 16.27 W/m-K (other properties listed in Table 2), while the heat transfer coefficient for natural convection can be assumed to be between 5 and 20 W/m^{2}K. The diameter of the obstruction can be assumed to be 1.016 cm (0.435 inches) for this exercise. Using the higher end value for the heat transfer coefficient to get a conservative estimate, the Bi number comes out to be 0.0034. This is less than 0.1 so lumped capacitance is a valid assumption. The lumped capacitance model helps in presenting results, and is not important in the numerical simulations. Results for the research are obtainable even when the lumped capacitance model does not work.

Table 2: Material Properties

Properties	Symbol	Units	Material	
			Nitrogen	Steel
Density	ρ	kg/m^3	Ideal gas approximation	8030
Specific Heat	c_p	J/kg-K	1040.67	502.48
Viscosity	μ	kg/m-s	$1.663*10^{-5}$	--
Thermal Conductivity	k	W/m-K	0.0242	16.27
Molecular Weight	M	kg/kmol	28.0134	--

3.2 Boundary and Initial Conditions

Temperatures, heat fluxes, and mass flow rates all can be used for boundary conditions. To run the two-dimensional simulations, four boundary conditions and one initial condition are needed. For the initial condition, the system starts out at a uniform temperature of 300 K. The four boundary conditions are applied directly to the external boundaries (Figure 10).

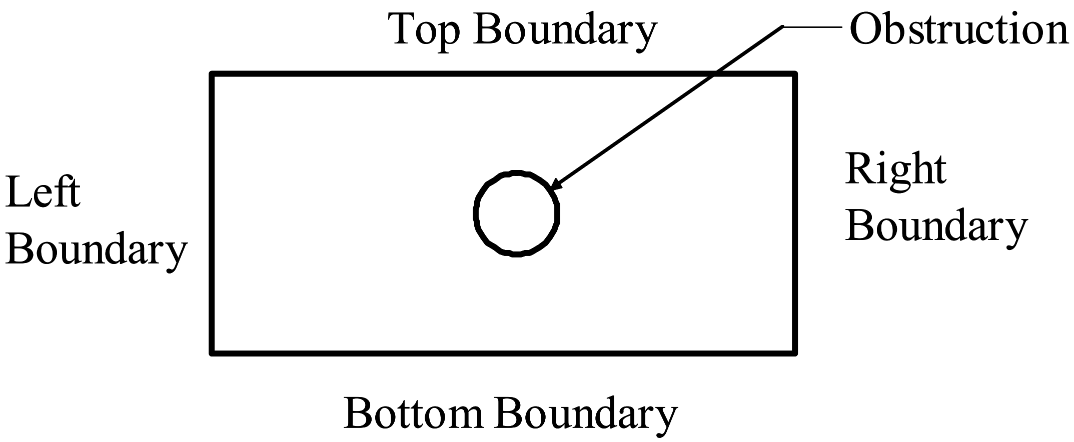

Figure 10: Boundary labeling scheme

Running the three-dimensional simulations requires six boundary conditions and one initial condition. A boundary condition is needed for each external boundary in the enclosure. The labels for the three-dimensional model are the same as the two-dimensional model with the addition of the labels front boundary and back boundary. Boundary conditions are discussed below.

3.2.1 Right Boundary

The right boundary has a specified temperature. This temperature represents heating caused by an external environment such as a fire. Because an object in an abnormal environment is not expected to have a constant temperature for all times, the temperature on the right boundary is adjusted between 310 K and 1275 K for different simulations. The upper end temperature is representative of the temperature in a pool fuel fire.

Specific temperatures are specified for each simulation. The two-dimensional simulations for the 1/3 aspect ratio and 2/5 shaft ratio are run at set right boundary temperatures of 310, 500, 600, 800, 950, 1100, and 1275 K. This temperature range covers temperatures the test model should encounter when exposed to a fire radiating at 1275K. The changing aspect ratio simulations are kept at a constant 600 K to allow for independent variables to be minimized and the solutions compared more directly to determine the effect of the aspect ratio. Three-dimensional simulations are run using only the right boundary temperatures of 310, 500, 600, 950, and 1275 K. A final simulation is run using a 40 K/min transient temperature from 310 K to 1275 K on the right boundary. This approximates how the objects boundary temperature is expected to change over time if in a heating environment.

3.2.2 Other Boundaries

The other boundaries, those excluding the right boundary, are assumed to be adiabatic. Reasoning behind making all the boundaries except the right boundary adiabatic is the enclosure is encapsulated in foam insulation, which should prevent significant amounts of energy transfer from the system though these boundaries.

3.3 Tolerances and Relaxation Factors

Most CFD programs, including FLUENT, have built in default tolerances and relaxation factors. The tolerances are needed by the solver to determine when a calculation for a time step is converged and the solver can go on to the next time step. Relaxation factors are used to reduce the amount of change to the original solution estimate to get a new solution estimate by individual iteration calculations. Relaxation reduces the chances for the proposed solution to overshoot the actual solution. Sometimes, overshoots can be so severe, numerical methods diverge. A mathematical formulation for the numerical relaxation of the quantity ϕ is given in equation (3.7).

$$\phi_{new} = \phi_{old} + r\Delta\phi \tag{3.7}$$

In this equation, ϕ is an arbitrary quantity and r represents the relaxation factor. The change in ϕ calculated is adjusted by the relaxation factor, and a new value for ϕ is determined.

FLUENT uses an aggressive set of default relaxation factors, many set to unity. What is considered an aggressive relaxation factor is problem dependent. It is felt by the author and several experienced engineers who use FLUENT that the default tolerances in FLUENT are too aggressive for transient natural convection simulations. Therefore, relaxation factors in FLUENT were reduced. Three notable quantities that had their relaxation factors reduced were density, body force, and momentum. The density relaxation factor changed from 1 to 0.6. Body force likewise was changed from 1 to 0.6. The body force is an important quantity for the pressure because a body force averaged discretization method is used. Momentum was set to have the largest relaxation with the relaxation constant changed from 0.7 to 0.4.

Tolerances, like relaxation factors, are important in reaching a solution. FLUENT's default tolerances are loose, usually with a value of only 0.0001. Running simulations with these tolerances allows for large reductions in simulation times, but at a cost of not converging to the true solution. For the present simulations, there are four critical categories that need the tolerance tightened below the default tolerances. These categories are continuity, velocity, energy, and radiation. New tolerances for the continuity and velocities are $1*10^{-6}$. Velocities can be broken down into the x, y, and z components, each requiring a smaller tolerance. Energy and radiation had the tolerances reduced to $1*10^{-8}$. Setting the proper materials, tolerances, relaxation factors, and boundary conditions, the simulations were considered ready to run.

CHAPTER IV

SIMULATION RESULTS

This chapter presents the simulation results from FLUENT. The format of this chapter starts with a description of the analysis and then provides a two-dimensional example using the base boundary condition temperature of 600 K on the right boundary, aspect ratio 1/3, and shaft ratio 2/5. Following the sections describing the analysis, results for the entire project are presented. Analysis is essentially the same for all the simulations, including the three-dimensional simulations. Two extra boundaries and a volume averaging for the bulk temperature are the only difference between the three-dimensional and two-dimensional analysis.

4.1 Detailed Analysis and Description

Parameters analyzed are the obstruction's average surface temperature, percent difference in surface temperature, percent heat flux, fluid flow fields, temperature plots over the entire model, and heat transfer coefficients for the obstruction and right boundary. As indicated, much of the attention is placed on the obstruction. This is because in design and analysis, the main concern is the obstruction, which represents a component housed in the enclosure. Averaged values, such as heat transfer coefficients, are presented using area averaging methods.

4.1.1 Average Surface Temperature on the Obstruction

Surface temperature plots provide a convenient way to compare the results from the different heat transfer simulations. Three heat transfer mode simulations are run: (1) all heat transfer modes included, (2) buoyancy forces neglected, and (3) both conductivity and buoyancy forces neglected. By turning off buoyancy forces, natural convection is removed from the simulation. Turning off conduction is done by setting the fluid's conductivity to 0, creating a simulation with only surface radiation.

Simple comparisons are only the first of several reasons to look at average surface temperature. A key reason to look at average surface temperature is the ease of extracting the data. Node values on the boundaries are easily accessed either through a post processor or an extraction program. Because the obstruction can be effectively considered a lumped mass system, its average surface temperature can also be assumed to be its average temperature. This assumption holds true up to the high temperature (1275 K), which is seen by comparing the average surface temperature to the average volume temperature. At the high temperatures, a slight gradient forms at the right side of the obstruction due to high heat fluxes from enclosure radiation. The average surface temperatures are also used in calculation for heat transfer coefficients.

Average surface temperatures presented are formulated using area averaging. Mesh faces on surfaces and boundaries are used to represent discrete areas. Each of the mesh elements also have a temperature associated with them. The discrete area and temperature are multiplied and summed up along the length of a surface or boundary and divided by the total area of the surface or boundary. Mathematically this is represented as:

$$T_{avg} = \frac{\sum_{i=1}^{n} T_i A_i}{\sum_{i=1}^{n} A_i} \tag{4.1}$$

Where T_{avg} is the average temperature, T_i is a temperature for a given element along the surface or boundary, and A_i is the area for the element along the surface or boundary.

For the two-dimensional simulation with the right boundary temperature set at a constant temperature of 600 K, aspect ratio 1/3, and shaft ratio 2/5, the average surface temperature for a transient time simulation extending for a little over one hour is presented in Figure 11.

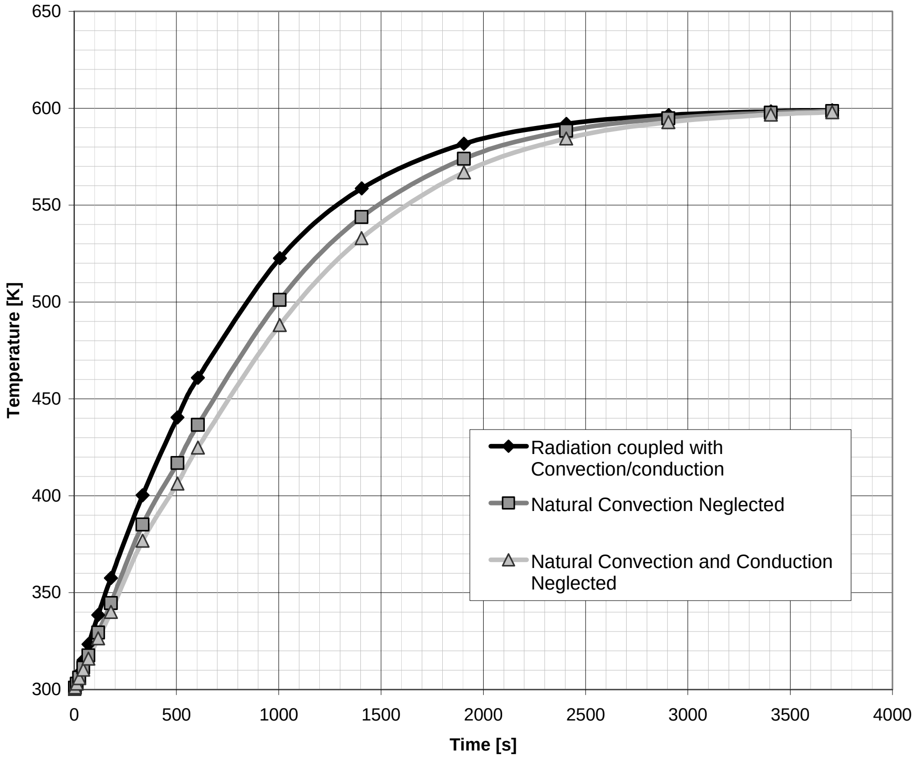

Figure 11: Average surface temperature for obstruction surface temperature, T_r=600 K

Trends on the plot are as expected, indicating the simulations are working properly. When all heat transfer modes are included, the average surface temperature increases fastest. As heat transfer modes are removed, the temperature response slows. All simulations have the greatest temperature increase initially and then converge to a horizontal asymptote. To confirm the trends are as expected, calculations for enclosure radiation are conducted and compared to the results from the conduction neglected simulation results.

Calculations for enclosure radiation are performed using a net radiation formulation. This formulation was originally proposed by Hottel and considers N discrete surfaces that radiation is exchanged between (Howell, 1981). The basic equation is:

$$\sum_{j=1}^{N}\left(\frac{\delta_{kj}}{\varepsilon_i}-F_{k-j}\frac{1-\varepsilon_j}{\varepsilon_j}\right)\frac{Q_j}{A_j}=\sum_{j=1}^{N}\left(\delta_{kj}-F_{k-j}\right)\sigma T_j^4 \tag{4.2}$$

Subscripts represent surfaces, ε is the emissivity of a surface, F is the viewfactors as calculated by equation (1.10), Q is the heat transfer from a surface, A is the area of a surface, σ is Boltzmann's constant, and T is the surface temperature. The symbol δ_{jk} is defined as: δ_{jk} equals 1 when $k = j$ and δ_{jk} equals 0 when $k \neq j$.

Appling equation (4.2) to the two-dimensional model with the adiabatic boundary conditions taken into account to simplify the mathematics, equations (4.3) and (4.4) are solvable numerically to determine the obstruction temperature. Formulation of the matrix equation and the source code for the MATLAB based simulation is provided in Appendix B. Subscript 5 represents the obstruction surface, 4 the bottom boundary, 3 the left boundary, 2 the top boundary, and 1 the right boundary.

$$\begin{bmatrix} \frac{1}{\varepsilon_1 A_1} & F_{12}\sigma & F_{13}\sigma & F_{14}\sigma & -F_{15}\frac{(1-\varepsilon_5)}{\varepsilon_5 A_5} \\ -F_{21}\frac{(1-\varepsilon_1)}{\varepsilon_1 A_1} & -\sigma & F_{23}\sigma & F_{24}\sigma & -F_{25}\frac{(1-\varepsilon_5)}{\varepsilon_5 A_5} \\ -F_{31}\frac{(1-\varepsilon_1)}{\varepsilon_1 A_1} & F_{32}\sigma & -\sigma & F_{34}\sigma & -F_{35}\frac{(1-\varepsilon_5)}{\varepsilon_5 A_5} \\ -F_{41}\frac{(1-\varepsilon_1)}{\varepsilon_1 A_1} & F_{42}\sigma & F_{43}\sigma & -\sigma & -F_{45}\frac{(1-\varepsilon_5)}{\varepsilon_5 A_5} \\ -F_{51}\frac{(1-\varepsilon_1)}{\varepsilon_1 A_1} & F_{52}\sigma & F_{53}\sigma & F_{54}\sigma & \frac{1}{\varepsilon_5 A_5} \end{bmatrix} \begin{Bmatrix} Q_1 \\ T_2^4 \\ T_3^4 \\ T_4^4 \\ Q_5 \end{Bmatrix} = \begin{Bmatrix} \sigma T_1^4 - F_{15}\sigma T_5^4 \\ -F_{12}\sigma T_1^4 - F_{25}\sigma T_5^4 \\ -F_{32}\sigma T_1^4 - F_{35}\sigma T_5^4 \\ -F_{42}\sigma T_1^4 - F_{45}\sigma T_5^4 \\ -F_{52}\sigma T_1^4 + \sigma T_5^4 \end{Bmatrix} \qquad (4.3)$$

$$T_5^{m+1} = -\frac{\Delta t Q_5}{\rho c_p V} + T_5^m \qquad (4.4)$$

Δt is the time step, ρ is density, c_p is specific heat, V is volume, and the superscript m is a time designator. Using a right boundary temperature of 600 K, the superimposed results of the FLUENT and MATLAB simulations are shown in Figure 12. The average surface temperatures extracted from the two simulations correspond within four Kelvin. Differences are probably from using fewer nodes to represent the boundaries in the net radiation method than are used in the FLUENT simulations and viewfactor simplifications.

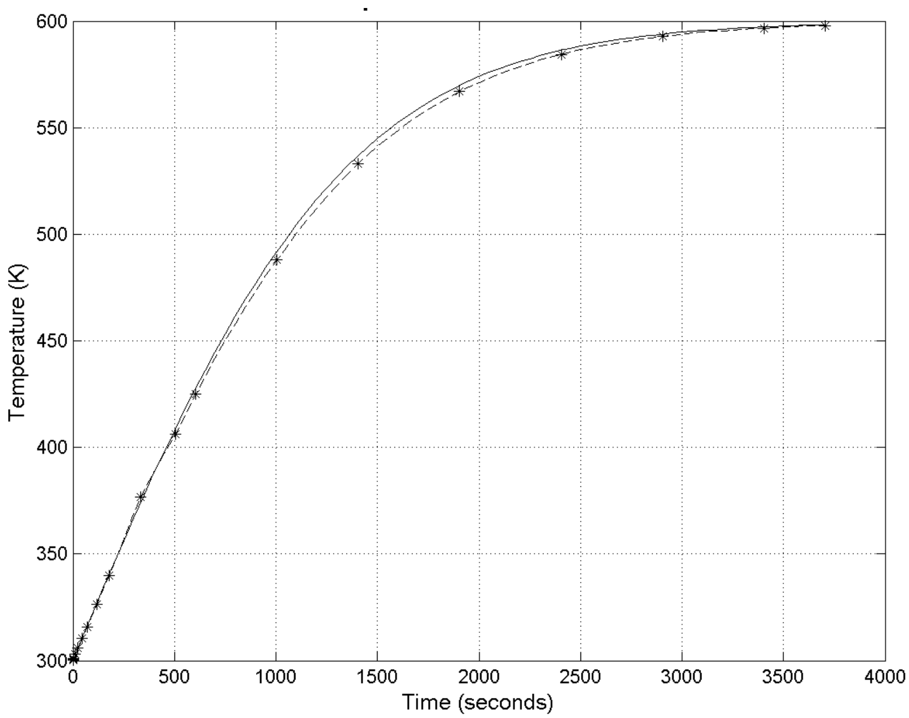

Figure 12: Comparison of FLUENT simulation results and net radiation method simulation results. Solid line is net radiation simulation; dashed black is FLUENT simulation results

4.1.2 Percent Difference in Average Surface Temperature

Temperature results for the average surface temperature on the obstruction are appreciably different. This section takes the average surface temperatures for the three heat transfer simulations in the average surface temperature section and calculates the percent difference using the all heat modes included as the baseline value. Resulting percent differences are used to determine how important each heat transfer mode is to the thermal analysis calculations. If the percent difference is low (low being determined by an analyst performing a calculation), a heat transfer mode may be neglected and meaningful results still obtained. Another way of looking at the problem is if the thermal analysis follows the current setup and only includes one form of heat transfer, such as radiation, and still fails to meet design criteria, then it will fail to meet design criteria with all heat transfer modes included.

Normally percent differences are defined as $\%_{difference} = \frac{\phi_1 - \phi_2}{\phi_1}$ when ϕ_1 is considered the base line. For the average surface temperatures on the obstruction, this equation is problematic. The difference in the temperatures initially increases to a maximum value before decreasing to a small number. At the same time, the denominator starts at a preset number and increases towards the set temperature on the right boundary. To reduce this problem, a new value to normalize the percent difference is used in the denominator. This denominator value is based on the difference between the set right boundary temperature and the initial starting temperature. Applying the change to the denominator produces equation (4.5).

$$\%_{difference} = \frac{\left(T_{all} - T_{neglect}\right)}{\left(T_{Right} - T_{init}\right)} \tag{4.5}$$

Using this reference eliminates the denominator increasing in value, which eliminates a reduction in the percent difference caused by the increasing surface temperature. With a constant base, the point of maximum difference is simpler to determine. Comparison with different boundary conditions is simplified by having a constant base that is determined by specified values in the simulations. Figure 13 shows the percent difference for the temperatures shown in Figure 11.

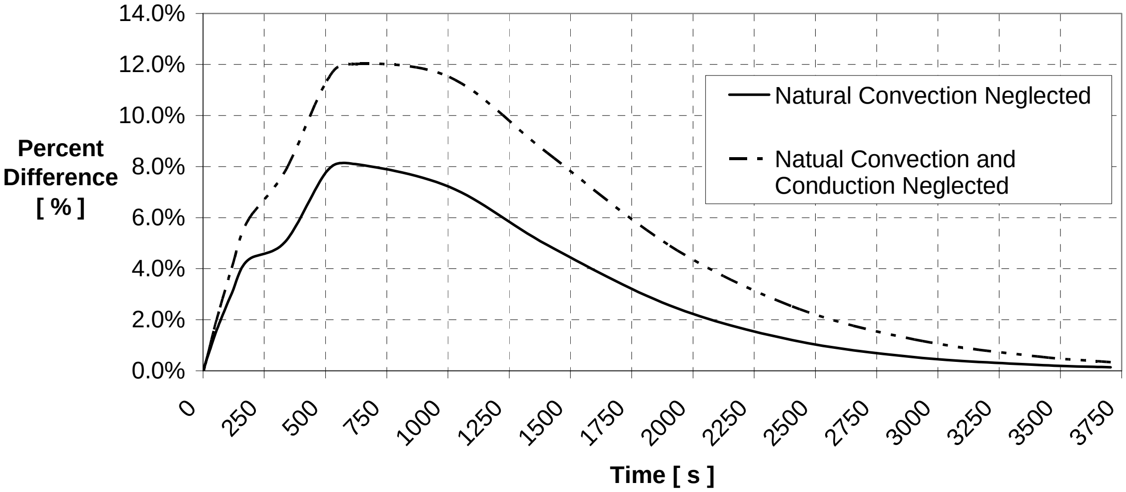

Figure 13: Percent difference in average surface temperature for obstruction surface for all heat transfer modes included and heat transfer modes neglected with T_r=600 K

At time = 0, the surface temperature for all the simulations are equal to the initial temperature. As the simulation is run, the percent difference quickly rises to a maximum difference. For natural convection neglected, this value was a little over 8%. Maximum percent differences for natural convection and conduction neglected increased about 4% over the natural convection neglected value to a total of about 12% difference. After the peak percent difference, the percent difference undergoes an exponential decay towards 0.

The significance of the shape can be related to the temperatures responses. All modes of heat transfer included has the most rapid temperature response, so initially the difference in temperatures increases rapidly. After time passes, the simulation with all modes of heat transfer ceases to increase in temperature as rapidly while the simulations with some mode of heat transfer neglected continue to increase rapidly. As more time passes, the temperature for the simulation with a heat transfer mode neglected starts to increase slower.

Simulations with all heat transfer modes included increase in average surface temperature faster than the simulations with a heat transfer mode neglected. The simulations with a heat transfer mode neglected reach the same temperatures as with all the heat transfer modes included, but at a latter time. This difference in time can be considered a time lag. In comparing the simulations with all heat modes and one with a heat transfer mode neglected, the lag in time when the simulations temperature changes start to decrease is responsible for the exponential shape of the percent difference line.

A notable phenomenon on the graph is the significant decrease and then increase in slope in the line at a time of about 335 seconds. FLUENT recommends starting the transient time solver in the first order scheme. At about 335 seconds, the transient solver was changed to the second order scheme. This is to help with final convergence. First order solver schemes assume values throughout the mesh element are uniform, while the second order solver schemes uses a Taylor expansion to gain more accuracy. Noting Figure 11, the effect on temperature appears to be negligible for the change from the first to second order solver scheme. Effects of the change are highlighted by the percent difference and grow worse at higher right boundary temperatures. It is likely the formulation of the percent difference equation is sensitive to this small change. Also, the simulations with heat transfer modes neglected used the first order solver during the entire simulation because the calculations are simpler and the change was not deemed necessary. This conclusion is supported by the net radiation calculations in section 4.1.1.

4.1.3 Percent Heat Flux

Information with all modes included in the simulations contains the net radiation heat flux and the net total heat flux into a surface. The net radiation heat flux is the difference between the radiation into a surface and the radiation leaving the surface. The net total heat flux is the difference in the heat flux into and the heat flux leaving a surface. The total heat flux is composed of all modes of heat transfer including natural convection, conduction, and radiation. Sign convention for the two heat fluxes is a positive heat flux goes out of a surface, while a negative heat flux is entering a surface.

Like the averaged temperature, the heat flux values for both the radiation and total heat fluxes are stored in cells. Cells in the context used here are formed from the mesh with values such as temperatures and material properties assigned to nodes at the center of the cell. For the purpose of assessing simplified models, local values for heat flux are not as useful as averaged values over a surface, so an average for the net radiation heat flux and net total heat flux are taken in the same manner the average temperatures are taken: heat flux times area summed and divided by the total area.

$$q_{rad\_avg} = \frac{\sum_{i=1}^{n} q_{rad,i} A_i}{\sum_{i=1}^{n} A_i} \tag{4.6}$$

$$q_{tot\_avg} = \frac{\sum_{i=1}^{n} q_{tot,i} A_i}{\sum_{i=1}^{n} A_i} \tag{4.7}$$

Averaging the heat fluxes in this manner reveal problems with the averaging algorithm. Temperature, heat flux, and other values are stored in cells. The averaging algorithm includes all cells present along a surface; including cells shared between adjacent boundaries. Summing the values in the cells present along a surface works for most applications, but when boundaries with different boundary conditions intersect, problems result in the averages.

A good example is the net total heat flux on the top boundary. The boundary is specified as adiabatic, so it should have a value of 0 W/m^2. The algorithm results in a value of 11 W/m^2 at the start time and slowly decreases to 0 W/m^2. The reason is the right boundary has a large net total heat flux, 7385 W/m^2, compared to the top boundary. This value is in a cell that is in contact with the top boundary surface and thus gets averaged into the net total heat flux value for the top boundary. The refined mesh helps in reducing errors associated with the averaging algorithm because the small cells near the surfaces make the area containing the questionable net total heat flux small: the area is 93.3 mm^2. Even the large net total heat fluxes coming from the right boundary are moderated by the small value. The obstruction is not in contact with any other boundaries that could cause this problem. Therefore, the average heat fluxes reported should be a good representation for the actual values.

Ratios of the net radiation heat flux over the net total heat flux result in a percent contribution value for the heat transfer from radiation into the obstruction.

$$\%_{radiation} = \frac{q_{radiation}}{q_{total}} \tag{4.8}$$

Results from the percent contribution calculation from equation (4.8) provide significant insights for the interaction of radiation and all other heat transfer modes. For example, if radiation contributes over 90% of the heat transfer to the obstruction, then the remaining

10% is due to other heat transfer modes (convection, conduction, advection). Values for the percent contribution for the right boundary set to 600 K are graphically shown in Figure 14.

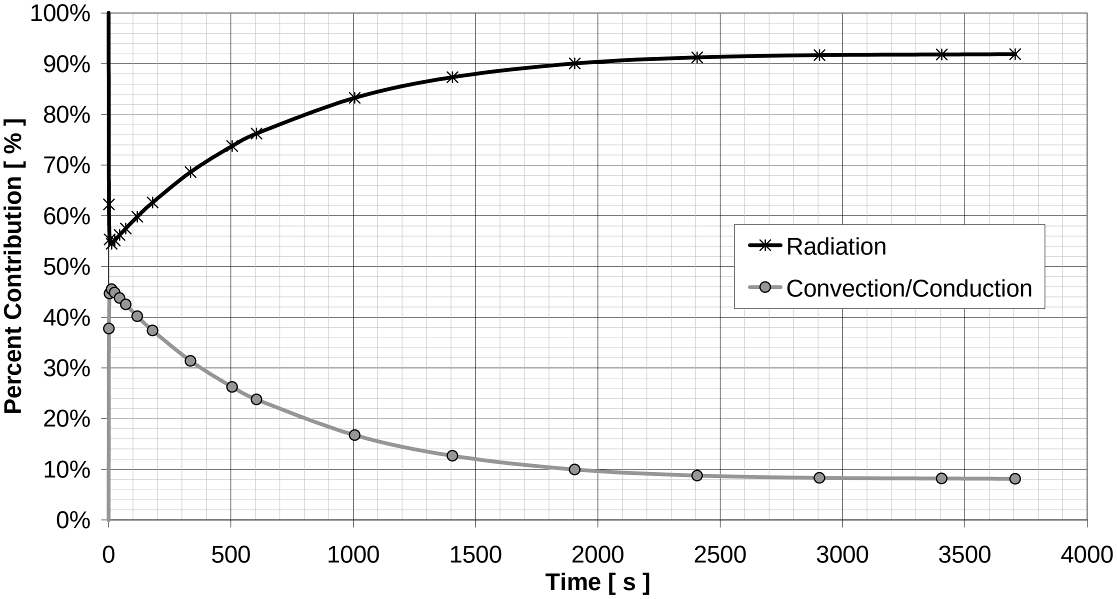

Figure 14: Percent contribution of radiation to the heat transfer into the obstruction for Tr=600K

Initially, 100% of the heat transfer comes from radiation. In less than two seconds, the percent contribution from radiation heat transfer drops close to 60%. After four seconds, the percent contribution from radiation decreases to 54.5%. Radiation continues to contribute less than 70% of the total heat transfer until after 300 seconds. These results indicate that heat transfer modes other than radiation contribute appreciable to the heat transfer to the obstruction for the constant right boundary temperature of 600 K. Natural convection/conduction has the greatest contribution at times lower than 1000 seconds. The average surface temperature plot in Figure 11 shows that times below 1000 seconds are where the average surface temperatures are undergoing the greatest changes and diverging, times after 1000 seconds the average surface temperatures converge to the steady state temperature.

Percent contribution results are not able to segrigate the contribution of natural convection. The flow inside the enclosure could be zero, and all heat transfer would happen through direct conduction through the fluid. Observing the fluid flow aids in observing the presence of natural convection.

4.1.4 Flow Fields

Natural convection occurs in a fluid where the flow is induced by buoyancy forces. Vector plots of fluid movement are useful in determining if natural convection is occurring. Three images are presented in this section to provide an understanding of the fluid motion in the enclosure over time. The first plot (Figure 15) is for a time 0.0996 seconds after the simulations start. The second plot (Figure 16) is for a time 117.51 seconds into the simulation, while the last plot (Figure 17) is for a time of 1005.9 seconds. These three plots include all modes of heat transfer. If buoyancy forces are neglected, there is no fluid motion.

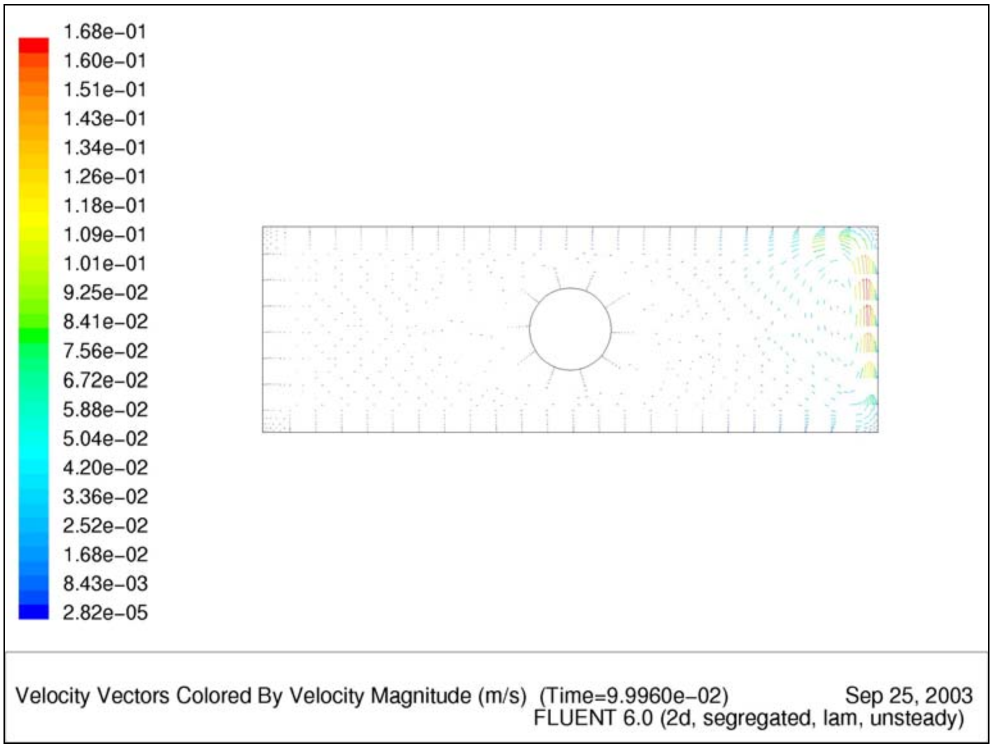

Figure 15: Velocity field for 600 K right boundary temperature at 0.0996 seconds

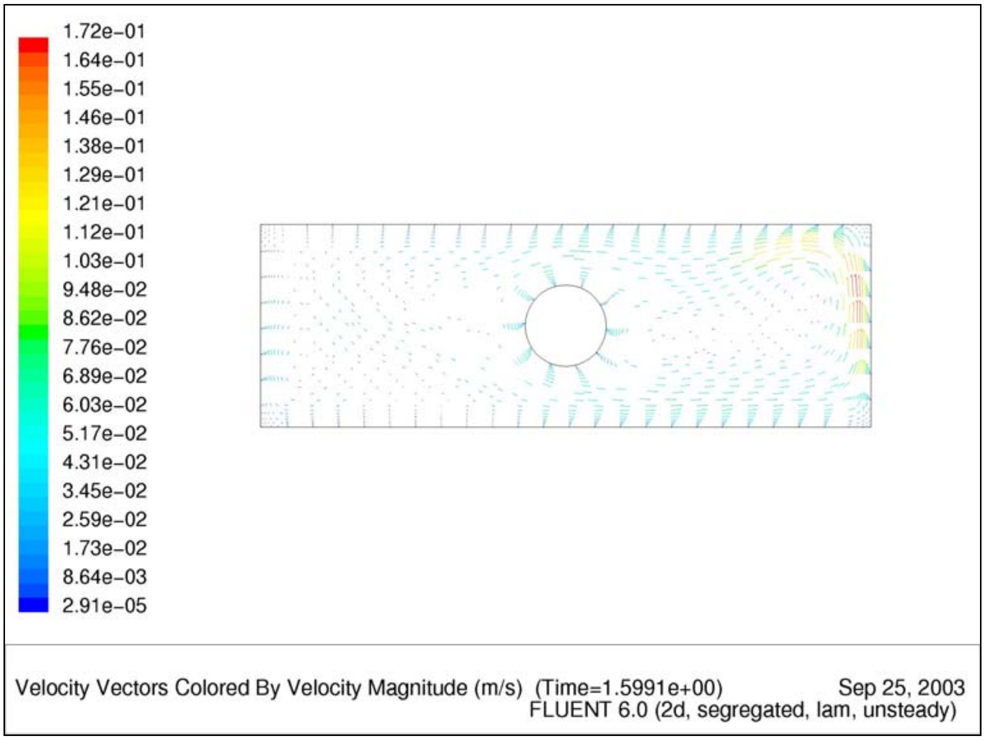

Figure 16: Velocity field for 600 K right boundary temperature at 1.5991 seconds

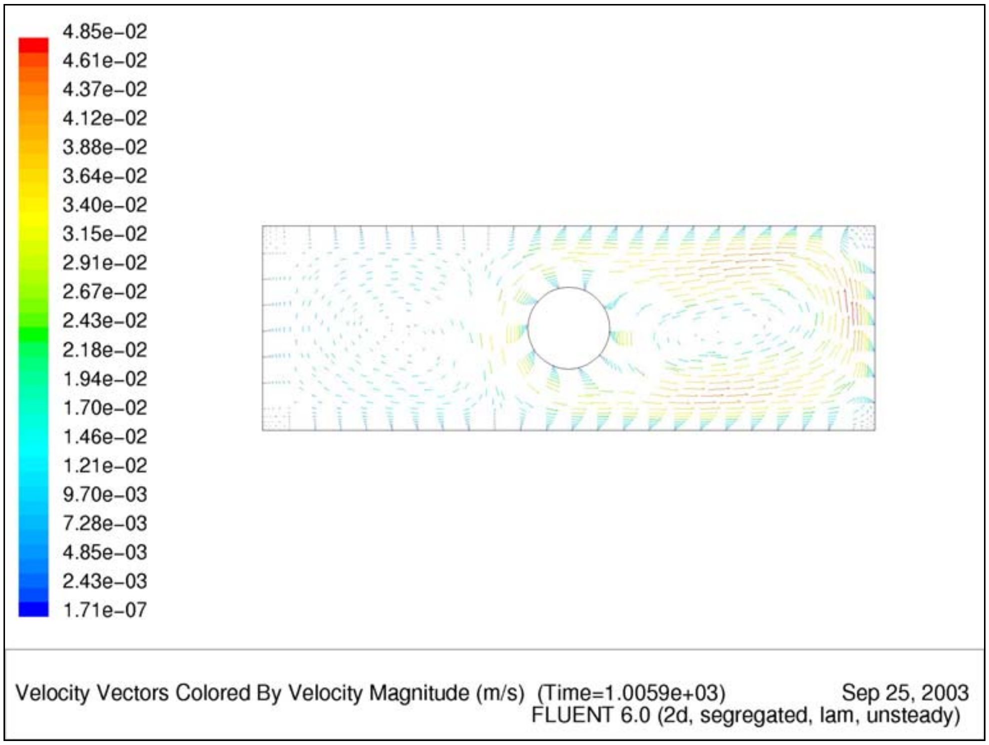

Figure 17: Velocity field for 600 K right boundary temperature at 1005.9 seconds

Figures 15, 16, and 17 show the development of the flow field over time. The maximum velocity is 0.17 m/s at 1.5991 seconds for the 600 K right boundary condition. At the end of the simulation, 3705.8 seconds, the maximum velocity is $1.32*10^{-3}$ m/s; nearly no flow.

Along the boundary, the no slip boundary condition is present with the flow in the interior next to boundaries showing velocity gradients. At the start (Figure 15), fluid flow velocities increase rapidly near the right boundary while the flow in the remainder of the model is relatively small. With passing time (Figures 16 and 17), the flow becomes more structured and forms a main flow cell in the right portion of the model. In the flow cell, fluid rises next to the right boundary, moves across the top boundary until it is near the obstruction. Near the obstruction, the fluid flows down and around the obstruction. Fluid coming off the obstruction splits with the majority of the flow moving back towards the right boundary completing the main flow cell. Fluid leaving the obstruction and moving to the left boundary forms a small secondary flow cell. Fluid velocities in the secondary flow cell are a fraction of the main flow cell and serve to mix the fluid creating a more distributed temperature profile as seen in the temperature plots in the next section. Because the fluid is flowing, there should be heat transfer through natural convection.

4.1.5 Temperature Profiles

Contour plots of temperature provide an overview of the system's temperature field for a specific time. They also allow for any gradients within the obstruction to be viewed, allowing for a determination on the acceptability of the lumped mass assumption. Viewing the temperature plots along with the velocity vector plots shows the relationship of the temperature fields and the flow. Plots for the temperature fields are presented for the same times as the velocity vector plots (Figures 18, 19, and 20). The effect of neglecting different modes of heat transfer on the temperature profiles are shown in Figures 21 and 22.

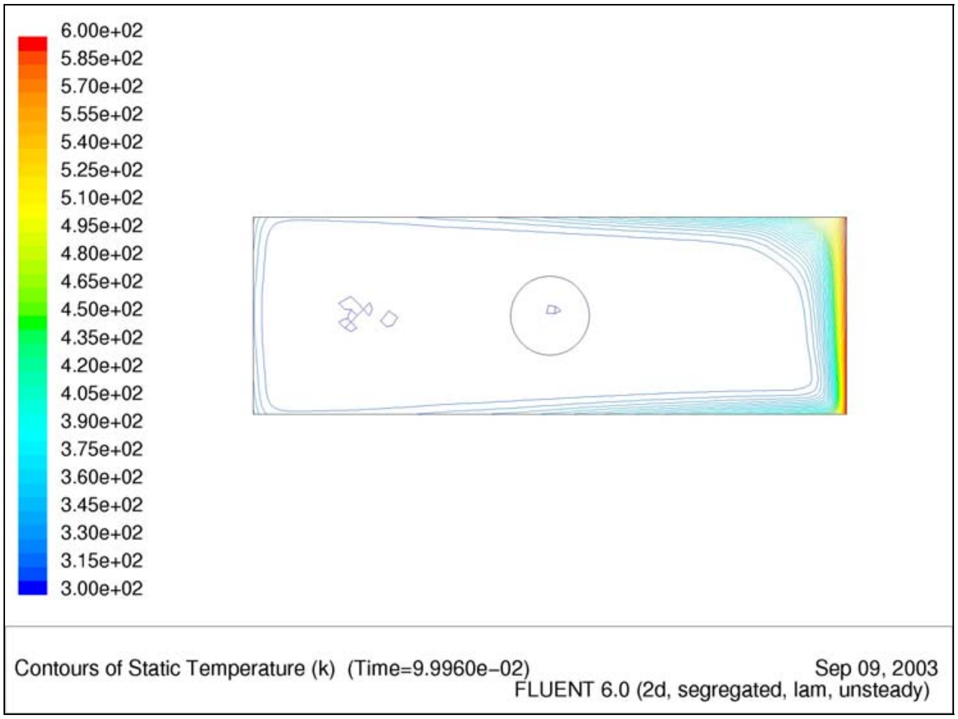

Figure 18: Temperature contours for right boundary at 600 K and time 0.0996 seconds, all heat transfer modes included.

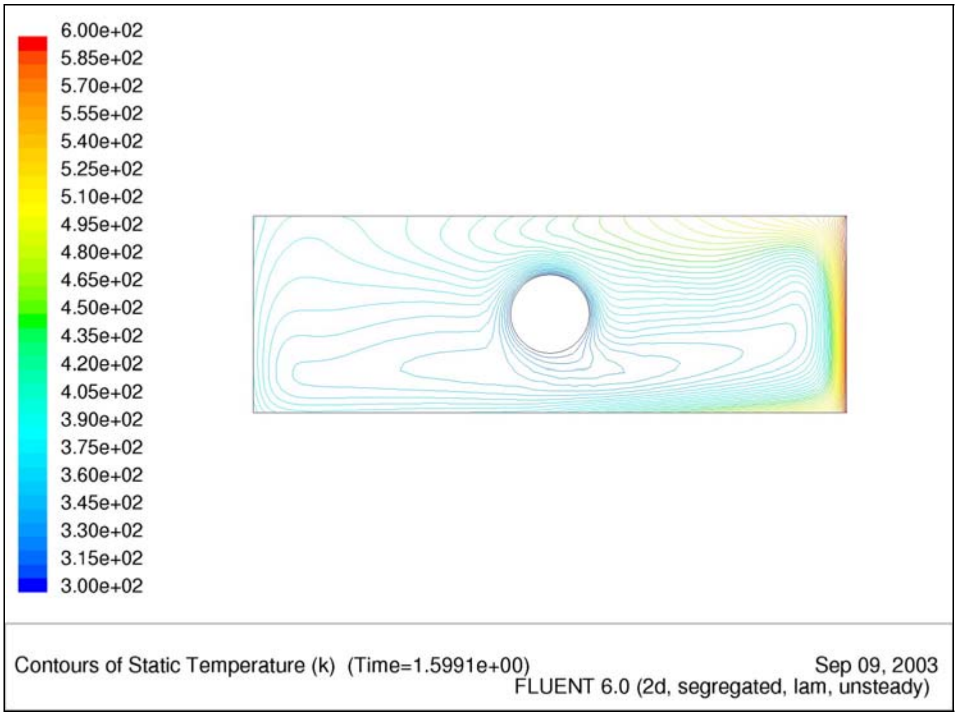

Figure 19: Temperature contours for right boundary at 600 K and time 1.5991 seconds, all heat transfer modes included.

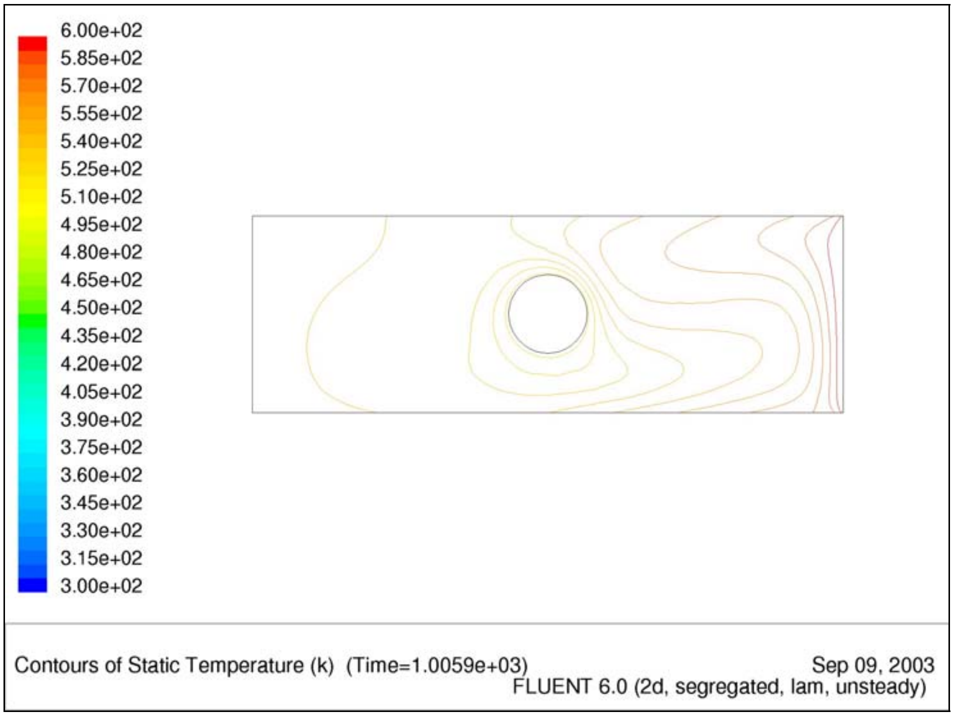

Figure 20: Temperature contours for right boundary at 600 K and time 1005.9 seconds, all heat transfer modes included.

Figure 18 shows the temperature profile immediately after startup (0.0996 seconds). Radiation from the right boundary heats the top and bottom boundaries, which then heat the fluid through conduction. Along the right boundary, the fluid flow disperses warm fluid into the right top corner and along the top boundary more than along the bottom boundary. Along the left boundary, the effects of the obstruction blocking radiation are seen with lower temperatures near the midpoint of the left boundary. Several numerical error regions are also visible but disappear at latter time steps. These regions are found in the center of the left hand portion of the enclosure and the obstruction.

After the flow field has developed (Figures 19 and 20), distinct gradients and stratifications are apparent. In the model's right portion, fluid cooled by the obstruction moves under fluid warmed by the right boundary forming a vertical gradient from the bottom boundary to the top boundary. Along the right boundary, a significant horizontal gradient exists in the fluid. This gradient is where the maximum velocity occurs. After 1000 seconds, the fluid begins to reach the temperature of the right boundary, and the gradients are reduced. However, the effects of the fluid flow are still apparent with how the temperature profiles form extensions into the fluid regions of the model that layer each other. Extensions are defined horizontal temperature gradients in the enclosure.

A simple explanation for the extensions is the right boundary heats the fluid which then moves up because of buoyancy forces. This hot fluid displaces the cooler fluid in the right top corner forcing it towards the left boundary. The obstruction cools the fluid around it causing the fluid density to increase and the fluid to sink. With the cold fluid moving out of the way, the warm fluid moves down to the obstruction and is cooled. In this cycle, the cold fluid moves to the right to replace the fluid being warmed by the right boundary. These advective cells formed from the buoyancy flow result in the horizontal thermal gradients and extensions.

In cases with specific heat transfer modes neglected the temperature profiles (Figures 21 and 22) are significantly different. When buoyancy forces are neglected and conduction and radiation remain, there is no fluid motion; radiation heats the boundaries, which then conduct into the fluid. Looking at the fluid, smooth gradients exist from each of the boundaries extending towards the cool obstruction at the enclosure's centroid. Figure 21 at time 4.1 seconds shows the temperature gradients from the boundaries. Neglecting conduction produces an enclosure radiation problem between the boundaries and the obstruction with no intervening fluid. For these simulations, radiation from the right boundary heats the other boundaries and the obstruction (Figure 22). The fluid has no interaction in the calculations and remains at the initial temperature (limitations in FLUENT result in the fluid being shown), while the obstruction heats up after absorbing energy from the right boundary.

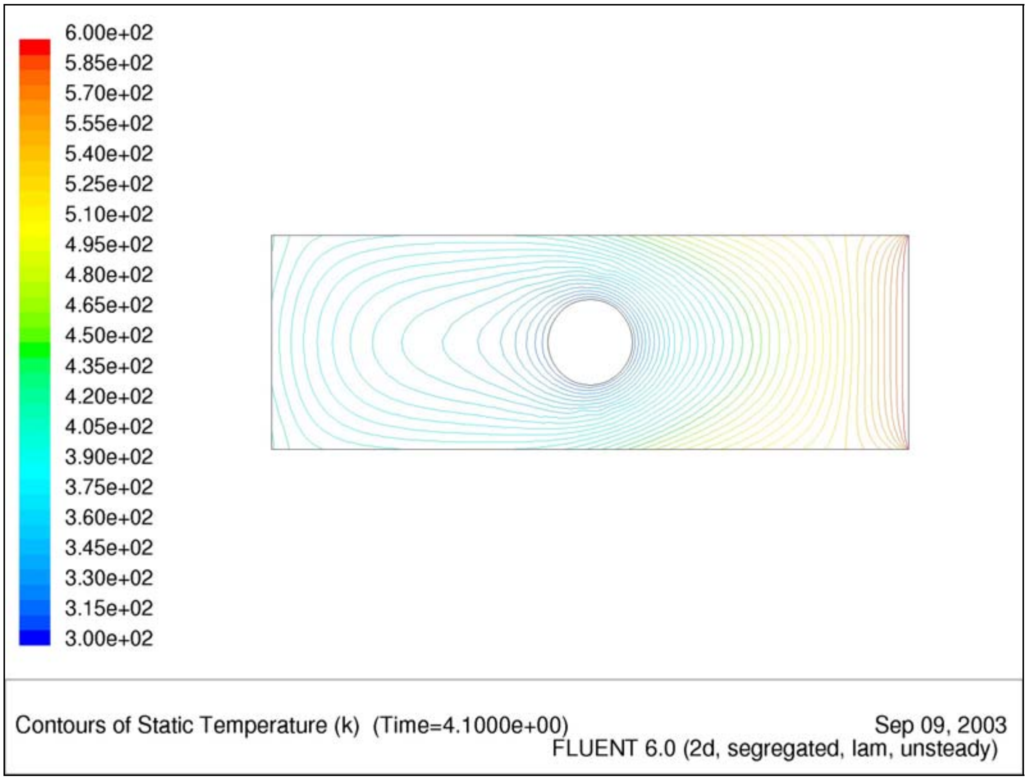

Figure 21: Temperature contours for right boundary at 600 K and time 4.1 seconds, natural convection neglected.

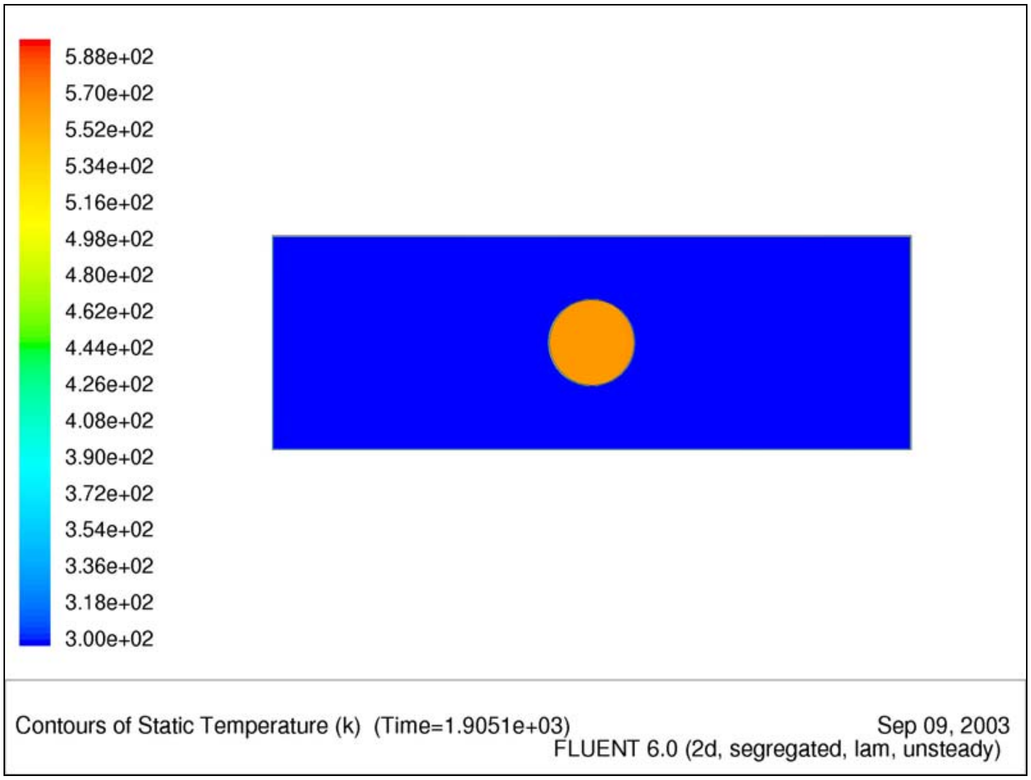

Figure 22: Filled temperature profile for right boundary at 600 K, conduction in fluid suppressed.

4.1.6 Heat Transfer Coefficients

Two methods for presenting heat transfer coefficients are located in this section. The first is a time averaged heat transfer coefficient, while the second is a correlation relating a Rayleigh number to a Nusselt number. Both the Nusselt number and time averaged heat transfer coefficients initial derivations are similar. The derivation of the heat transfer coefficient is first discussed, followed by the time averaging technique, and then by the Nusselt number relations. The section concludes with an example simulation result with discussion.

The heat transfer coefficient is defined by rearranging the convective heat flux rate equation. The resulting equation is:

$$h = \frac{q}{\left(T_S - T_B\right)} \tag{4.9}$$

In this equation, the q can be rewritten as the heat transfer conducted into the fluid at the surface, producing equation (4.10).

$$h = \frac{-k \left.\dfrac{\partial T}{\partial x_i}\right|_{boundary}}{\left(T_S - T_B\right)} = \frac{q_{boundary}}{\left(T_S - T_B\right)} \tag{4.10}$$

The heat transfer from the boundaries, q_{boundary}, is obtained from FLUENT using the method described in section 4.1.3. T_S is the average surface temperature for a boundary, and the T_B is defined as the bulk fluid temperature. Calculating T_B is similar to calculating a boundary average temperature, but area is replaced by volume.

$$T_B = \frac{\sum_{i=1}^{n} T_i V_i}{\sum_{i=1}^{n} V_i} \tag{4.11}$$

Where V_i is the volume of an element, and T_i is the fluid temperature associated with the element.

Implementing the bulk fluid temperature definition posed some problems. Temperature profiles in the model show the fluid temperature is not uniform. This effect is seen on the top and bottom boundaries. On the top and bottom boundaries, the temperature in the fluid toward the right boundary is higher than the fluid temperature towards the left boundary. Fluid temperatures near the left boundary undergo a more uniform temperature change than the fluid near the right boundary, which has large gradients. Overall, the definition for the bulk temperature is helpful in simplifying calculations and presenting data.

Temperature profiles and fluid flow also present problems with estimating heat transfer coefficients. Fluid velocities in the left portion of the model are significantly less than the right. For example, in some instances, the velocities could even be considered negligible. Under these conditions, heat transfer from the left boundary is controlled more by conduction than convection. As the flow develops, the convection increases. To some extent, this behavior is seen by all the boundaries and surfaces. An initial condition for the simulations is that fluid starts at rest. When the simulation starts, heat is conducted into the fluid creating temperature and density gradients which cause buoyant flow. Not until the flow starts can convection be considered and the convective heat transfer coefficients have any meaning.

To reduce uncertainty associated with fluid flow development, the first three data values from the start of the simulation are not included in the time averaged heat transfer coefficient and Nusselt correlations. Heat fluxes on the top, bottom, and left boundaries are negligible compared to those of the obstruction and the right boundary. Because the obstruction and right boundary dominate the heat transfer in the simulation, only heat transfer coefficients and relations for the obstruction and right boundary were assessed.

Calculations for the average heat transfer coefficient start with extracting average heat fluxes, boundary temperatures, and bulk fluid temperature for select time data: select time data in effect being points numerical data was saved. Equation (4.10) is used to calculate a heat transfer coefficient for each time data. Table 3 summarizes the values for the two-dimensional simulation with an aspect ratio of 1/3, shaft ratio of 2/5, and right boundary temperature of 600 K.

Table 3: Calculations of Heat Transfer Coefficients

Time [s]	T_B [K]	Obstruction			Right Boundary		
		T [K]	q [W/m^2]	h [W/m^{2}K]	T [K]	q [W/m^2]	h [W/m^{2}K]
0.09996	321.21	300.04	0.47	0.022	599.96	2775.46	9.957
1.5991	394.41	300.44	-912.67	9.711	599.97	1767.98	8.601
4.049	434.03	301.24	-1474.50	11.104	599.98	1251.17	7.540
12.479	445.09	304.11	-1592.64	11.297	599.98	1114.23	7.194
25.079	447.09	308.40	-1552.60	11.195	599.98	1091.65	7.140
45.229	450.20	315.17	-1490.03	11.034	599.98	1057.01	7.057
70.109	453.96	323.36	-1416.21	10.843	599.98	1015.83	6.957
117.51	460.92	338.49	-1285.55	10.501	599.98	941.85	6.773
180.11	469.71	357.54	-1131.29	10.086	599.98	852.10	6.541
334.91	489.86	400.25	-824.53	9.202	599.98	662.23	6.014
504.91	509.70	440.41	-581.01	8.385	599.98	496.19	5.496
604.91	520.28	460.91	-472.05	7.951	599.99	415.69	5.215
1005.9	554.10	522.64	-202.09	6.424	599.99	195.23	4.254
1405.8	575.10	558.64	-85.98	5.222	600.00	88.40	3.551
1905.8	588.89	581.66	-30.85	4.264	600.00	33.27	2.996
2405.8	595.12	591.97	-12.05	3.822	600.00	13.29	2.725
2905.8	597.85	596.46	-5.07	3.667	600.00	5.68	2.639
3405.8	599.03	598.41	-2.25	3.625	600.00	2.53	2.604
3705.8	599.37	598.97	-1.44	3.595	600.00	1.64	2.617
Time Averaged				8.053			5.519

Time averaging for the heat transfer coefficient is done by summing the individual heat transfer coefficient by a backwards time difference. The total sum is divided by the total time of the summation.

$$h_{tavg} = \frac{\sum_{i=1}^{N} h_i \left(t^i - t^{i-1}\right)}{\left(t_{end} - t_{start}\right)} \tag{4.12}$$

This equation is for N number of time divisions. Parameter h_i is the heat transfer coefficient at specified moments in time t^i. A numerical approximation is made by assuming the heat transfer coefficient is represented as h_i since the last time step t^{i-1}. The value for t_{end} is the value for the last t^i value in the summation, while t_{start} is the time associated with the first t^{i-1} value.

Equation (4.12) is a numerical approximation for the heat transfer coefficient over time using the rectangular approximations. This method has an error associated with it depending on the number of divisions used in the approximation. Smaller time steps are used for the heat transfer coefficients in the early time stages when the value changes more rapidly and larger time steps in regions where the heat transfer coefficients are more constant. The effect of varying the time to match changing heat transfer coefficients is to reduce the error introduced by under or overestimates associated with rectangular area summations to approximate the integral.

For enclosed systems such as windows (simple schematic of a two pane window is shown in Figure 23) at steady-state, the value for the heat transfer coefficient near the "hot" boundary is lower than the value at the "cold" boundary. Using a similar approach, the heat transfer coefficients for the current simulations are as expected. Near the right boundary, which is considered the "hot" boundary, the average heat transfer coefficient is 5.5 W/m^{2}K. This value is lower than the averaged heat transfer coefficient of the obstruction value of 8.1 W/m^{2}K. Unlike the window at steady-state, the system is undergoing a transient change and energy is dissipated into the fluid to warm it as well as the boundaries. Therefore, in a transient case, not all the heat flux leaving the "hot" boundary enters the "cold" surface of the obstruction.

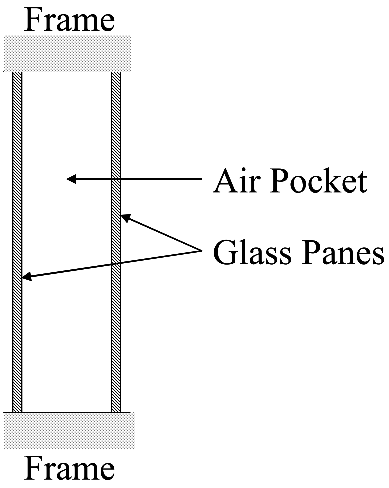

Figure 23: Two pane window schematic: side cutout view

Average heat transfer coefficients provide a simplified means for estimating the amount of energy transfer due to natural convection. For natural convection, the heat transfer coefficient is often expressed using the Nusselt number and correlated with the Rayleigh and Prandlt numbers. Definitions for Rayleigh and Nusselt numbers are given below:

$$Ra \equiv \frac{g\rho^2 c_p L^3 \beta (T_i - T_B)}{k\mu} \tag{4.13}$$

$$Nu \equiv \frac{hL}{k} \tag{4.14}$$

Where k is the thermal conductivity, μ is the fluid viscosity, β is the thermal expansion coefficient, L is a length scale, c_p is the specific heat, ρ is the density, and g is gravity.

The fluid properties in the Rayleigh equation are evaluated at the initial temperature of the simulation. This creates a parameter affected only by temperatures in the simulations. Nusselt values are correlated from the heat transfer coefficients at specified times and linked with the corresponding Rayleigh number. Least square regression is used to develop relationships between sets of Rayleigh numbers and Nusselt numbers. Several equation forms are used, the standard power format and a quadratic formulation. In Figure 24, data points represent the Rayleigh-Nusselt pairs. The lines are the least square regression fits. Parameters for the least square regression fits are summarized in Table 4.

Traditionally, literature presents the Nusselt-Rayleigh correlations in a power format (Holman 2002, Incropera and DeWitt 1996, and Mills 1999). Nusselt-Rayleigh plots presented by Holman (2002) show the relation can be broken up into three regions on a log-log plot. The first and third regions are logarithmically linear, while the second region is a smooth curve with increasing positive slope that connects the first and third regions. The change in slope on the log-log plot dictates the regions.

Correlations are generally expressed in the power format for the first and third regions with bounds placed on the Rayleigh numbers that are applicable for the correlation. An example is a vertical enclosure, similar to Figure 23, with a height H and distance between surfaces L. Incropera and DeWitt (1999) give a relation as:

$$Nu_L = 0.22\left(\frac{\Pr}{0.2+\Pr}Ra_L\right)^{0.28}\left(\frac{H}{L}\right)^{-1/4}$$

$$\begin{bmatrix} 2 < \dfrac{H}{L} < 10 \\ \Pr < 10^5 \\ 10^3 < Ra_L < 10^{10} \end{bmatrix} \tag{4.15}$$

Where Pr is the Prandlt number, H is the height, L is the length. To be able to use the Nusselt to Rayleigh correlation, all the requirements in the bracketed list must be met.

Nusselt-Rayleigh values in the current research appear to be in the second region where the data curves. Curve fit values appear to be good (R^2 values above 0.89) whether the equation is a power or quadratic. However, the quadratic fits followed the trends of the data more closely (Figure 24). Rayleigh numbers for this research are between 0.005 and 300 (Figures 25 and 26).

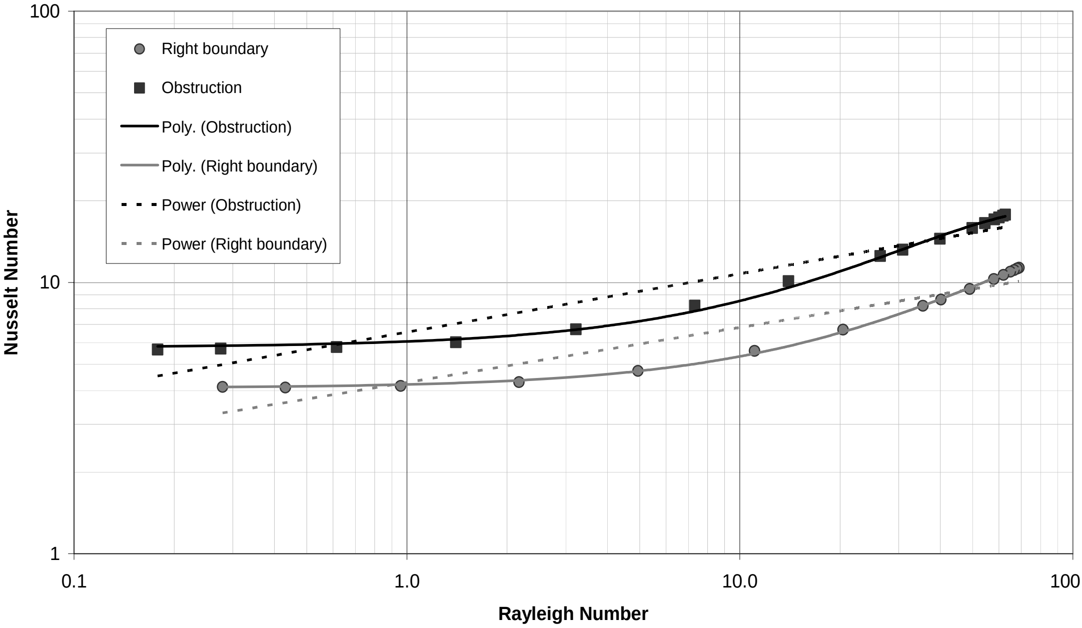

Figure 24: Nusselt to Rayleigh data: right boundary temperature of 600 K

Table 4: Nusselt to Rayleigh Correlations: Right Boundary Temperature of 600 K

		Correlation	R^2 fit
Obstruction	Power	$Nu = 6.556*Ra^{0.2156}$	0.922
	Polynomial	$Nu = -0.0017*Ra^2 + 0.296*Ra + 5.765$	0.997
Right Boundary	Power	$Nu = 4.279*Ra^{0.2029}$	0.895
	Polynomial	$Nu = -0.0004*Ra^2 + 0.130*Ra + 4.077$	1.000

4.2 Complete Simulations Results

Earlier in this chapter, data were presented for an enclosure with aspect ration 1/3, shaft ratio of 2/5, and right boundary temperature of 600 K. This part of the chapter is devoted to presenting the data for all simulations in the form of summary tables and graphs.

4.2.1 Average Surface Temperature and Percent Difference on the Obstruction

Trends for the increase in average surface temperature are similar for all simulations. The main differences are that the simulations have temperature responses and average temperature convergence values dependent on right boundary temperatures. Changing the aspect ratio affects the response. Using 1000 seconds as a reference time between simulations, each change in aspect ratio (i.e. 1/4 to 1/3 to 1/2) retards the temperature response by around 10 K. Observing the aspect ratio trend, the results for the 1/3 aspect ratio is midway between the responses of the 1/4 and 1/2 aspect ratios.

With the exception of when the right boundary temperature was 1275 K, plots of the surface temperature and percent temperature difference had the same trends as those described in section 4.1.1. The exception with the right boundary temperature of 1275 K occurred because the numerical solver in FLUENT allowed the temperature to increase too rapidly, overshoot, and never converge to a proper solution. Taking smaller time steps did not help the problem out enough to formulate a solution to include in the results. Calculations using the net radiation method are able to produce a solution that matches what is expected given the other simulation trends. The average obstruction surface temperature results are presented in Figures 31 through 46 in Appendix C.

Percent temperature difference values are greatest for the low temperatures on the right boundary and decrease as the temperatures increase. At T_R equals 310 K, the maximum error for neglecting natural convection was 9.3% and 19.0% for conduction neglected also: temperature differences of 0.93 K and 1.9 K respectively. For T_R equal to 1275 K, the error falls to a maximum value of 1.03% ($\Delta T = 10.04$ K) for natural convection neglected. No value is available for conduction neglected on T_R equals 1275 K, but T_R equal to 1100 K has a maximum error of 2.76% ($\Delta T = 22.09$ K) for conduction neglected. Table 5 summarizes the maximum error for all the simulations.

Shaft ratios are considered special. Changing the shaft ratio affects the system in several ways. It changes the thermal mass in the center, and it changes the amount of blockage for the viewfactors. These effects are apparent in the graphs for the temperature response. A small thermal mass allows the obstruction to increase in temperature quickly when a heat flux enters it, but less direct radiation is likely to be incident on it. Also, larger obstructions receive more direct radiation than those of smaller diameter. Radiation heat flux is reduced due to smaller viewfactors and is why the temperature response for conduction suppressed is so slow for the 1/5 shaft ratio simulation leading to the large percent temperature difference shown in Table 5.

For the percent difference, several of the graphs dip or have negative values. This occurs at a time near 335 seconds, the point where the solver type is changed from first order to second order. The dips are really only a problem for the higher simulation T_R values of 800 K and higher. What occurs at these points is the heat modes neglected temperature values bypass the all modes included temperature baseline. This is a result of the error in numerical simulation from tolerance issues and approximation used in reaching a solution. Temperature values are within several Kelvin of each other and the problem is localized to this moment in time, so the error is not considered significant.

Table 5: Maximum Percent Temperature Differences: All Heat Transfer Modes Included Set as Base Case and Comparison Against Heat Modes Neglected

T_R [K]	AR	SR	Geometry	Maximum Temperature Difference [K]		Maximum Percent Temperature Difference (Error) [%]	
				Buoyancy off	Conduction suppressed	Buoyancy off	Conduction suppressed
310	1/3	2/5	2d	0.93	1.90	9.27	19.04
500	1/3	2/5	2d	22.85	33.90	11.42	16.95
600	1/3	2/5	2d	24.36	36.05	8.12	12.02
800	1/3	2/5	2d	18.96	30.53	3.74	6.11
950	1/3	2/5	2d	16.37	25.16	2.52	3.87
1100	1/3	2/5	2d	13.32	22.09	1.66	2.76
1275	1/3	2/5	2d	10.04	-----	1.03	-----
600	1/4	2/5	2d	21.98	36.45	7.33	12.15
600	1/2	2/5	2d	25.97	35.94	8.66	11.97
600	1/3	1/5	2d	25.10	246.82	8.37	82.27
600	1/3	3/5	2d	24.29	35.52	8.10	11.84

4.2.2 Heat Flux Contributions

Graphs for the percent contribution are found in Appendix D. The graphs for changing aspect ratio show the percent radiation contribution increases by 2% for each change in aspect ratio from 1/4 to 1/3 to 1/2. At an aspect ratio of 1/4, the minimum percent contribution from radiation is 52.4%, while the aspect ratio of 1/2 has a minimum percent contribution from radiation of 56.8%.

Changing only one parameter at a time reveals large effects in radiation percent contribution. Shaft ratios play an important part in the heat transfer. Modifying the shaft ratio, radiation minimum percent contribution is greater in the larger shaft ratio (3/5) than the smaller shaft ratio (1/5), 56.1% and 50.6% respectively. As the right boundary temperature is increased from 310 K to 1275 K on an aspect ratio of 1/3 and shaft ratio of 2/5, the minimum values for radiation percent contribution change from 46.9% to 88.7%. The full list of minimum percent radiation contributions are found in Table 6 on page 70. Percentages in Table 6 are larger than Table 5 because the percent temperature difference has a larger base denominator.

4.2.3 Fluid Flow and Temperature Profiles

Fluid velocity vectors and temperature profiles for the complete list of simulations are similar to those presented in section 4.1.4 and 4.1.5. Some apparent nuances exist between the simulations, such as geometry factors like aspect and shaft ratios. Other nuances are more subtle like the 15 to 30 K gradients visible in the right portion of the obstruction for the higher right boundary temperatures (1100 K and 1275 K). Even with the gradient, average surface temperatures still provides a reasonable representation of the obstruction temperature within a 5 K error. Vector plots are like the temperature plots in that the trends look similar. The major difference is the maximum velocities achieved. These maximum velocities are shown in Table 7.

Table 6: Minimum Percent Radiation Contribution: All Heat Transfer Modes Source Data

T_R [K]	AR	SR	Geometry	Minimum Percent Radiation Contribution (%)
310	1/3	2/5	2d	46.94
500	1/3	2/5	2d	47.43
600	1/3	2/5	2d	54.48
800	1/3	2/5	2d	68.70
950	1/3	2/5	2d	77.17
1100	1/3	2/5	2d	83.54
1275	1/3	2/5	2d	88.71
600	1/4	2/5	2d	56.81
600	1/2	2/5	2d	52.41
600	1/3	1/5	2d	50.59
600	1/3	3/5	2d	56.05
310	1/3	2/5	3d	39.48
500	1/3	2/5	3d	45.47
600	1/3	2/5	3d	52.04
950	1/3	2/5	3d	74.08
1275	1/3	2/5	3d	86.77

Table 7: Maximum Velocities

T_R [K]	AR	SR	Geometry	Maximum velocities [m/s]
310	1/3	2/5	2d	0.0281
500	1/3	2/5	2d	0.140
600	1/3	2/5	2d	0.172
800	1/3	2/5	2d	0.234
950	1/3	2/5	2d	0.271
1100	1/3	2/5	2d	0.301
1275	1/3	2/5	2d	0.334
600	1/4	2/5	2d	0.168
600	1/2	2/5	2d	0.199
600	1/3	1/5	2d	0.168
600	1/3	3/5	2d	0.174
310	1/3	2/5	3d	0.0272
500	1/3	2/5	3d	0.141
600	1/3	2/5	3d	0.166
950	1/3	2/5	3d	0.319
1275	1/3	2/5	3d	0.355

4.2.4 Heat Transfer Coefficients

Values and correlations for the convective heat transfer coefficients are presented in three tables: average heat transfer coefficients (Table 8), Nusselt to Rayleigh correlations for the obstruction (Table 9), and Nusselt to Rayleigh correlations for the right boundary (Table 10). Two plots of all Rayleigh-Nusselt data points for the obstruction (Figure 25) and the right boundary (Figure 26) are provided. Section 4.2.4 also talks about problems with determining overall correlations.

Determination of heat transfer coefficient correlations are hindered by problems in the bulk temperature definition. Points where heat transfer interactions should be are not properly represented by using a single bulk fluid temperature. For example, the right boundary would only interact with fluid in the right fluid region of the enclosure, which has a different average fluid temperature than the entire enclosure. Data points on Figures 25 and 26 are expected to line up, but problems with the bulk fluid temperature cause the data points to not line up. This in turn causes scattering that reduces the R^2 fit of the general correlation.

Adding to the problem are the data points from simulations with right boundary temperatures like 1100 K and 1275 K. These simulations converge quickly to the right boundary temperature resulting in a large number of data points at the end with skewed values caused by tolerance issues in FLUENT. For this reason, Rayleigh values below 0.1 are ignored. Attempting a general correlation produces equations (4.16) and (4.17).

$$Nu_{obstruction} = 7.712 * Ra_{obstruction}^{0.146} \tag{4.16}$$

$$Nu_{Right} = 5.303 * Ra_{Right}^{0.106} \tag{4.17}$$

Table 8: Time Averaged Heat Transfer Coefficients

T_R [K]	AR	SR	Geometry	Time averaged heat transfer coefficients [W/m^{2}K]	
				Obstruction	Right boundary
310	1/3	2/5	2d	7.719	4.471
500	1/3	2/5	2d	9.288	5.946
600	1/3	2/5	2d	8.053	5.519
800	1/3	2/5	2d	7.283	5.608
950	1/3	2/5	2d	7.078	5.586
1100	1/3	2/5	2d	8.025	6.191
1275	1/3	2/5	2d	7.065	6.037
600	1/4	2/5	2d	8.729	6.483
600	1/2	2/5	2d	7.648	4.900
600	1/3	1/5	2d	8.817	4.548
600	1/3	3/5	2d	10.062	6.447
310	1/3	2/5	3d	8.354	4.708
500	1/3	2/5	3d	9.669	5.834
600	1/3	2/5	3d	8.651	5.314
950	1/3	2/5	3d	6.201	4.941
1275	1/3	2/5	3d	5.518	4.719

Table 9: Obstruction Nusselt to Rayleigh Correlations: Nu = A*Ra^2+B*Ra+C. All R^2 Values Are Greater Than 0.95

T_R [K]	AR	SR	Geometry	Correlation Constants		
				A	B	C
310	1/3	2/5	2d	-0.8125	4.3571	4.7638
500	1/3	2/5	2d	-0.005	0.4783	5.9322
600	1/3	2/5	2d	-0.0017	0.2958	5.7648
800	1/3	2/5	2d	-0.0004	0.1494	5.5397
950	1/3	2/5	2d	$-6*10^{-5}$	0.0797	6.1351
1100	1/3	2/5	2d	$-4*10^{-5}$	0.0635	5.7202
1275	1/3	2/5	2d	$-2*10^{-5}$	0.0457	5.638
600	1/4	2/5	2d	-0.0016	0.2815	6.7485
600	1/2	2/5	2d	-0.0017	0.3018	5.1106
600	1/3	1/5	2d	-0.0011	0.2719	7.9289
600	1/3	3/5	2d	-0.0033	0.3939	5.4801
310	1/3	2/5	3d	-0.7961	4.0847	5.1538
500	1/3	2/5	3d	-0.0049	0.4525	6.4003
600	1/3	2/5	3d	-0.0018	0.2872	6.261
950	1/3	2/5	3d	-0.0003	0.1202	5.4975
1275	1/3	2/5	3d	-0.0004	0.0679	5.2872

Table 10: Right Boundary Nusselt to Rayleigh Correlations: Nu = A*Ra^2+B*Ra+C. All R^2 Values Are Greater Than 0.95

T_R [K]	AR	SR	Geometry	Correlation Constants		
				A	B	C
310	1/3	2/5	2d	-0.1486	1.6496	2.3997
500	1/3	2/5	2d	-0.0012	0.2235	3.5488
600	1/3	2/5	2d	-0.0004	0.1298	4.0771
800	1/3	2/5	2d	$1*10^{-5}$	0.0512	4.7711
950	1/3	2/5	2d	$5*10^{-5}$	0.0288	5.0639
1100	1/3	2/5	2d	$7*10^{-5}$	0.0123	5.4635
1275	1/3	2/5	2d	$6*10^{-5}$	0.0047	5.6841
600	1/4	2/5	2d	-0.0006	0.1565	4.9922
600	1/2	2/5	2d	-0.0002	0.1086	3.5212
600	1/3	1/5	2d	-0.0007	0.1563	4.1149
600	1/3	3/5	2d	$6*10^{-5}$	0.0808	3.8884
310	1/3	2/5	3d	-0.0887	1.2644	2.4796
500	1/3	2/5	3d	-0.0006	0.1743	3.7082
600	1/3	2/5	3d	$-4*10^{-6}$	0.0922	4.0702
950	1/3	2/5	3d	0.0002	0.0063	4.7501
1275	1/3	2/5	3d	0.0001	-0.0058	4.7596

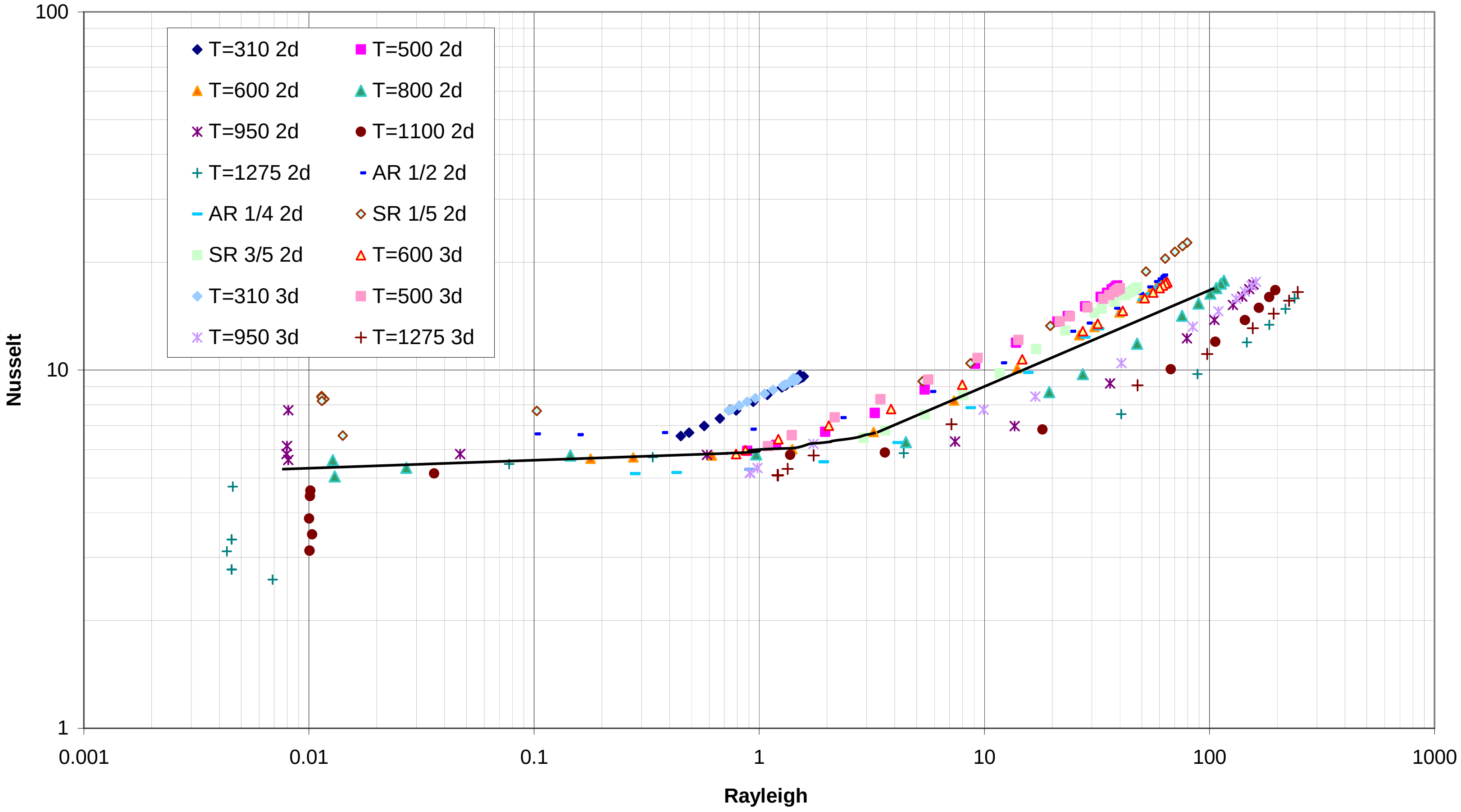

Figure 25: Obstruction Nusselt-Rayleigh data

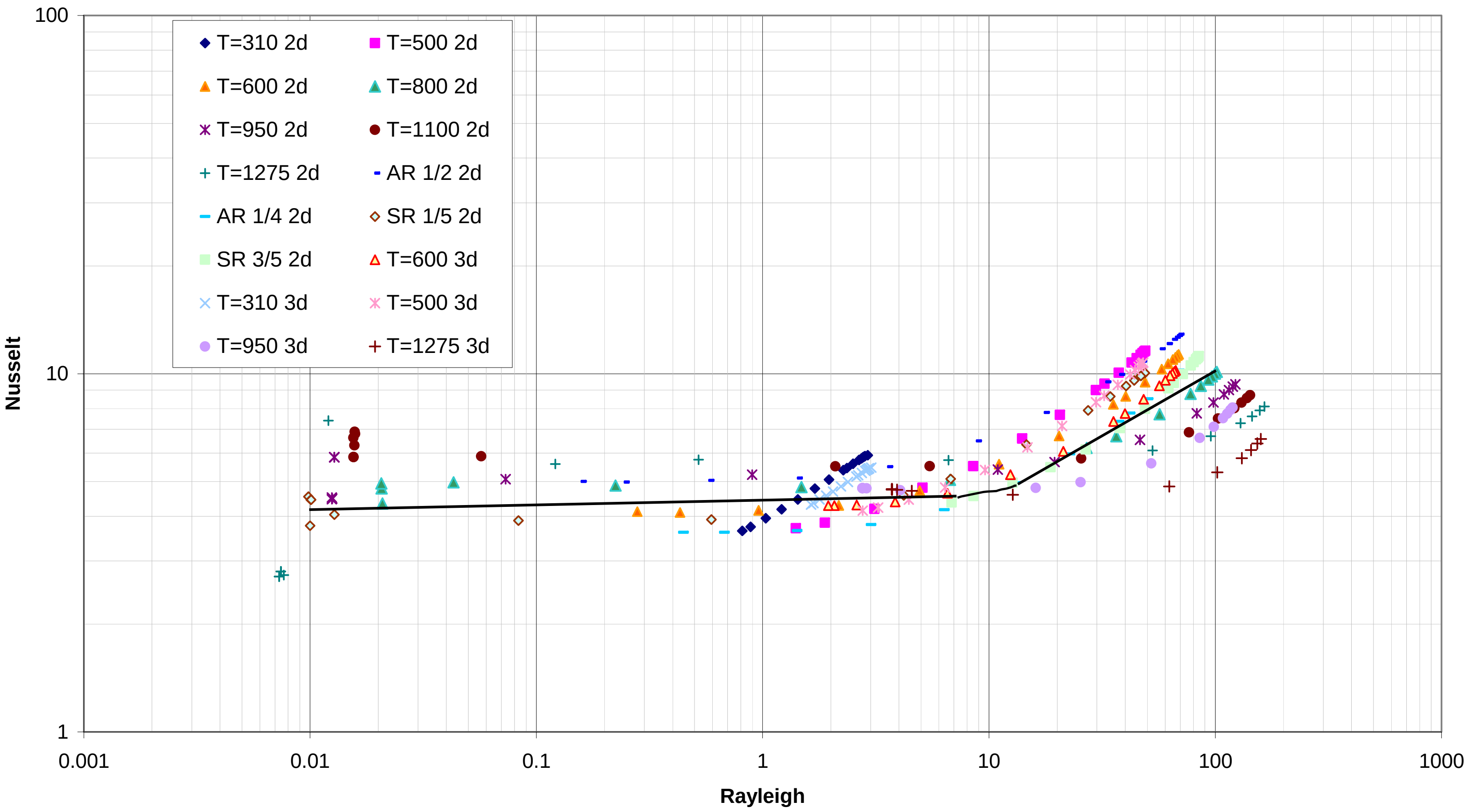

Figure 26: Right boundary Nusselt-Rayleigh data

4.2.5 Stepping Right Boundary Temperature

Sometimes, small changes have a large impact on simulations. Temperature stepping the right boundary is designed to simulate a transient boundary condition temperature response. Results are presented for the obstruction average temperature, percent radiation contribution, time averaged heat transfer coefficients, and the Nusselt-Rayleigh correlations. Results from the temperature stepping are predictable from the constant boundary temperatures with several exceptions, the obstruction temperature response and heat transfer relations.

The response of the average obstruction surface temperature is different than the constant temperature right boundary condition simulations (Figure 27). This response begins with a slow initial temperature rise, followed by a rapid temperature rise, and ends with stabilization to a temperature equal to the final right boundary temperature. The dots represent the time instance when the right boundary temperature changes and the quantitative value of the temperature change.

Radiation percent contribution is shown in Figure 28. Data save points are different for the temperature stepping simulation than the constant temperature simulations, preventing a comparison for starting times like 0.1 seconds, but comparisons may still be made. While the right boundary temperature is 310 K, the percent radiation contribution is about 41%. As the right boundary temperatures increase, the percent radiation contribution increases to nearly 100% for the right boundary temperature of 1275 K. Comparing with constant right boundary temperatures, the minimum radiation contribution is 5% lower than expected, but the high is in line with constant right boundary temperature of 1275 K simulations.

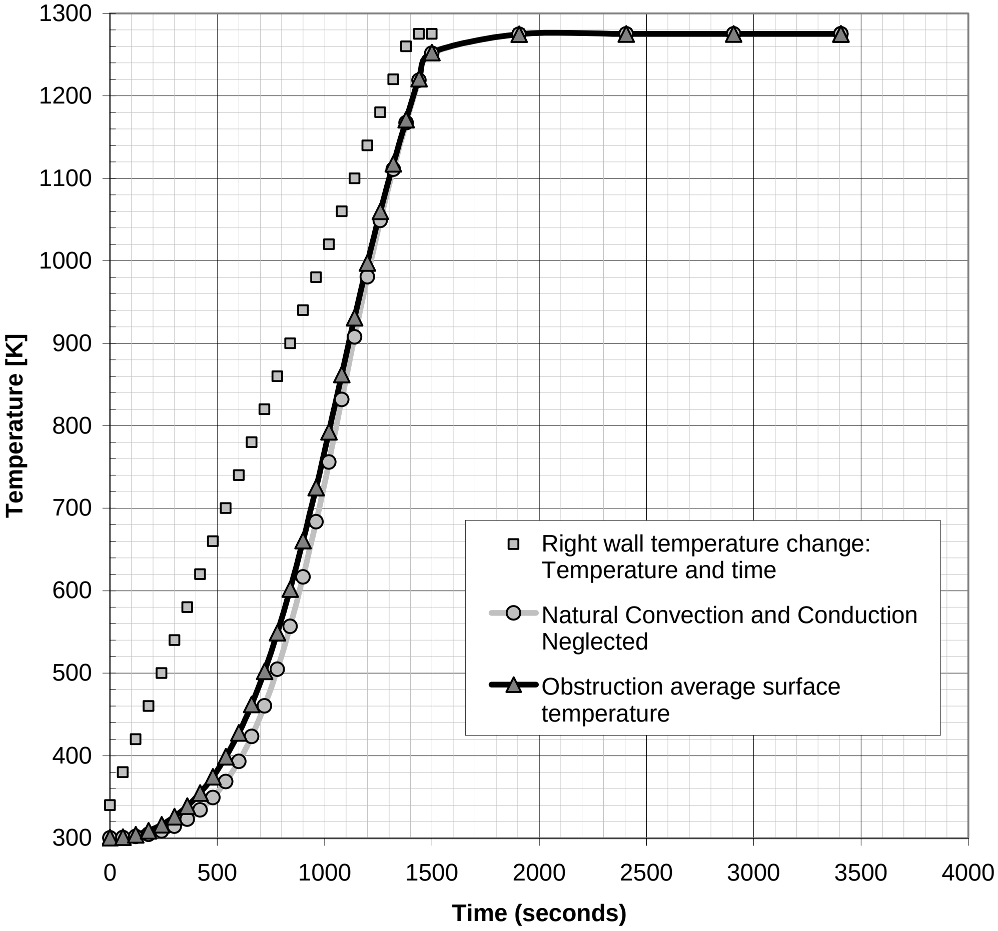

Figure 27: Right boundary temperature stepping results on obstructions average surface temperature: 2D, aspect ratio 1/3, shaft ratio 2/5

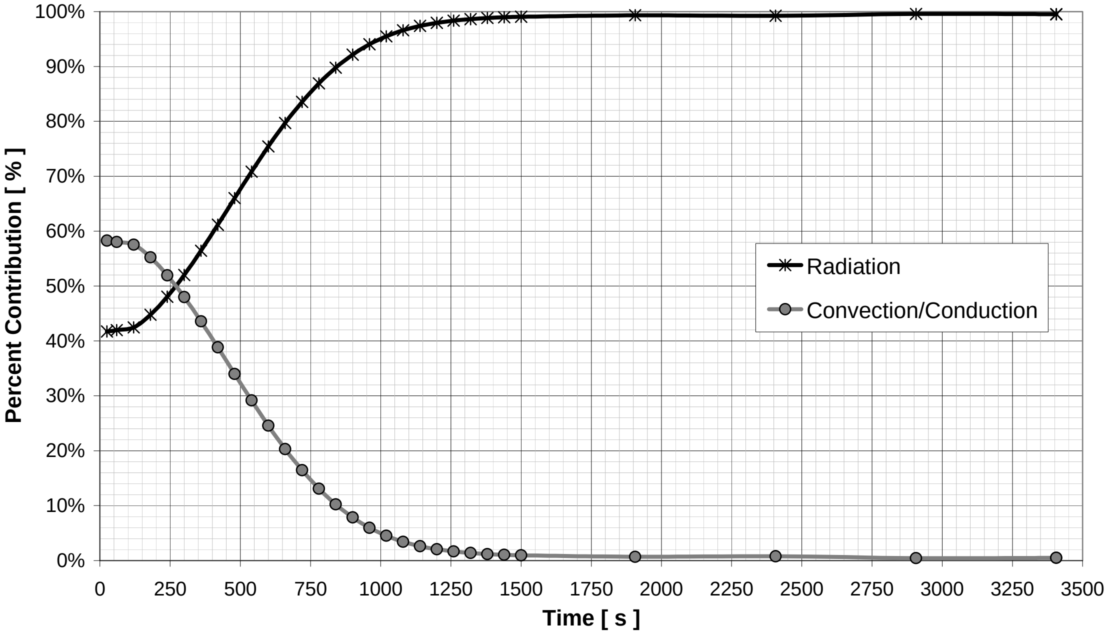

Figure 28: Right boundary temperature stepping effects on percent radiation contribution to the obstruction

Percent heat flux contributions in Figure 28 look different than those shown in Figure 47 through Figure 62. A reason for this is that the data points are taken at different time save locations. Figure 47 through 62 have a time save close to the start at 0.1 seconds. Also, the right boundary temperature in Figure 27 is changing so it should be a compilation of the results in Figures 47 through 62, as for it is. Initially, time less than 200 seconds, the right boundary temperature is below 500 K and the radiation percent contribution is less than the other heat transfer modes contributions. At higher right boundary temperatures, radiation percent contribution is greater than the other heat transfer modes contributions.

Figures 27 and 28 show the importance of natural convection at lower right boundary temperatures in terms of the slower obstruction temperature response. The maximum percent difference between the all heat transfer modes included simulation and the natural convection and conduction heat transfer modes neglected simulation is 8.06%. This fairly low difference, below 10%, indicates ignoring natural convection and conduction from the simulation produces acceptable results to estimate the obstruction temperature response. The approximation is acceptable because the system does not stay at low temperatures, below 500 K, for significant amounts of time before the right boundary temperature reaches values, above 800 K, where radiation dominates the heat transfer.

Results for the heat transfer coefficients are limited. The obstruction's time averaged heat transfer coefficient is 6.82 W/m^{2}K, while the right boundary's was 5.78 W/m^{2}K. No Nusselt to Rayleigh correlations are possible for the result data set because the data plots in a manner that curves back on itself. A function is defined as a grouping of data that given a single independent value there will be a dependent value. For the Nusselt and Rayleigh data set, certain Rayleigh values have two possible corresponding Nusselt values. Changes in the right boundary temperature, problems with the bulk fluid temperature value, and transient temperature response of the fluid are likely culprits for this problem.

CHAPTER V

DETAILED DISCUSSION

This chapter provides a more detailed discussion of the results presented in Chapter IV. Ordering in Chapter V is similar to Chapter IV: obstruction average surface temperature and percent difference, percent radiation contribution for heat transfer to the obstruction, maximum fluid velocities and model temperature distributions, and heat transfer coefficients.

5.1 Obstruction Area Averaged Surface Temperature and Percent Difference

One aspect of interest for the average surface response is the time it takes for simulations to reach a condition where the obstruction is close to the same temperature as the set temperature boundary. Simulations with the right boundary temperature below 600 K, all heat modes included, aspect ratio 1/3, and shaft ratio 2/5, do not reach the point where they approach closely to the right boundary temperature within an hour.

Because not all simulations reached the final temperature in the allotted time, time constants are used to represent the temperature response. Time constants, τ, are the time it takes a parameter to reach 63% of the response from the initial condition to the final condition for a constant input parameter. Temperature response curves for the obstruction can be generically written as equation (5.1), which can be rewritten as equation (5.2) to solve for the time constant.

$$T_s = \left(T_R - T_o\right)\left(1 - e^{\frac{t}{\tau}}\right) + T_o \qquad (5.1)$$

$$\tau = \frac{-t}{\ln\left(1 - \frac{(T_s - T_o)}{(T_R - T_o)}\right)} \tag{5.2}$$

The average surface temperature associated with a given time constant is:

$$T_s = (T_R - T_o)0.63 + T_o \tag{5.3}$$

T_s is the average surface temperature, T_R is the right boundary temperature, T_o is the initial temperature, t is the time, and τ is the time constant. The figures on pages 116-123 are used to determine the time associated with the temperature given by equation (5.3). Table 11 summarizes the time constants for all heat transfer modes included, while Table 12 and 13 are for natural convection neglected and conduction neglected respectively.

Table 11: Time Constants for All Heat Transfer Modes Included

T_R [K]	AR	SR	Geometry	Time [s]	τ [s]
310	1/3	2/5	2d	2600	2615.0
500	1/3	2/5	2d	1050	1056.1
600	1/3	2/5	2d	775	779.5
800	1/3	2/5	2d	390	392.3
950	1/3	2/5	2d	290	291.7
1100	1/3	2/5	2d	200	201.2
1275	1/3	2/5	2d	125	125.7
600	1/4	2/5	2d	825	829.8
600	1/2	2/5	2d	700	704.1
600	1/3	1/5	2d	250	251.5
600	1/3	3/5	2d	1550	1559.0
310	1/3	2/5	3d	N/A	N/A
500	1/3	2/5	3d	1050	1056.1
600	1/3	2/5	3d	800	804.6
950	1/3	2/5	3d	300	301.7
1275	1/3	2/5	3d	130	130.8

Table 12: Time Constants for Natural Convection Neglected

T_R [K]	AR	SR	Geometry	Time [s]	τ [s]
310	1/3	2/5	2d	3300	3319.1
500	1/3	2/5	2d	1400	1408.1
600	1/3	2/5	2d	925	930.4
800	1/3	2/5	2d	450	452.6
950	1/3	2/5	2d	290	291.7
1100	1/3	2/5	2d	200	201.2
1275	1/3	2/5	2d	125	125.7
600	1/4	2/5	2d	1005	1010.8
600	1/2	2/5	2d	825	829.8
600	1/3	1/5	2d	300	301.7
600	1/3	3/5	2d	1875	1885.8

Table 13: Time Constants for Conduction Neglected

T_R [K]	AR	SR	Geometry	Time [s]	τ [s]
310	1/3	2/5	2d	N/A	N/A
500	1/3	2/5	2d	1600	1609.3
600	1/3	2/5	2d	1005	1010.8
800	1/3	2/5	2d	475	477.8
950	1/3	2/5	2d	290	291.7
1100	1/3	2/5	2d	200	201.2
1275	1/3	2/5	2d	125	125.7
600	1/4	2/5	2d	1100	1106.4
600	1/2	2/5	2d	925	930.4
600	1/3	1/5	2d	N/A	N/A
600	1/3	3/5	2d	2050	2061.9

The time constants show how rapidly the average surface temperature response changes for an increase in right boundary temperature. Higher right boundary temperatures result in a faster thermal response and have lower time constants. Also, the time constants show how the three-dimensional simulations took more time to reach the final temperature than the two-dimensional simulations. Simulations like the three-dimensional simulation with right boundary temperature 310 K have N/A (Not Available) recorded because the average surface temperature never reached 63% of the final value in the recorded time.

Time constants are larger for the simulations with heat transfer modes neglected. Visually inspecting the time dependent temperature profiles in Appendix C, the trends for time constants with heat transfer modes neglected are similar to those with all modes included. Increasing the right boundary temperature decreases the time constant. Step temperature changes on the right boundary really show the effects of what the time constants represent.

Step changing the right boundary temperature causes a change in the rate the obstruction's temperature changes (Figure 27). Lower right boundary temperatures have a lower rate of change in the obstructions temperature: smaller slope on temperature response. As the right boundary temperature increases, the rate of temperature change increases in the obstruction. This trend continues till about 700 seconds when the right boundary temperature is 780 K and the obstruction temperature is about 500 K. At this point the obstruction temperature increases at nearly a constant rate of change greater than the 40 K/min rate of change on the right boundary. At 1440 seconds, when the right boundary temperature reaches the limit temperature 1275 K, the obstruction temperature has reached within 55 K of the right boundary temperature. From this point, the obstruction temperature converges to the right boundary temperature in about 460 seconds.

Data from the stepping simulation show that the obstruction and fluid are at lower temperatures where natural convection contributes over 50% to the heat transfer for over four minutes, and the right boundary temperature is below 500 K for five minutes. After the right boundary has reached a high temperature, 900 K in the stepping simulation, radiation is the dominant heat transfer mode contributing over 90% of the heat transfer and the other modes may be neglected. In the overall problem, radiation dominated allowing natural convection and conduction to be ignored even at the lower temperatures producing a maximum percent temperature difference of 8.06%.

An important part of this research is the investigation of the relative magnitudes of natural convection and radiation in three-dimensional models. Three-dimensional simulation temperature responses are similar to the two-dimensional simulations at first glance, but close inspection reveals a major difference. At lower temperatures, i.e. 310 K, the average surface temperatures of the obstruction in the three-dimensional simulation are significantly lower than the obstruction temperatures in the two-dimensional simulations (Figures on pages 116-123 in Appendix C). Three-dimensional simulations with right boundary temperatures higher than 310 K have longer temperature response times than the two-dimensional counterpart. This fact is harder to see from the figures on pages 116-123, but the time constants in Table 11 aid in identifying the trend.

Obstruction temperatures at times above 3000 seconds, figures on page 117 (top) and page 122 (bottom), also show how the three-dimensional simulations take longer to converge to the right boundary temperature. These two figures are for a right boundary temperature of 600 K, aspect ratio of 1/3, and a shaft ratio of 2/5. Where the two-dimensional simulation is effectively converged to the right boundary temperature at 3500 seconds (page 117, top), the three-dimensional model is still several degrees below the right boundary temperature (page 122, bottom). Possible causes for the slight difference is the modeling of the heat transfer through the fluid and the radiation coming to the front and back boundaries from the right boundary. In the two-dimensional model, there are not front and back boundaries, leaving only the top, left, and bottom boundaries heated along with the obstruction.

At low temperatures like 310 K, natural convection is a significant heat transfer mode, contributing over 50% to the heat transfer for over 16 minutes. For natural convection heat transfer mode, the right boundary supplies significant amounts of heat into the fluid compared to the amount of radiation emitted. At low right boundary temperatures, the radiation into the system is reduced, causing the amount of heating on the other boundaries to be lower. The result of this is the boundaries do not transfer as much heat into the fluid, which in turn lowers the heating of the obstruction. At higher right boundary temperatures, the other adiabatic boundaries are heated through radiation. The heated boundaries conduct energy into the fluid in proportion to the radiation influx and adiabatic boundary conditions. The heated fluid then transfers energy to the obstruction. This is why higher right boundary temperatures are close to the same obstruction temperatures while lower right boundary temperatures are not.

All three-dimensional simulations are run with all heat transfer modes included. Results for the two-dimensional simulations, especially those using higher right boundary temperatures, are scalable to the three-dimensional models. In general, the right boundary temperature has a large effect on the maximum percent difference in obstruction temperatures given heat transfer modes neglected. With buoyancy turned off (neglecting natural convection), the maximum percent difference appears to form an exponentially decreasing curve for right boundary temperatures of 600 K and higher (Figure 29). The error in temperature for a right boundary temperature of 310 K appears to be low. This may be caused by the percent difference formulation and the small temperature range the obstruction traverses through. With conduction neglected in the fluid, the exponentially decaying curve is clear for the entire range of right boundary temperature.

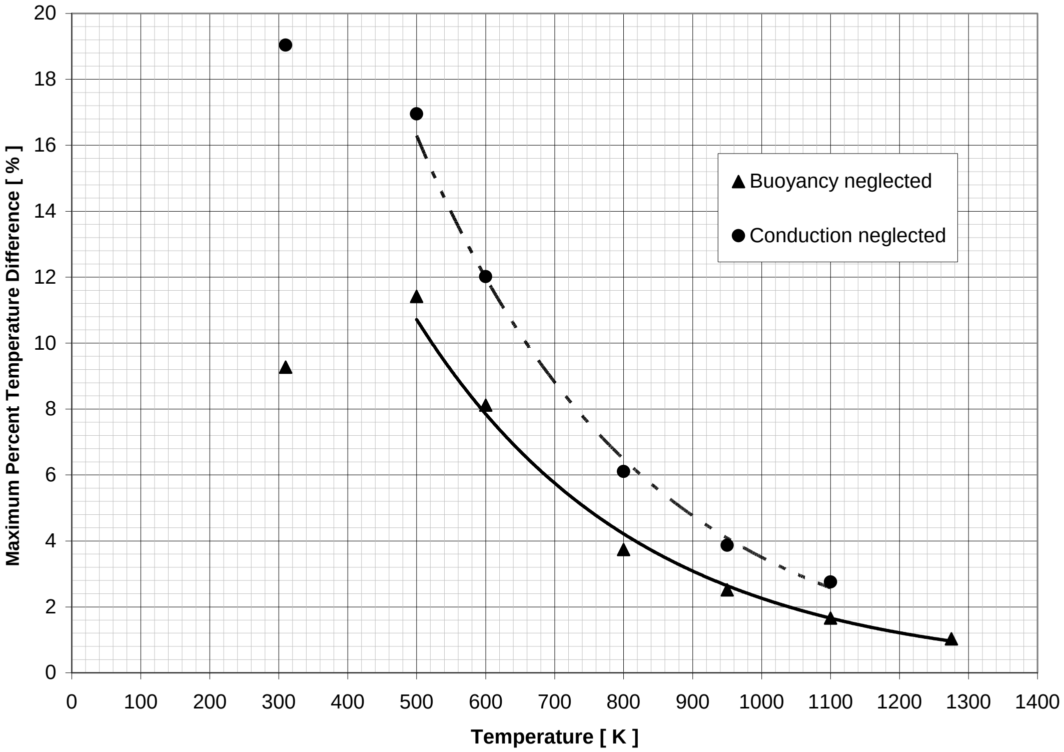

Figure 29: Percent temperature difference: two-dimensional simulations, aspect ratio 1/3, and shaft ratio 2/5

The significance of the exponential decaying curves is that for a transient right boundary temperature, the percent difference may start out large, but as the right boundary temperature increases, the percent temperature difference will decrease to a point where a heat transfer modes may be neglected. This supports a two step analysis hinted at earlier in this section. Start the simulation with natural convection included: this is a time where the error is large for neglecting natural convection. Towards the end of the simulation, neglect the heat transfer mode such as natural convection: temperatures at this time should be high enough the errors should be small. This method is intended for use when the right boundary temperatures change slowly, less than 40 K/min, and the error is expected to be greater than 10%.

The geometry affects the error. Data for this conclusion is in Table 5. Changing the aspect ratio from 1/3 to 1/4 reduces the error to 7.33% from 8.12% for no buoyancy forces. Increasing the aspect ratio from 1/3 to 1/2 increases the error for no buoyancy from 8.12% up to 8.66%. For conduction suppressed, the values are nearly the same at about 12% difference. For problems neglecting buoyancy and changing shaft ratios, the percent difference is similar to the changing aspect ratio. Suppressing conduction produces percent temperature differences 1% to 10% larger than just neglecting buoyancy. Decreasing the shaft ratios causes a 70.05% increase in the percent temperature difference, but increasing the shaft ratio reduces the error 0.18% as compared to the base case.

The best explanation for the increase in error for a smaller shaft ratio with conduction suppressed is the small shaft ratio does not blocks the radiative heat transfer to the other boundaries as much as larger shaft ratios. This means less radiation energy is directly transfer to the obstruction and the temperature response is slower.

Defining the percent difference is modified from the standard percent difference equation ($\%_{difference} = \frac{\phi_1 - \phi_2}{\phi_1}$) to equation (4.5).

$$\%_{difference} = \frac{\left(T_{all} - T_{neglect}\right)}{\left(T_{Right} - T_{init}\right)} \tag{4.5}$$

This change is done in the denominator to create a constant base defined by the right boundary temperature and initial temperature. Using the original percent difference equation, the denominator value changes and becomes larger as the right boundary temperature increases. Increasing denominator values in turn affect the percent differences by reducing them and skewing the results of the maximum percent difference for various temperatures to the lower simulation times.

The difference in obstruction temperatures for all heat transfer modes included and heat transfer modes neglected simulations increases with increasing right boundary temperatures, but by less than 5% for each right boundary temperature step (Table 5). Support for the use of the modified definition comes with the fact that the obstruction temperature increases faster for the higher right boundary temperatures (See figures in Appendix C). Denominator effects from the rapid increase caused by the higher right boundary temperatures mean that the denominator reaches its maximum value within 1500 second of the simulation start. This is likely to skew the percent temperature difference to times below 1500 seconds where the denominator is smaller. Also, the modified percent difference equation the right boundary temperature and initial temperature to normalize the percent difference and produce percent temperature differences that reveal where the maximum difference in temperature is between all heat modes included simulations and simulations with heat transfer modes neglected.

5.2 Heat Flux Contributions on the Obstruction

Heat fluxes on the obstruction are presented as percentages to allow comparisons for various right boundary temperatures in both two and three-dimensional configurations. Overall, the minimum percent radiation contribution can be described as a linear trend with the right boundary of 1275 K having the largest radiation contribution (Figure 30). This statement is true for both two and three-dimensional simulations.

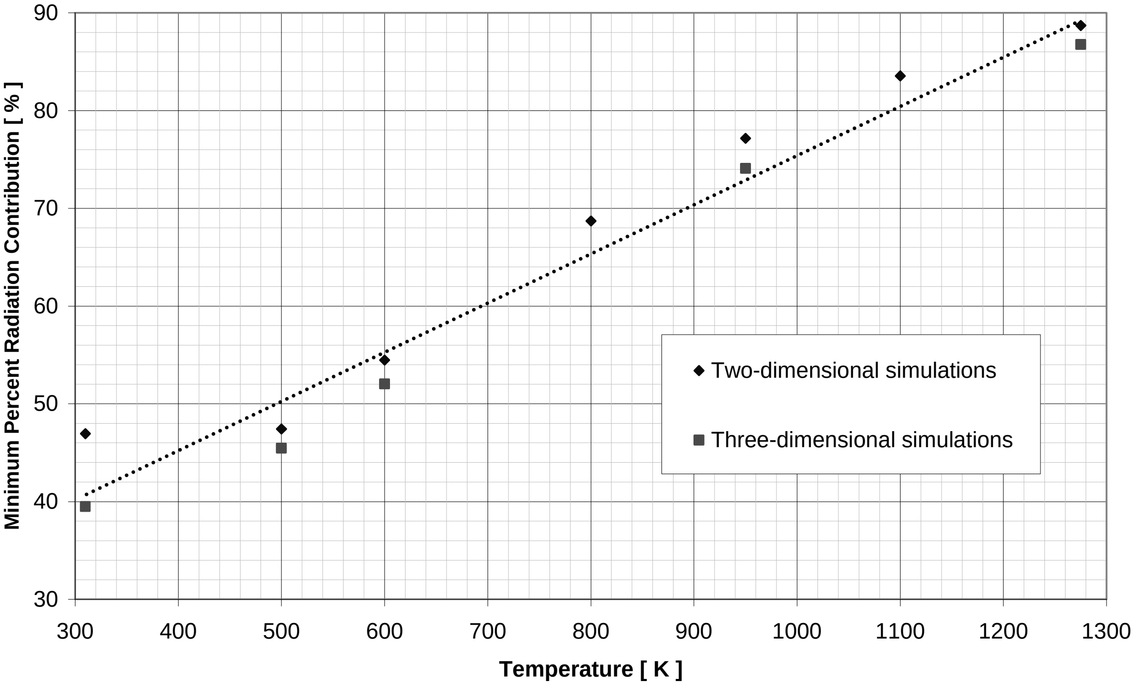

Figure 30: Minimum percent radiation contribution for aspect ratio 1/3 and shaft ratio 2/5

Trends for the percent heat flux contributions are comparable for the two and three-dimensional simulations. Initially, heat transfer comes entirely from radiation. After the fluid flow develops, the percent heat flux contributions from heat transfer modes other than radiation increase. The amount of increase is dependent on the right boundary temperature. For both the two and three-dimensional simulations, right boundary temperatures under 600 K result in the radiation percent contribution being lower than other heat transfer modes for early time. Towards the end of the simulations, the radiation heat transfer contribution increases to be the dominant heat transfer mode.

For the high right boundary temperatures of 950, and 1275 K, the percent radiation contribution drops from values over 80% to a value closer to 50% (Figures 61 and 62). This may be the result of numerical error showing more heat transfer into the obstruction than actually present. A more likely explanation is the fluid is two to three degrees warmer than the obstruction. Therefore, heat is transferred to the obstruction through the fluid. Radiation will decrease because the temperature difference is diminished. Heat flux is transferred until the system reaches the right boundary temperature.

The temperature responses for the right boundary temperatures of 950 and 1275 K (Figures 45 and 46) show that the time to approximately reach steady state are 1005.9 seconds and 504.9 seconds respectively. These times correspond to the start of the drop in percent radiation contribution (Figures 61 and 62). Observations of the obstruction temperature convergence and the drop in percent radiation contribution support the conclusion the drop is from reduced heat transfer into the obstruction from radiation and continued heat transfer through natural convection. The right boundary temperature of

600 K is on the verge of converging (Figure 44), and is thus beginning to reduce in radiation percent contribution (Figure 60) and follow the trend exhibited in the 950 and 1275 K simulations.

Concerning the values of minimum percent radiation, three-dimensional results are usually several percentage points lower than the corresponding two-dimensional simulation (see Table 6). Explaining this phenomenon are the front and back boundaries. These two boundaries are heated by radiation, and because they are adiabatic, the heat is then conducted into the fluid where it eventually heats the obstruction. Because there is more heat flux entering the fluid through the end boundaries, more heat can be conducted to the obstruction through the fluid and the percent contribution from radiation is lower.

Percent heat flux contributions for the stepping right boundary temperature coincide with the results for fixed right boundary temperatures. Coupling the stepping boundary condition with the three-dimensional simulation produces doubt about the minimum percent contribution from the two-dimensional right boundary temperature of 310 K simulation. Both the three-dimensional simulation with right boundary of 310 K and the stepping simulation had minimum percent contributions close to 40%, which match well with what is expected using a linear trend line to predict minimum percent contributions (Figure 30).

Geometry effects on the minimum percent radiation contribution are slight. Increasing or decreasing the aspect ratio from 1/3 to 1/2 or 1/4 produces a change of around 2%. Changing the shaft ratio has a slightly larger effect. The percent change is a 4% decrease for reducing the shaft ratio from 2/5 to 1/5. A 2% increase is obtained for enlarging the shaft ratio from 2/5 to 3/5. The two-dimensional models capture the minimum percent contribution from radiation for a given boundary condition. This observation is extended to the maximum velocities in the simulations.

5.3 Maximum Fluid Velocities and Model Temperatures

Maximum fluid velocities are small, usually on the order of 10^{-1} m/s or smaller. Not shown in Table 7 is that most of the maximum velocities occurred early in the simulations: 0.1 to 1.6 seconds. When a right boundary temperature stepping scheme is used, the maximum recorded velocity is at 480 seconds.

Maximum velocities between the two and three-dimensional simulations are similar. An example is the maximum velocity for a right boundary temperature of 500 K. For the two-dimensional simulation the maximum recorded velocity is 0.140 m/s, while the three-dimensional simulation has a maximum recorded velocity of 0.141 m/s. The velocity differences vary by less than 0.02 m/s for the other two and three-dimensional simulations.

Right boundary temperature appears to play a larger role in maximum velocities than geometry. Changes in the geometry’s aspect ratio affect the maximum velocity by less than 0.03 m/s. Increasing the aspect ratio increases the maximum velocity, while reducing the aspect ratio decreases the velocity. A possible reason for this is the smaller aspect ratios have longer top and bottom boundaries where shear forces hinder the flow. Shaft ratio changes have very little effect on the maximum velocity. There is only a 0.006 m/s recorded difference between the lowest and highest maximum velocities associated with shaft ratio changes.

Flow patterns in the three-dimensional simulations are more complicated than the two-dimensional simulation patterns. Due to the end boundaries, the fluid undergoes a buoyancy effect caused by heat transfer into it from the end boundaries. This in turn causes a slight funneling of fluid to the enclosure center. Shear forces and the relative small amount of heat transfer to the fluid from the end boundaries make the effect only slight. Overall, the two-dimensional simulations predict the fluid flow within the small enclosures.

Two-dimensional models also predict the temperature distribution in the small enclosures. Like the two-dimensional models, the three-dimensional models have two distinct fluid flow cells: right and left regions. Temperatures in the left region are more uniform than the right region which has warm fluid on top of a layer of cooler fluid. The right region also has larger temperature gradients. A major difference is a small thermal effect around the front and back boundaries. This effect causes the fluid to be warmer at a given x position along the boundary surface than is encountered towards the center of the enclosure at an equivalent x position. Depth of this thermal effect is not appreciable and does not appear to significantly effect the simulations. Therefore, two-dimensional simulations are reasonable approximations.

5.4 Heat Transfer Coefficients

This section discusses the heat transfer coefficients in detail. The simplest relation to use given a bulk node temperature is the time averaged heat transfer coefficients. Time averaged heat transfer coefficients range from 5.51 to 10.06 W/m^{2}K for the obstruction and 4.72 to 6.48 W/m^{2}K for the right boundary (Table 8). The mean for the obstruction is 8.01 W/m^{2}K while the median is 8.04 W/m^{2}K. Both the median and mean are similar indicating the simulation result data is distributed near the heat transfer coefficient of 8 W/m^{2}K. Heat transfer coefficients on the right boundary have a similar trend with a mean value of 5.45 W/m^{2}K and a median of 5.55 W/m^{2}K.

If a numerical model can use only one heat transfer coefficient, a value of 6.725 W/m^{2}K could prove useful as an average between the obstruction and right boundary heat transfer coefficients. Looking at the time averaged values independently, there does not appear to be a set pattern in how temperature affects the heat transfer coefficients. The same may be said about the geometry. Causes for this are not quite certain. Violations of assumptions with the bulk fluid temperature representing the entire fluid volume may be responsible for the randomness associated with the heat transfer coefficients.

Numerical error and approximations are expected in the simulations, so the data points are not expected to align perfectly. However, Figures 25 and 26 on pages 76 and 77 reveal the Nusselt-Rayleigh data points have a lot of scatter. Like the time averaged heat transfer coefficients, the problem is believed to be due to the bulk fluid temperature approximation. It is proposed that a more accurate representation of the bulk fluid temperature for regions more representative of where the heat transfer interactions are occurring will shift the curves causing them to align. This may not be realistic, because it may cause more complications in simulation preparation than simplifications.

Data in Figure 25 show higher three-dimensional Nusselt numbers than for the two-dimensional simulations for the same obstruction Rayleigh number. For the right boundary, Figure 26, the three-dimensional Nusselt numbers are lower than the two-dimensional Nusselt numbers for the same Rayleigh number. This is attributed to the end boundary effects increasing the heat transferred into the fluid.

Figures 25 and 26 also show the data forms a band, which can be line fit using an power format to obtain a Nusselt-Rayleigh correlation. R^2 values for the obstruction fit in equation (4.15) is 0.73. For equation (4.16), the R^2 value is lower at 0.48. Much of the problem with the right boundary correlation is the data resulting from after the system has started to reach a steady-state condition. Removing Rayleigh numbers below 1 changes the R^2 value to 0.67, a more acceptable value, and the correlation becomes:

$$Nu_{Right} = 3.93 * Ra_{Right}^{0.1981} \tag{5.4}$$

Equation (5.4) is limited in use for Rayleigh values between 1 and 200. Errors are also attributed to the curved region of the Nusselt-Rayleigh relation. Correlations presented in this report are useful when all that is needed is an approximate convective heat transfer coefficient or the simulation is too complicated for current computer resources and time. If boundary temperatures are expected to reach over 800 K spending only a minute or two at low temperatures like 310 K, all heat transfer modes except radiation can be neglected and the resulting obstruction temperature still be within 8% of an all modes included simulation.

CHAPTER VI

SUMMARY AND CONCLUSIONS

The research objective is to quantify the interaction of natural convection and radiation on an obstruction in a small enclosure using numerical modeling. Interaction between natural convection and radiation is investigated using temperatures and heat transfer values, which are used to formulate heat transfer coefficients, heat transfer relations using Nusselt and Rayleigh numbers, and percent heat flux contributions. Errors are used to determine if a heat transfer mode can be neglected.

6.1 Summary

Chapter I introduces the problem associated with the interaction of natural convection and radiation and provides examples of engineering problems where it is encountered. Relevant literature reviewed is presented to provide a basis for the current research and information on the computational tool is presented in detail. The research objective is also formally stated.

Computational models are covered in Chapter II. Three main topics are discussed: model geometry, time steps, and model mesh. Dimensions for the enclosure are given, as well as reasons behind the time step selection and mesh profile. Chapter III provides information on the material selection, boundary conditions, and tolerances. Nitrogen gas is used in the enclosures being simulated and also allows for radiation heat transfer to be modeled using enclosure radiation. Tolerances in FLUENT are considered to loose for natural convection and need to be tightened. Details in these chapters are important and can affect the simulation's solution.

Chapter IV presents the simulation results with brief explanations. Simulations and calculations other than from FLUENT are present to increase confidence in the FLUENT results. Average surface temperature plots for the obstruction exhibit logarithmic rise, while temperature and fluid velocity plots indicate a defined temperature profile and flow field common between the individual simulations. Results show increasing the temperature on the right boundary increases the minimum percent radiation contribution.

Results from Chapter IV are reviewed and discussed in greater detail in Chapter V. Key information out of Chapter V is the relations between the two and three-dimensional simulations. General values for time averaged heat transfer coefficients and equations for Nusselt-Rayleigh relations are also provided.

6.2 Conclusion

Interaction of natural convection and radiation is temperature dependent. At high right boundary temperatures such as 1275 K, the effect of natural convection is not appreciable on the final temperature result. At lower temperatures, less than 600 K, other modes of heat transfer can be significant. Looking at heat flux contributions, natural convection/conduction is generally appreciable for times below 500 seconds. In all of the simulations, the percent radiation heat flux contribution drops below 90% at some time. Simulations with right boundary temperatures greater than 800 K have heat transfer that is dominated by radiation and the obstruction temperature response is not appreciably affected by natural convection/conduction heat transfer (Figures 34 through 37). For simulations of this nature all modes of heat transfer except radiation can be neglected.

In a full system analysis, the right boundary temperature will undergo a transient response. During the temperature response time, the right boundary will pass through temperatures where natural convection/conduction is significant, contributing over 50% to the heat transfer. For this reason, a means of representing natural convection should be included in thermal numerical analysis, if more than two or three minutes are spent at the lower temperatures like 310 K. If the temperature rise on the right boundary is fast enough that the temperature is at low temperatures, below 800 K, for less than 12 minutes, all heat transfer modes except radiation may be neglected in order to simplify the simulations. For these cases, the error in obstruction temperature is less than 8.06% temperature difference. The stepping simulation is an example where the temperature change is rapid enough to have only an 8.06% max temperature difference with natural convection and conduction are neglected.

A convenient method to model natural convection is to use a time averaged heat transfer coefficient and a bulk fluid temperature. Recommended values for the obstruction and right boundary are 8 and 5.5 W/m^2K respectively. If only one heat transfer coefficient may be used for the fluid, the value of 6.725 W/m^2K provides a compromise for both the right boundary and obstruction.

6.3 Follow-up Work

Violations of the approximation of uniform temperature associated with the bulk fluid temperature assumption remains an unresolved issue. More work is needed in either normalizing the result data, or better fluid temperature representations are needed for formulating the heat transfer coefficients and Rayleigh numbers. One possible temperature representation is to break the fluid into four zones, each with their own average temperature. These temperatures would then be used in calculations for the boundaries they are next to. This method might work for simple model configurations, but would be cumbersome or impractical for more complicated models. Obstruction geometries other than simple circles and cylinders should be investigated. This will change the viewfactor blocking and affect the radiation heat transfer. It will also likely affect the fluid flow in the system. Extended research into natural convection and radiation in small enclosures may provide more simplifying assumptions and relations for use in numerical simulations incorporating both natural convection and radiation. To verify the research results, an experiment can be conducted, but this is not considered necessary because the numerical code is benchmarked of off other experiments.

REFERENCES

Bond, J.W., Watson, K.M., and Welch Jr, J.A., 1956. *Atomic Theory of Gas Dynamics*. Addison-Wesley, Reading, Massachusetts.

Borjini, M. N., Mbow, C., and Daguenet M. 1999. Numerical analysis of the effect of radiation on laminar steady natural convection in a two-dimensional participating medium between two horizontal confocal elliptical cylinders. *Numerical Heat Transfer Part A* 35: 467-494.

Duluc, M. C., Xin S., and Le Quéré, P. 2003. Transient natural convection and conjugate transients around a line heat source. *International Journal of Heat and Mass Transfer*, 46: 341-354.

FLUENT, 1998, *FLUENT 5 User's Guide*. Fluent Inc. Lebanon New Hampshire.

Fusegi, T., and Farouk, B. 1989. Laminar and turbulent natural convection-radiation interactions in a square enclosure filled with a non-gray gas. *Numerical Heat Transfer Part A* 15: 303-322.

Fusegi, T., Ishii, K., Farouk, B., and Kuwahara, K., 1990a, Natural convection-radiation interaction in a cube filled with a non-gray gas. In: *Advanced Computational Methods in Heat Transfer Vol 1: Heat Conduction, Convection and Radiation*, *Proceedings of the First International Conference*, pp 157-168.

Fusegi, T., Ishii, K., Farouk, B., and Kuwahara, K., 1990b. Three-dimensional study of convection-radiation interactions in a cubical enclosure field with a non-gray gas. In: *Proceedings of the Ninth International Heat Transfer Conference*, Vol. 6: pp 421-426.

Glasstone, S. and Dolan, P.J., 1977. *The Effects of Nuclear Weapons*. United States Department of Defense and United States Department of Energy.

Gustavsen, A., Griffith, B., and Arasteh, D. 2001, Natural convection effects in three-dimensional window frames with internal cavities. *ASHRAE Transactions* 107: 1-10, Cl-01-5-1.

Han, C., and Baek, S. 2000. The effects of radiation on natural convection in a rectangular enclosure divided by two partitions," *Numerical Heat Transfer, Part A*, 37: 249-270.

Holman, J.P., 2002. *Heat Transfer: Ninth Edition*. McGraw Hill, New York.

Hsieh, S. S., and Yang, S. S. 1996. Transient three-dimensional natural convection in a rectangular enclosure. *International Journal of Heat and Mass Transfer*, 39 (1): 13-26.

Incropera, F. P., and DeWitt, D. P. 1996. *Fundamentals of Heat and Mass Transfer*. John Wiley and Sons, New York.

Khalifa, A. J., and Abdullah, S. E. 1999. Buoyancy driven convection in undivided and partially divided enclosures. *Energy Conservation and Management*, 40: 717-727.

Kohno, H., and Tanahashi, T., 2002. Finite element simulation of single crystal growth process using GSMAC method. *Journal of Computational and Applied Mathematics*, 149: 359-371.

Krishnaprakas, C. K., and Narayana K. B, 1999. Interaction of radiation with natural convection. *Journal of Thermophysics*, 13 (3): 387-390

Lei, C. and Patterson, J. C., 2001. A direct three-dimensional simulation of radiation-induced natural convection in a shallow wedge. *International Journal of Heat and Mass Transfer*, 46: 1183-1197.

Lei, C. and Patterson, J. C., 2002. Natural convection in a reservoir sidearm subject to solar radiation: A two-dimensional simulation. *Numerical Heat Transfer, Part A* 42: 13-32.

Li, X., and Durbetaki, P., 1990. Transient natural convection boundary layer induced by radiant heating. In: *Advanced Computational Methods in Heat Transfer Vol. 2: Natural and Forced Convection*, *Proceedings of the First International Conference*, pp 135-146.

Mills, A. F. 1999. *Heat Transfer* second edition, Prentice Hall, Euglewood Cliffs, New Jersey.

Moen, C. D., Evans, G. H., Domino, S. P., and Burns, S. P. 2002. A multi-mechanics approach to computational heat transfer. In: *Proceedings of ASME International Mechanical Engineering Congress and Exhibition*. pp 1-8.

Ramesh, N. and Venkateshan, S. P., 1999. Effect of surface radiation on natural convection in a square enclosure. *Journal of Thermophysics and Heat Transfer*, 13 (3): 299-301.

Ratzel, A.C., and Howell, J.R., 1982. Two-dimensional energy transfer in radiatively participating media with conduction by the P-N approximation. In: *Proceedings of the Seventh International Heat Transfer Conference*, Vol. 2, pp 535-540.

Raycraft, J., Kelleher, M. D., Yang, H. Q., and Yang, K. T., 1990. Fire spread in a three-dimensional pressure vessel with radiation exchange and wall heat loss. *Mathematical Computational Modeling*, 14: 795-800.

Velusamy, K., Sundararajan, T., and Seetharamu, K., 2001. Interaction effects between surface radiation and turbulent natural convection in square and rectangular enclosures. *Journal of Heat Transfer*, 123: 1062-1070.

Yang, K.T., 1986. Numerical modeling of natural convection-radiation interaction in enclosures. In: *Proceedings of the Eighth International Heat Transfer Conference*, Vol. 1, pp 131-140.

Yücel, A., and Acharya, S., 1990. Combined natural convection and radiation in partitioned enclosures. In: *Proceedings of the Ninth International Heat Transfer Conference, Vol.* 6, pp 445-450.

APPENDIX A

TURBULENT FLOW VELOCITY CALCULATION

Calculations using the Reynolds number are used to determine velocities necessary for turbulent flow. Turbulent flow is assumed to occur at the Reynolds number of $5*10^5$.

$$\mathrm{Re} \equiv \frac{\rho V L}{\mu}$$

Solving for velocity produces

$$V = \frac{\mathrm{Re}\,\mu}{\rho L}$$

The fluid is nitrogen, and the critical length, L, is specified as 0.0254 m.

ρ=1.138 kg/m^3
μ=1.663*10^{-5} kg/m-s

$$V = \frac{5*10^5 *1.663*10^{-5}\left[\frac{kg}{m-s}\right]}{0.0254[m]*1.138\left[\frac{kg}{m^3}\right]} = 287.66\left[\frac{m}{s}\right]$$

Therefore, a velocity of 287.66 m/s is needed in the example for the flow to become turbulent.

APPENDIX B

NET RADIATION METHOD: DERIVATION AND MATLAB CODE

Equation derivation:

A basic equation for the net radiation method is:

$$\sum_{j=1}^{N}\left(\frac{\delta_{kj}}{\varepsilon_j} - F_{kj}\frac{1-\varepsilon_j}{\varepsilon_j}\right)\frac{Q_j}{A_j} = \sum_{j=1}^{N}\left(\delta_{kj} - F_{kj}\right)\sigma T_j^4$$

In this equation, δ_{kj} is 1 when k=j and 0 otherwise. ε is the emissivity of a surface, Q is the heat transfer, A is the area, N the number of surfaces, F the viewfactors, σ is Boltzmann's constant, and T is the surface temperatures.

The simple model used is a five surface enclosure with each boundary represented by a number. Surface 1 is the right boundary, surface 2 is the top boundary, surface 3 is the left boundary, surface 4 is the bottom boundary, and the obstruction's surface is surface 5. Placement of the surfaces is shown graphically on page 34 in Figure 10.

Boundary conditions and known values are:

T1=Constant
Q2=0
Q3=0
Q4=0

F11=0
F22=0
F33=0
F44=0
F55=0

Expanding the net radiation method equation for the five surfaces using the known values and conditions produce 5 equations with 5 unknowns if viewfactors are considered known.

$$\frac{Q_1}{\varepsilon_1 A_1} - F_{15}\frac{(1-\varepsilon_5)Q_5}{\varepsilon_5 A_5} = \sigma T_1^4 - F_{12}\sigma T_2^4 - F_{13}\sigma T_3^4 - F_{14}\sigma T_4^4 - F_{15}\sigma T_5^4$$

$$-F_{21}\frac{(1-\varepsilon_1)Q_1}{\varepsilon_1 A_1} - F_{25}\frac{(1-\varepsilon_5)Q_5}{\varepsilon_5 A_5} = -F_{21}\sigma T_1^4 + \sigma T_2^4 - F_{23}\sigma T_3^4 - F_{24}\sigma T_4^4 - F_{25}\sigma T_5^4$$

$$-F_{31}\frac{(1-\varepsilon_1)Q_1}{\varepsilon_1 A_1} - F_{35}\frac{(1-\varepsilon_5)Q_5}{\varepsilon_5 A_5} = -F_{31}\sigma T_1^4 - F_{32}\sigma T_2^4 + \sigma T_3^4 - F_{34}\sigma T_4^4 - F_{35}\sigma T_5^4$$

$$-F_{41}\frac{(1-\varepsilon_1)Q_1}{\varepsilon_1 A_1} - F_{45}\frac{(1-\varepsilon_5)Q_5}{\varepsilon_5 A_5} = -F_{41}\sigma T_1^4 - F_{42}\sigma T_2^4 - F_{43}\sigma T_3^4 + \sigma T_4^4 - F_{45}\sigma T_5^4$$

$$-F_{51}\frac{(1-\varepsilon_1)Q_1}{\varepsilon_1 A_1} + \frac{Q_5}{\varepsilon_5 A_5} = -F_{51}\sigma T_1^4 - F_{52}\sigma T_2^4 - F_{53}\sigma T_3^4 - F_{54}\sigma T_4^4 + \sigma T_5^4$$

These equations are rearranged to solve for the unknown terms in reference to the known values and converted into a matrix.

$$\begin{bmatrix} \frac{1}{\varepsilon_1 A_1} & F_{12}\sigma & F_{13}\sigma & F_{14}\sigma & -F_{15}\frac{(1-\varepsilon_5)}{\varepsilon_5 A_5} \\ -F_{21}\frac{(1-\varepsilon_1)}{\varepsilon_1 A_1} & -\sigma & F_{23}\sigma & F_{24}\sigma & -F_{25}\frac{(1-\varepsilon_5)}{\varepsilon_5 A_5} \\ -F_{31}\frac{(1-\varepsilon_1)}{\varepsilon_1 A_1} & F_{32}\sigma & -\sigma & F_{34}\sigma & -F_{35}\frac{(1-\varepsilon_5)}{\varepsilon_5 A_5} \\ -F_{41}\frac{(1-\varepsilon_1)}{\varepsilon_1 A_1} & F_{42}\sigma & F_{43}\sigma & -\sigma & -F_{45}\frac{(1-\varepsilon_5)}{\varepsilon_5 A_5} \\ -F_{51}\frac{(1-\varepsilon_1)}{\varepsilon_1 A_1} & F_{52}\sigma & F_{53}\sigma & F_{54}\sigma & \frac{1}{\varepsilon_5 A_5} \end{bmatrix} \begin{Bmatrix} Q_1 \\ T_2^4 \\ T_3^4 \\ T_4^4 \\ Q_5 \end{Bmatrix} = \begin{Bmatrix} \sigma T_1^4 - F_{15}\sigma T_5^4 \\ -F_{21}\sigma T_1^4 - F_{25}\sigma T_5^4 \\ -F_{31}\sigma T_1^4 - F_{35}\sigma T_5^4 \\ -F_{41}\sigma T_1^4 - F_{45}\sigma T_5^4 \\ -F_{51}\sigma T_1^4 + \sigma T_5^4 \end{Bmatrix}$$

Multiplying both sides by the inverse on the first matrix, the unknowns are calculated. Q_5 is used to solve for the next time increments surface temperature on the obstruction.

$$\rho c_p V\frac{\partial T}{\partial t} = Q_5 \Rightarrow T_5^{m+1} = -\frac{\Delta t Q_5}{\rho c_p V} + T_5^m$$

Symbols in this equation represent change in time (Δt), density (ρ), specific heat (c_p), and volume of the obstruction (V). This equation comes from an energy equation with all terms except radiation heat transfer and transient internal energy neglected. Viewfactors are calculated using two predefined viewfactor equations and relations.

Viewfactors:

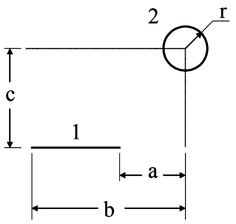

$$F_{12} = \frac{r}{b-a}\left(\tan^{-1}\left(\frac{b}{c}\right) - \tan^{-1}\left(\frac{a}{c}\right)\right)$$

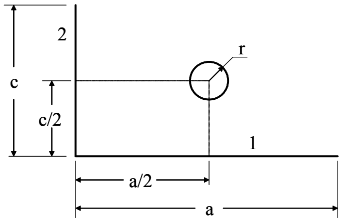

$$F_{12} = \frac{1}{2}\left[1 + \frac{c}{a} - \sqrt{1 + \left(\frac{c}{a}\right)^2 + 4\left(\frac{r}{a}\right)^2}\right]^*$$

*approximation

$$1 = \sum F_{ij} \qquad A_i F_{ij} = A_j F_{ji}$$

$$F_{12} = \frac{1}{2}\left[1 + \frac{c}{a} - \sqrt{1 + \left(\frac{c}{a}\right)^2 + 4\left(\frac{r}{a}\right)^2}\right] \qquad F_{21} = \frac{1}{2}\left[1 + \frac{c2}{a2} - \sqrt{1 + \left(\frac{c2}{a2}\right)^2 + 4\left(\frac{r}{a2}\right)^2}\right]$$

$$F_{13} = 1 - 2 * F_{12} - F_{15} \qquad F_{23} = F_{21}$$

$$F_{13} = F_{12} \qquad F_{24} = 1 - 2 * F_{21} - F_{25}$$

$$F_{15} = \frac{r}{b-a}\left(\tan^{-1}\left(\frac{b}{c}\right) - \tan^{-1}\left(\frac{a}{c}\right)\right) \qquad F_{25} = \frac{r}{b2-a2}\left(\tan^{-1}\left(\frac{b2}{c2}\right) - \tan^{-1}\left(\frac{a2}{c2}\right)\right)$$

$$F_{31} = F_{13} \qquad F_{41} = F_{21}$$

$$F_{32} = F_{12} \qquad F_{42} = F_{24}$$

$$F_{34} = F_{12} \qquad F_{43} = F_{21}$$

$$F_{35} = F_{15} \qquad F_{45} = F_{25}$$

$$F_{51} = \frac{A_1 F_{15}}{A_5} \qquad F_{52} = \frac{A_2 F_{25}}{A_5}$$

$$F_{53} = F_{51} \qquad F_{51} = F_{52}$$

MATLAB input file:

```
% This matlab m file calculates the heat transfer
%  to an object in a rectangular enclosure using
%  the net radiation method
%
% Jimmy Lloyd August 18, 2003

function qform(input);
heat_wall=input

% System parameters
stept=0.05          % time step
endt =3700          % end time
initail_temp=300        % initail system temperature
width=0.0762      % enclosure width
height=0.0254      % enclosure height
radius=0.00508     % obstruction radius
density=8030         % kg/m3
spec_h=602.48      % J/(kg K)
ep1=         0.8
ep2=         0.8
ep3=ep2;
ep4=ep2;
ep5=ep2;
sigma=        5.6685*10^(-8)
Time(1)=      0;
Time1  =      Time(1);
modv   =      1000;      % Number of data points to skip using mod function.

% set initial temperatures
Tr=heat_wall;
Ts(1)=initail_temp;
Tblack(1)=initail_temp;
Tblack1=Tblack(1);

%calculate viewfactors
Fae=radius/(height)*(atan(height/width)-atan(-height/width));
Fac=sqrt(1+(width/(height))^2)-width/height;
Fab=(1/2)*(1+(width/height)-sqrt(1+(width/height)^2));
Fde=radius/(width)*(atan(width/height)-atan(-width/height));
Fdb=sqrt(1+(height/(width))^2)-height/width;
Fac=(1/2)*(1+(height/width)-sqrt(1+(height/width)^2));
sax1=(height^3+height*width^2-4*radius^2*height+2*sqrt(-radius^2*width^2*...
    (-height^2-width^2+4*radius^2)))/(2*(width^2+height^2));
say1=sqrt(4*radius^2-4*sax1^2+4*sax1*height-height^2)/2+width/2;
sax2=(width^3 +width*height^2-4*radius^2*width +2*sqrt(-radius^2*height^2*...
    (-height^2-width^2+4*radius^2)))/(2*(width^2+height^2));
say2=sqrt(4*radius^2-4*sax2^2+4*sax2*width-width^2)/2+height/2;
SA1=radius*((atan((say1-width/2)/(sax1-height/2)))+pi) %2*pi*radius
SA2=radius*((atan((say2-height/2)/(sax2-width/2)))+pi)

F11=0
F12=(1/2)*(1+(width/height)-sqrt(1+(width/height)^2+4*(radius/height)^2))
F13=1-2*F12-Fae
F14=F12
F15=Fae
```

```
F21=(1/2)*(1+(height/width)-sqrt(1+(height/width)^2+4*(radius/width)^2))
F22=0
F23=F21
F24=1-2*F21-Fde
F25=Fde

F31=F13
F32=F12
F33=0
F34=F32
F35=F15

F41=F21
F42=F24
F43=F41
F44=0
F45=F25

F51=height*F15/SA1
F52=(1-2*F51)/2
F53=F51
F54=F52
F55=0

a=[1/(ep1*height), F12*sigma, F13*sigma, F14*sigma,...
                                  -F15*(1-ep5)/(ep5*2*pi*radius);
   -F21*(1-ep1)/(ep1*height), -sigma, F23*sigma, F24*sigma,...
                                  -F25*(1-ep5)/(ep5*2*pi*radius);
   -F31*(1-ep1)/(ep1*height), F32*sigma, -sigma, F34*sigma,...
                                  -F35*(1-ep5)/(ep5*2*pi*radius);
   -F41*(1-ep1)/(ep1*height), F42*sigma, F43*sigma, -sigma,...
                                  -F45*(1-ep5)/(ep5*2*pi*radius);
   -F51*(1-ep1)/(ep1*height), F52*sigma, F53*sigma, F54*sigma,...
                                       1/(ep5*2*pi*radius)];
d=inv(a);

Ts1=Ts(1);
g=1;

for i=2:1:endt/stept
   c=[sigma*Tr^4-F15*sigma*Ts1^4;
      -F21*sigma*Tr^4-F25*sigma*Ts1^4;
      -F31*sigma*Tr^4-F35*sigma*Ts1^4;
      -F41*sigma*Tr^4-F45*sigma*Ts1^4;
      -F51*sigma*Tr^4+sigma*Ts1^4];
   b=d*c;

   Ts2=-stept*b(5,1)/(density*spec_h*pi*radius^2)+Ts1;
   Tblack2=stept*height*sigma*(Tr^4-Tblack1^4) /      ...
                                (density*pi*radius^2*spec_h)+Tblack1;
   Time2=Time1+stept;
   if mod(i,modv) == 0
      g=g+1;
      Ts(g)=Ts2;
      Tblack(g)=Tblack2;
      Time(g)=Time2;
```

```
   end
   Ts1=Ts2;
   Tblack1=Tblack2;
   Time1=Time2;
end
% FLUENT simulation results - imported : Matlab used to spline data to
% create smooth curve
tsim =[0.1, 1.6, 4.1, 12.6, 25.1, 45.1, 70.1, 117.6, 180.1, 335.1, 505.1,...
       605.1, 1005.1, 1405.1, 1905.1, 2405.1, 2905.1, 3405.1, 3705.1];
 plot1100=[301.3945, 306.4852, 313.29077, 336.2756, 369.96936, 423.51709,...
        489.54834, 610.43042, 754.12677, 1006.213, 1075.8308, 1090.5131,...
        1099.748, 1099.9409, 1099.9801, 1099.9862, 1099.9862, 1099.9862,...
        1099.9862];
 plot950=[300.77237, 303.59201, 307.3616, 320.09396, 338.76794, 368.49722,...
        405.33548, 473.93823, 560.08777, 757.75732, 860.49628, 898.98059,...
        945.4621, 949.59937, 949.93964, 949.93964, 949.93964, 949.93964,...
        949.93964];
 plot800=[300.38458,301.78839, 303.66525, 310.00467, 319.30511, 334.12479,...
        352.53107, 387.06409, 431.39172, 545.31696, 625.87964, 668.88501,...
        764.70148, 791.71613, 798.66437, 799.73993, 799.9079, 799.92847,...
        799.92847];
 plot600=[300.11639, 300.54117, 301.1091, 303.02713, 305.84134, 310.32785,...
        315.90738, 326.41602, 340.04501, 376.79871, 406.34253, 424.86264,...
        488.10526, 533.00763, 566.9657, 584.41559, 592.80994, 596.71222,...
        597.94513];
 plot500=[300.05197, 300.24191, 300.49576, 301.35254, 302.60968, 304.6142,...
        307.10812, 311.80875, 317.9165, 334.52045, 348.12485, 356.84665,...
        388.73376, 415.51605, 441.47977, 460.11774, 473.31699, 482.37912,...
        486.3226];
 plot310=[300.00098,300.00497, 300.01022, 300.02719, 300.05179, 300.09085,...
        300.13931, 300.23093, 300.34967, 300.67355, 300.94312, 301.12439,...
        301.81323, 302.4512, 303.1922, 303.87805, 304.49524, 305.0509,...
        305.35788];
 plot1100s=spline(tsim,plot1100,0:stept:3705);
 plot950s=spline(tsim,plot950,0:stept:3705);
 plot800s=spline(tsim,plot800,0:stept:3705);
 plot600s=spline(tsim,plot600,0:stept*modv:3705);
 plot500s=spline(tsim,plot500,0:stept:3705);
 plot310s=spline(tsim,plot310,0:stept:3705);
% plot all results
plot(Time,Ts,'-r')
hold on
%set('Ylim',[0,heat_wall])
title('Obstruction Temperature for Radiation Heat Transfer',...
     'FontWeight','bold','FontSize', 14)
xlabel('Time (seconds)','FontSize', 12)
ylabel('Temperature (K)', 'FontSize', 12)
%plot(0:stept:3705,plot1100s,'--k',tsim,plot1100,'*k')
%plot(0:stept:3705,plot950s,'--k',tsim,plot950,'*k')
%plot(0:stept:3705,plot800s,'--k',tsim,plot800,'*k')
plot(0:stept*modv:3705,plot600s,'--k',tsim,plot600,'*k')
%plot(0:stept:3705,plot500s,'--k',tsim,plot500,'*k')
%plot(0:stept:3705,plot310s,'--k',tsim,plot310,'*k')
%plot(Time,Tblack,'-g')
grid on
%axis equal tight
hold off
```

APPENDIX C

OBSTRUCTION AVERAGE SURFACE TEMPERATURE PLOTS

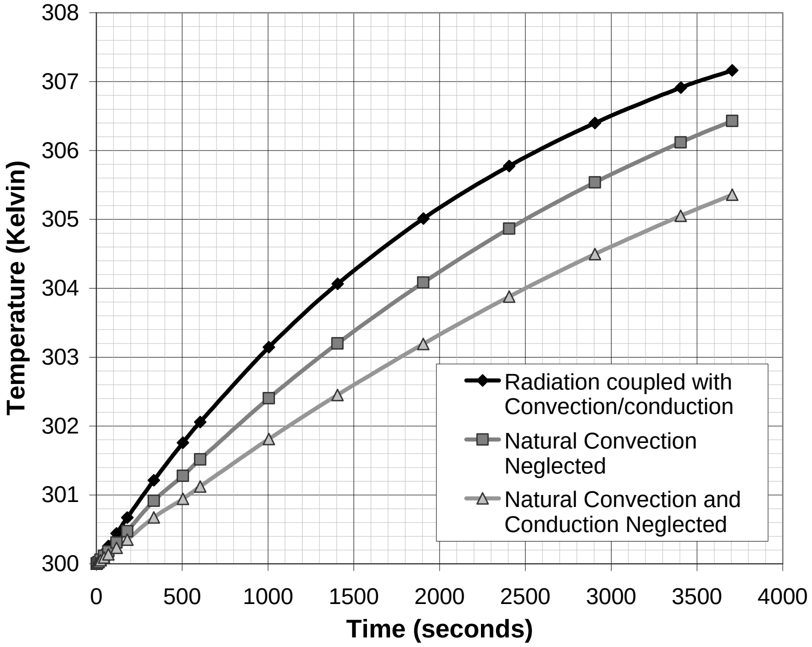

Figure 31: Obstructions average surface temperature: 2D, aspect ratio 1/3, shaft ratio 2/5, and right boundary temperature 310 K

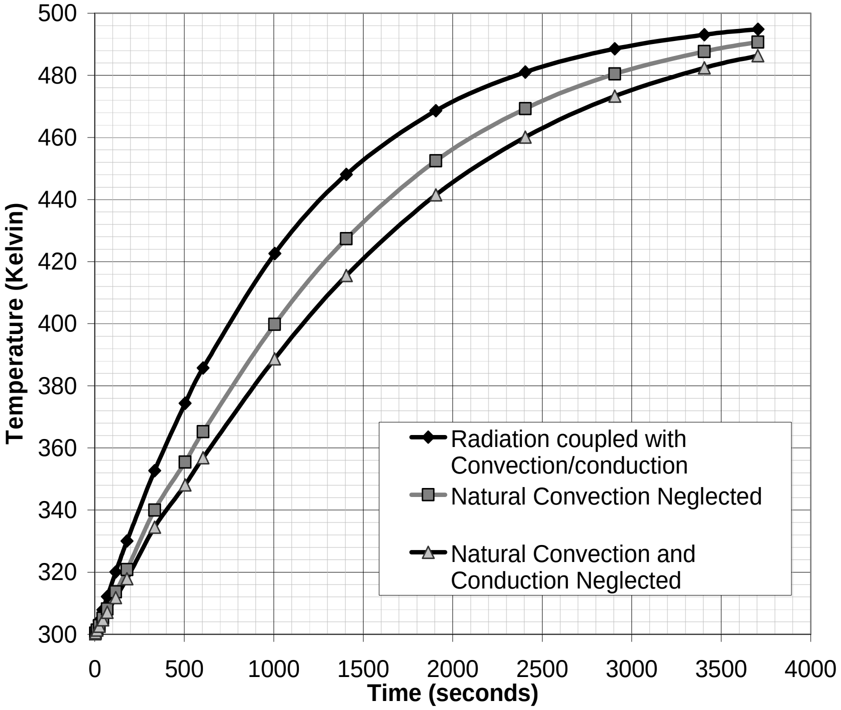

Figure 32: Obstructions average surface temperature: 2D, aspect ratio 1/3, shaft ratio 2/5, and right boundary temperature 500 K

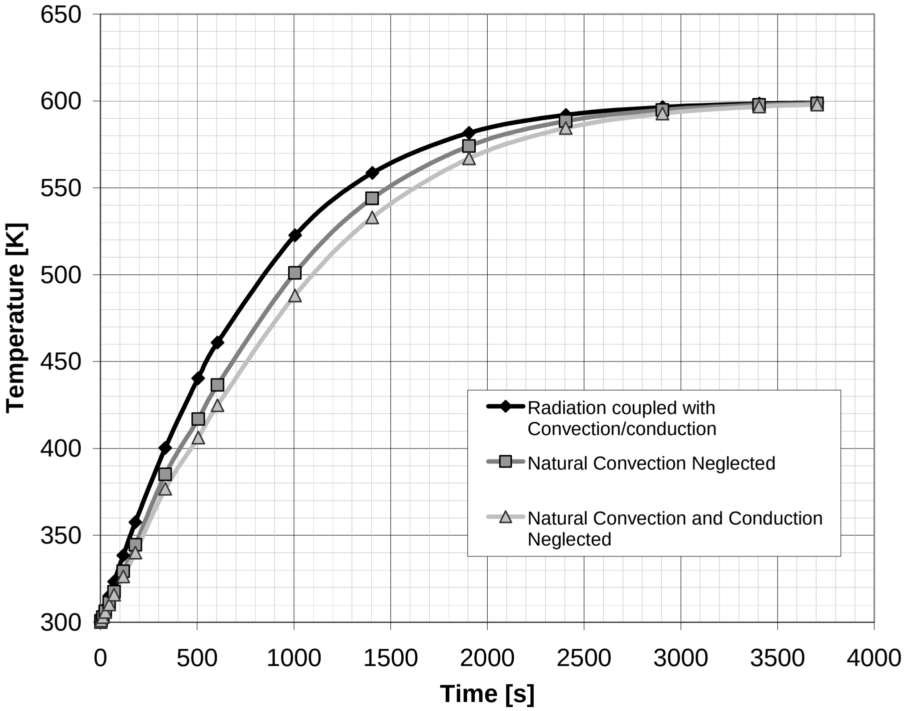

Figure 33: Obstructions average surface temperature: 2D, aspect ratio 1/3, shaft ratio 2/5, and right boundary temperature 600 K

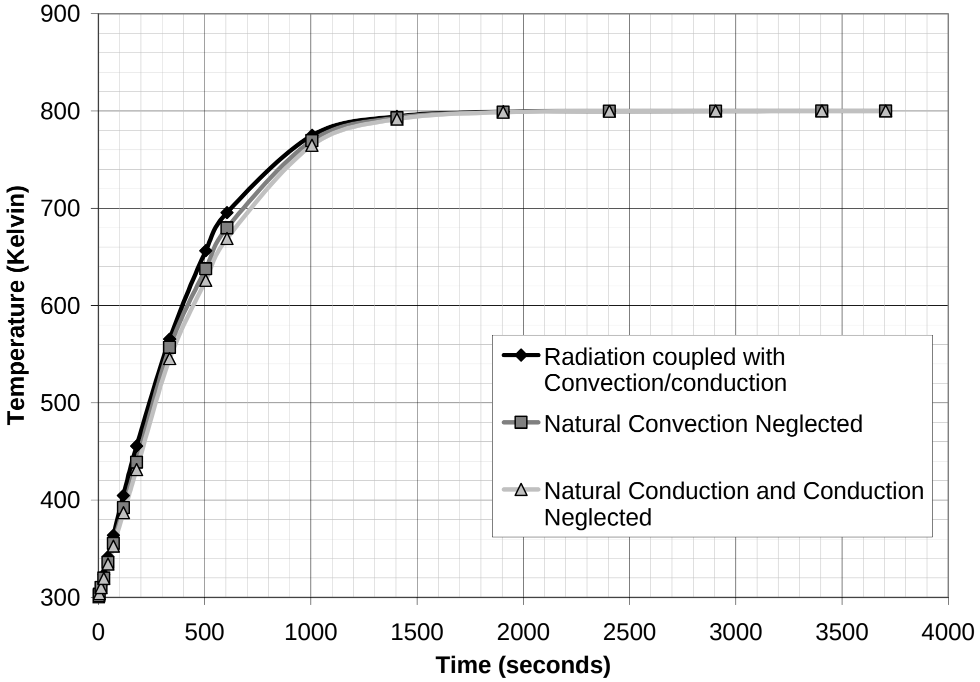

Figure 34: Obstructions average surface temperature: 2D, aspect ratio 1/3, shaft ratio 2/5, and right boundary temperature 800 K

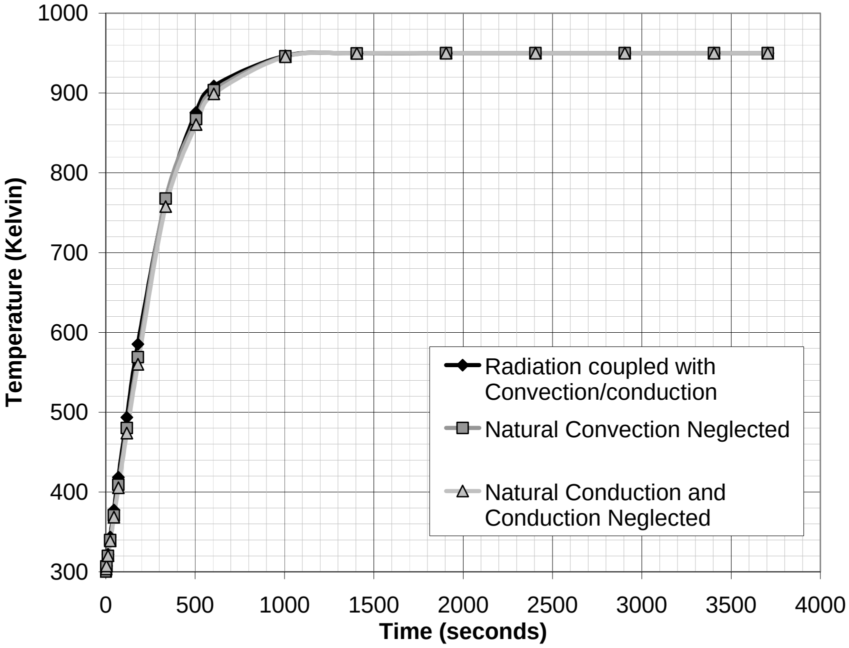

Figure 35: Obstructions average surface temperature: 2D, aspect ratio 1/3, shaft ratio 2/5, and right boundary temperature 950 K

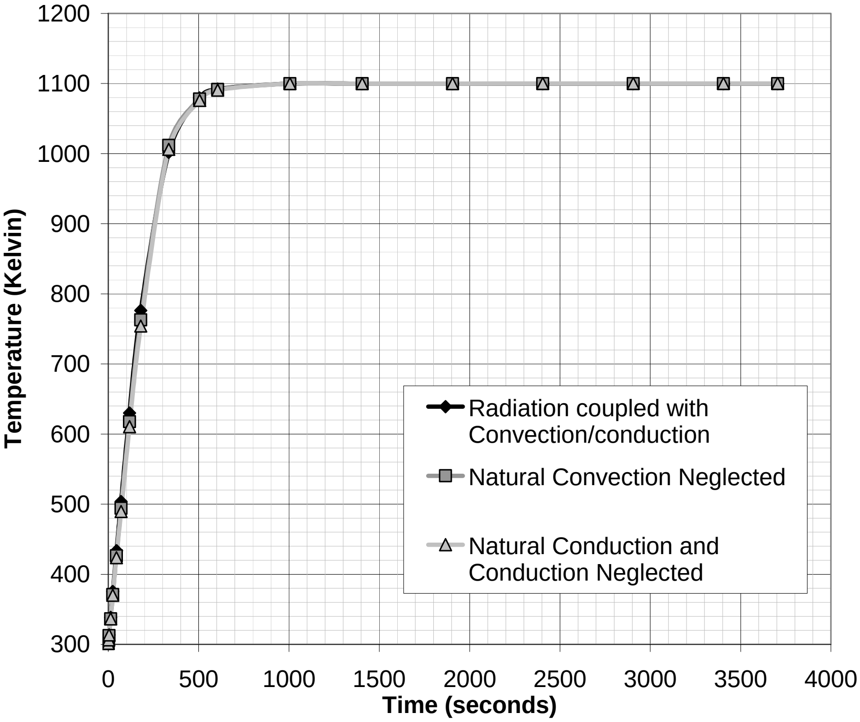

Figure 36: Obstructions average surface temperature: 2D, aspect ratio 1/3, shaft ratio 2/5, and right boundary temperature 1100 K

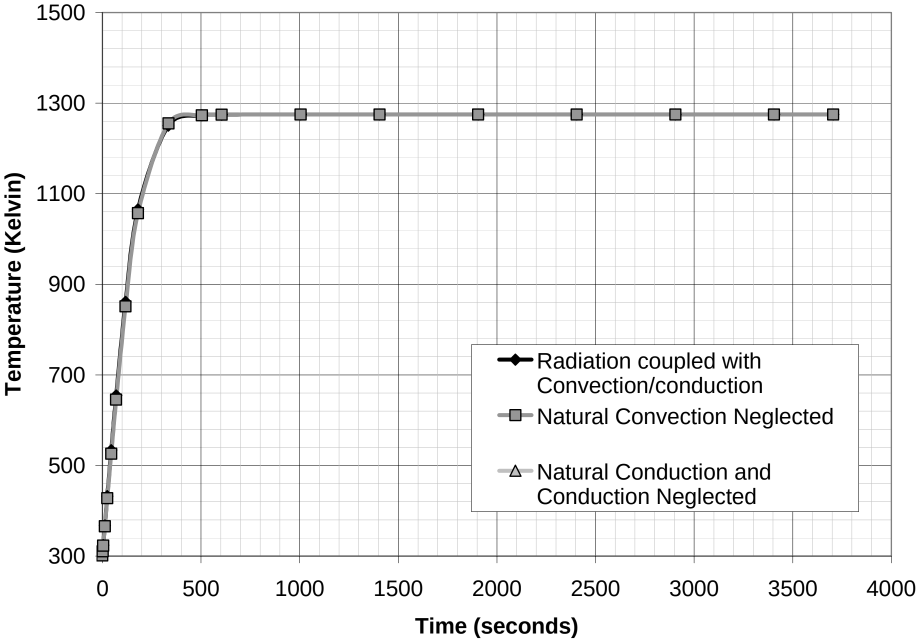

Figure 37: Obstructions average surface temperature: 2D, aspect ratio 1/3, shaft ratio 2/5, and right boundary temperature 1275 K

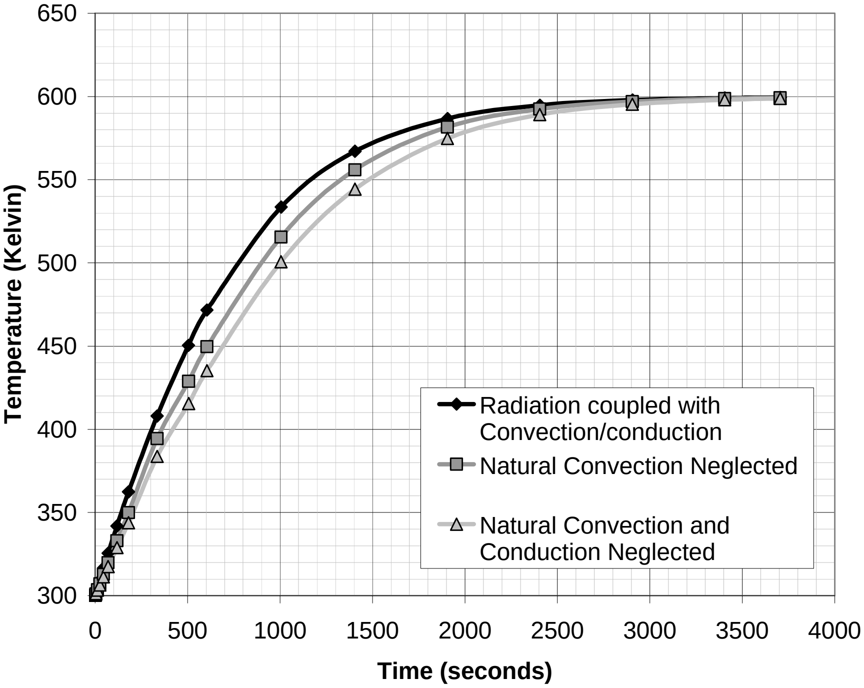

Figure 38: Obstructions average surface temperature: 2D, aspect ratio 1/2, shaft ratio 2/5, and right boundary temperature 600 K

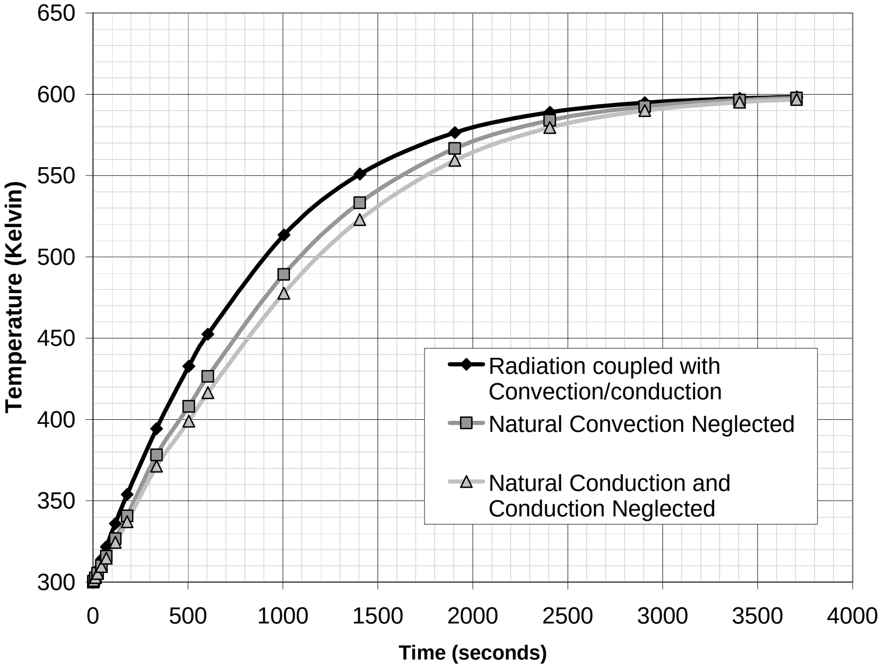

Figure 39: Obstructions average surface temperature: 2D, aspect ratio 1/4, shaft ratio 2/5, and right boundary temperature 600 K

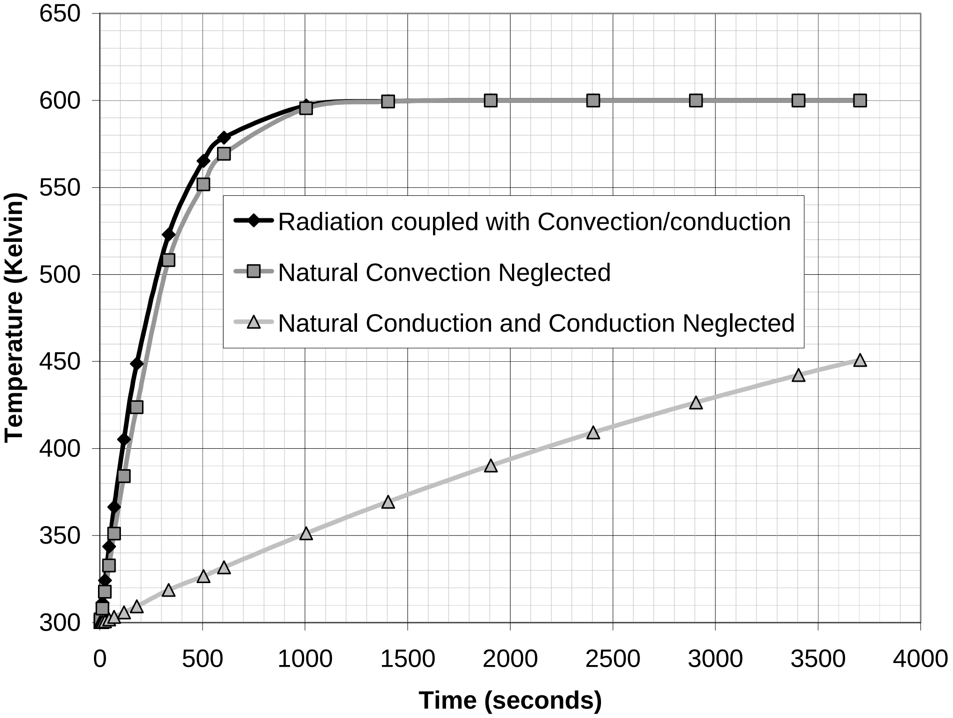

Figure 40: Obstructions average surface temperature: 2D, aspect ratio 1/3, shaft ratio 1/5, and right boundary temperature 600 K

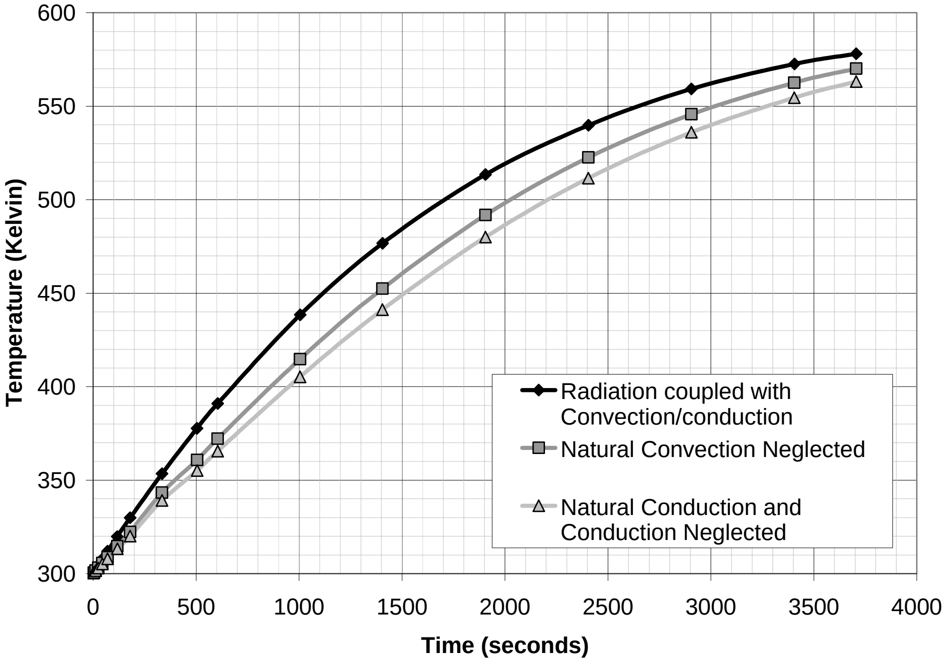

Figure 41: Obstructions average surface temperature: 2D, aspect ratio 1/3, shaft ratio 3/5, and right boundary temperature 600 K

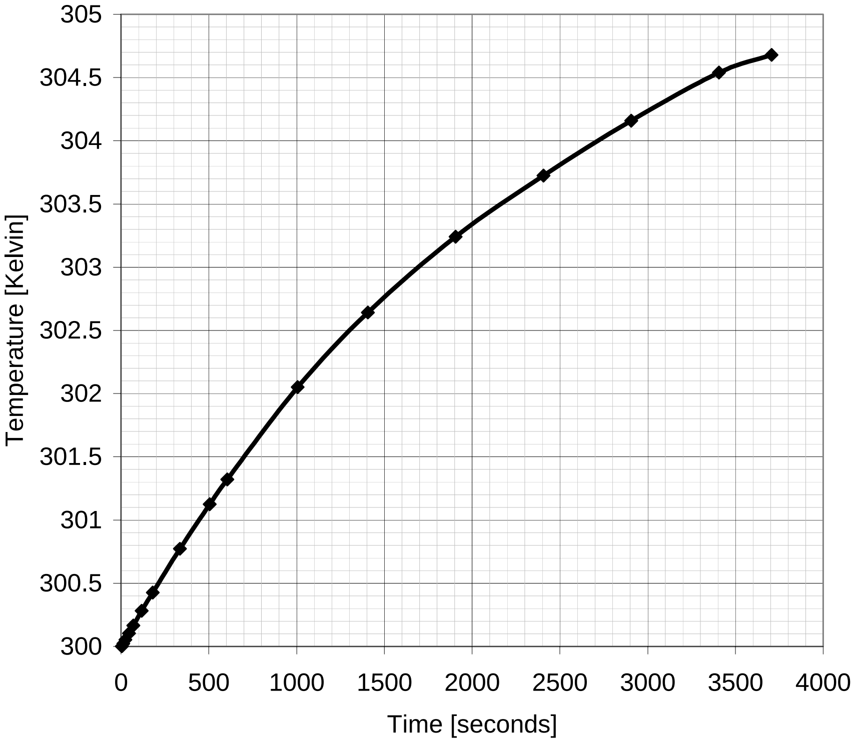

Figure 42: Obstructions average surface temperature: 3D, aspect ratio 1/3, shaft ratio 2/5, and right boundary temperature 310 K

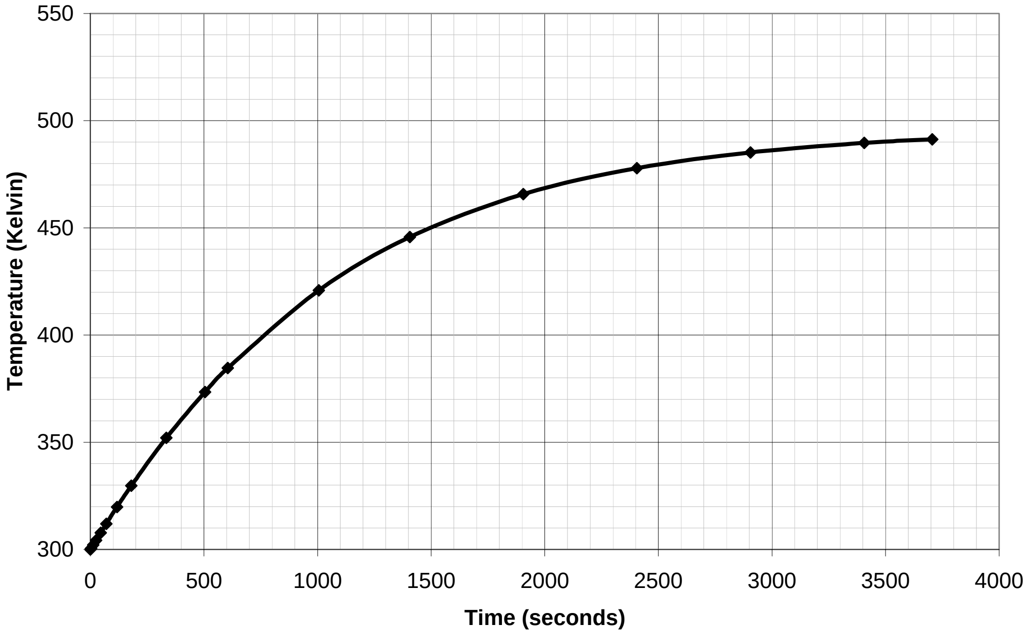

Figure 43: Obstructions average surface temperature: 3D, aspect ratio 1/3, shaft ratio 2/5, and right boundary temperature 500 K

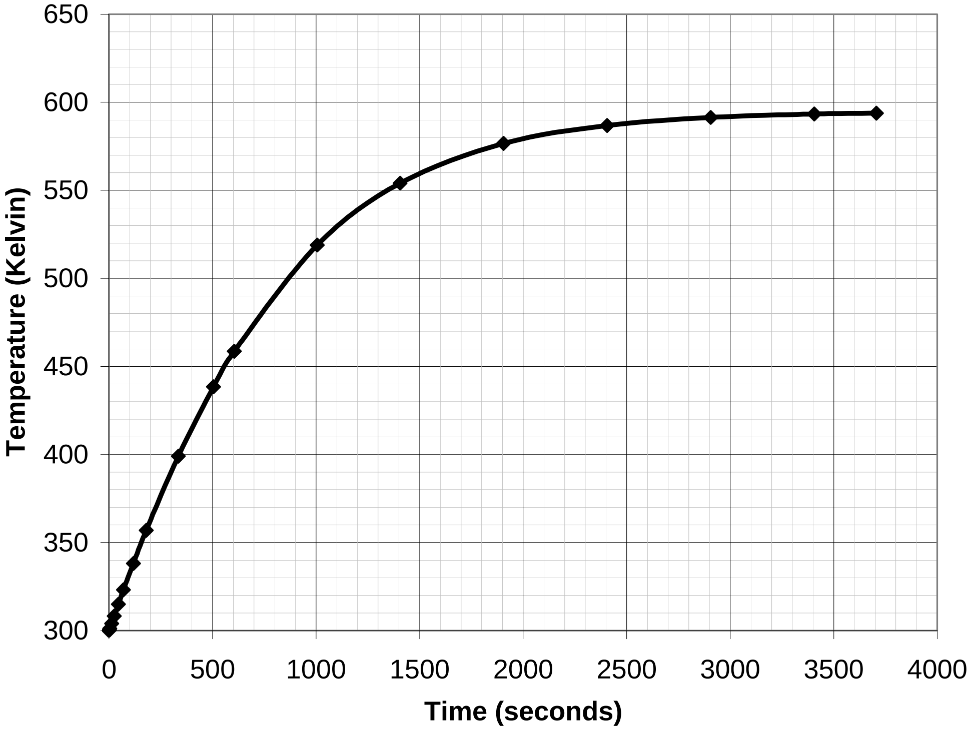

Figure 44: Obstructions average surface temperature: 3D, aspect ratio 1/3, shaft ratio 2/5, and right boundary temperature 600 K

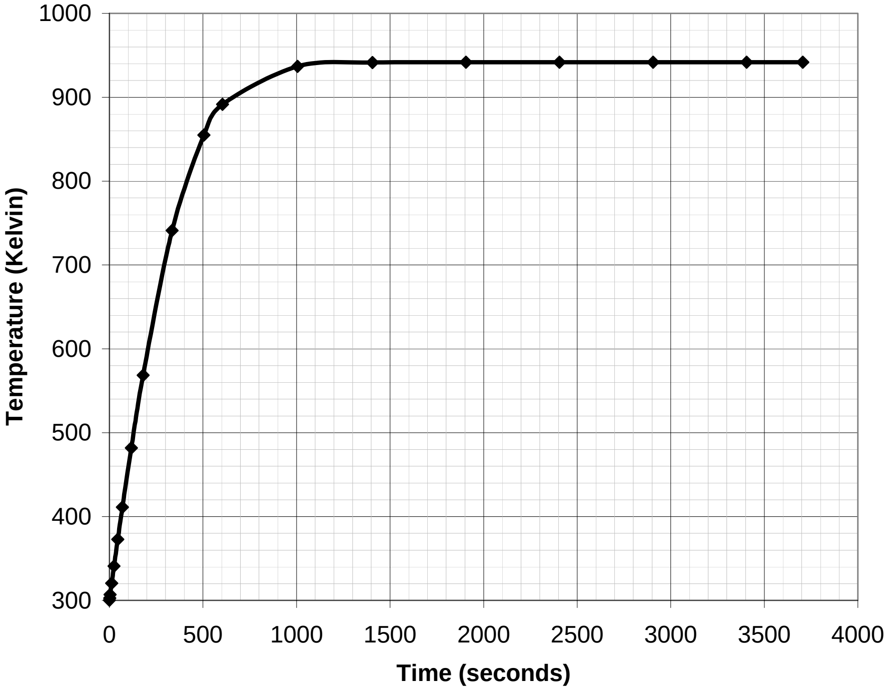

Figure 45: Obstructions average surface temperature: 3D, aspect ratio 1/3, shaft ratio 2/5, and right boundary temperature 950 K

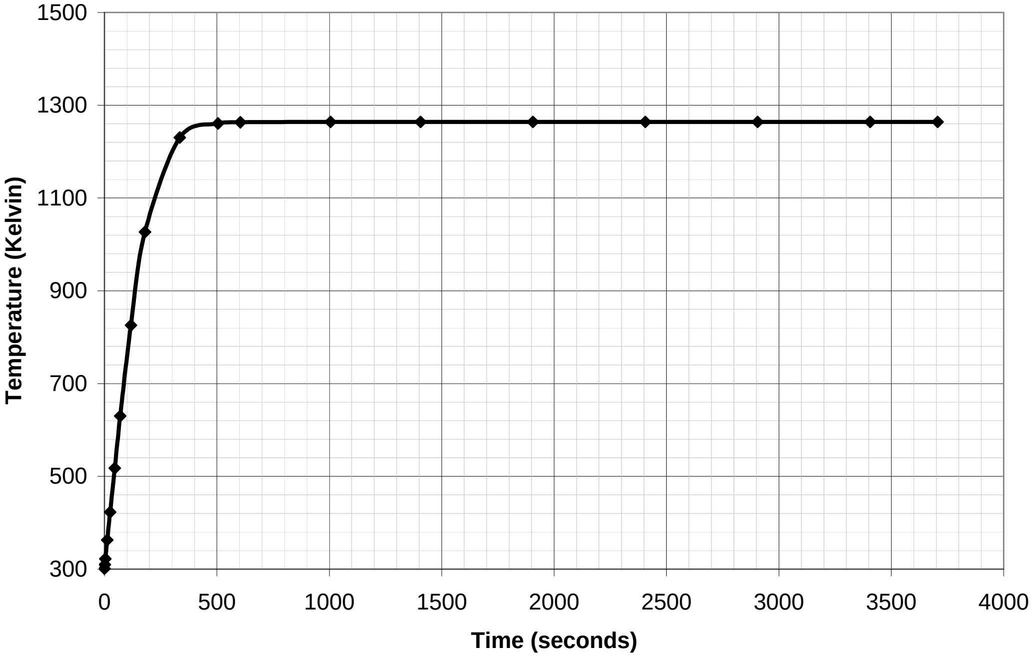

Figure 46: Obstructions average surface temperature: 3D, aspect ratio 1/3, shaft ratio 2/5, and right boundary temperature 1275 K

APPENDIX D

PERCENT RADIATION CONTRIBUTION ON OBSTRUCTION

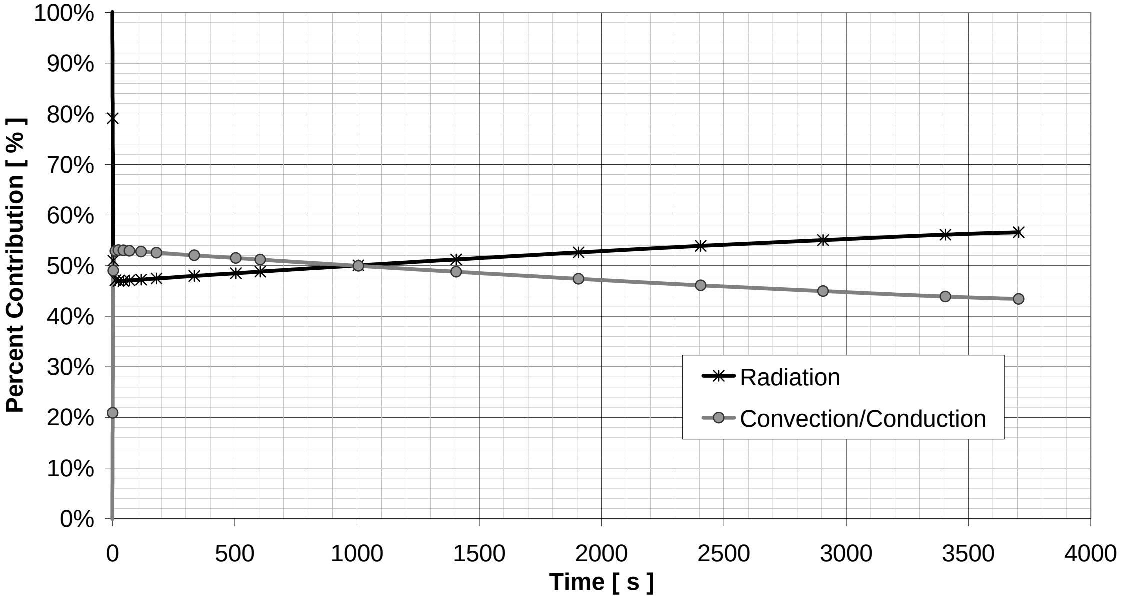

Figure 47: Percent radiation contribution on obstruction: 2D, aspect ratio 1/3, shaft ratio 2/5, and right boundary temperature 310 K

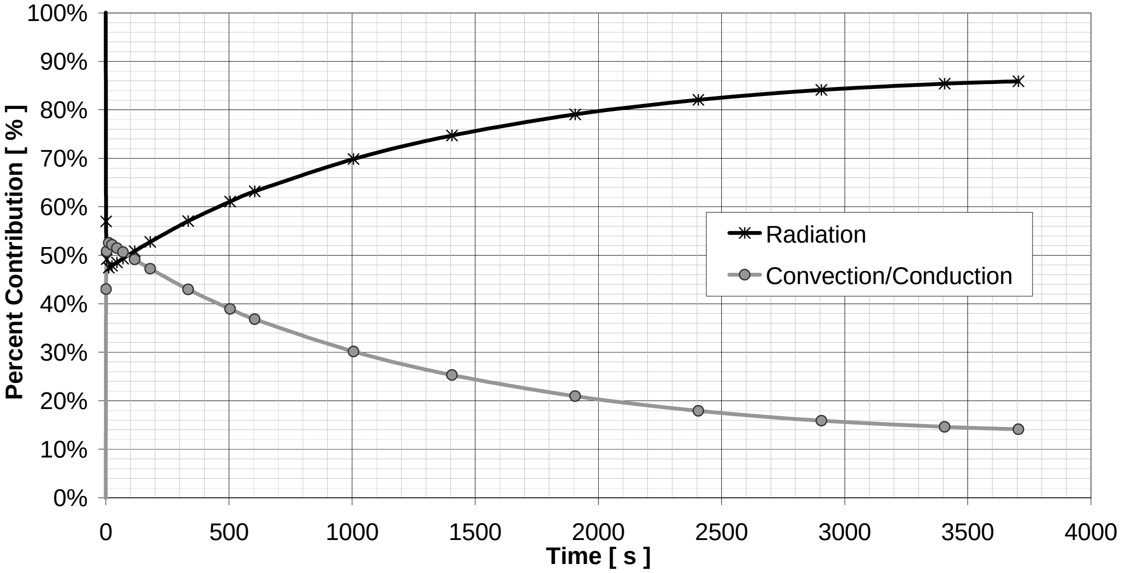

Figure 48: Percent radiation contribution on obstruction: 2D, aspect ratio 1/3, shaft ratio 2/5, and right boundary temperature 500 K

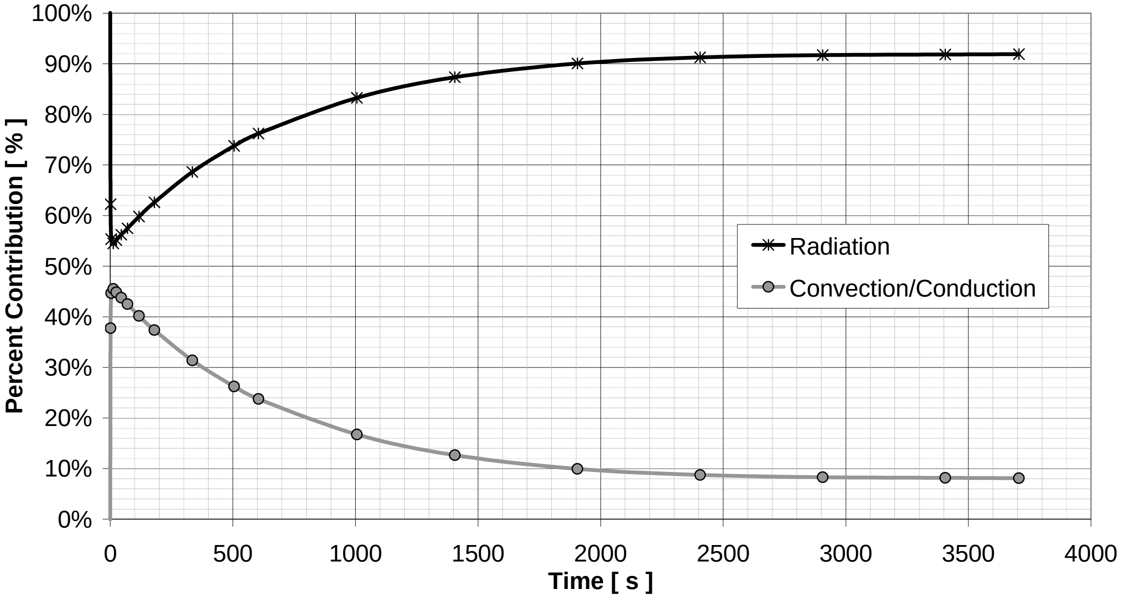

Figure 49: Percent radiation contribution on obstruction: 2D, aspect ratio 1/3, shaft ratio 2/5, and right boundary temperature 600 K

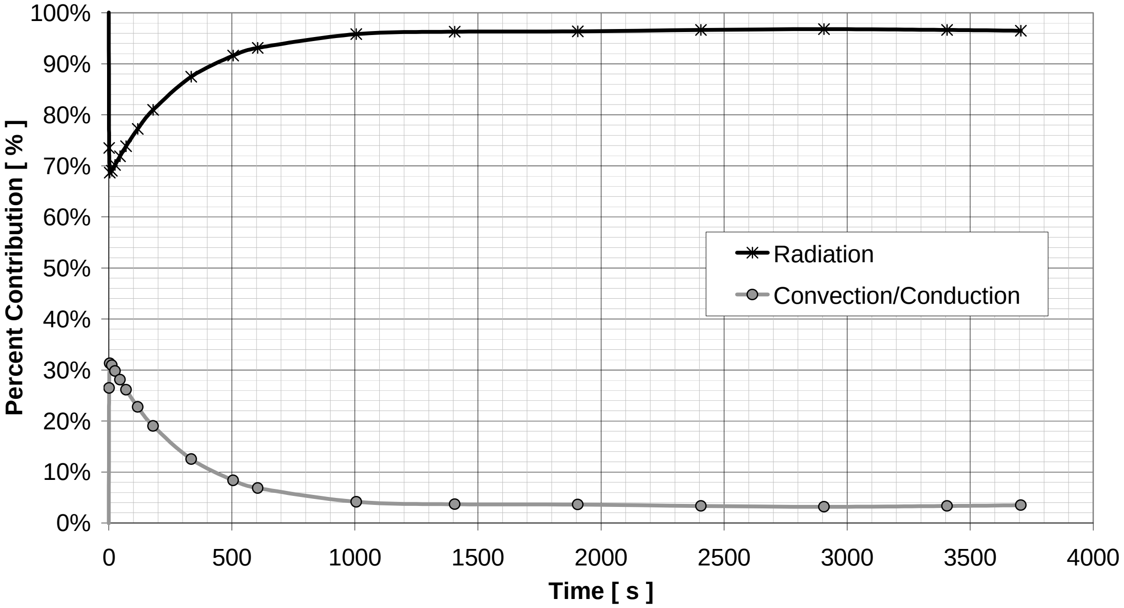

Figure 50: Percent radiation contribution on obstruction: 2D, aspect ratio 1/3, shaft ratio 2/5, and right boundary temperature 800 K

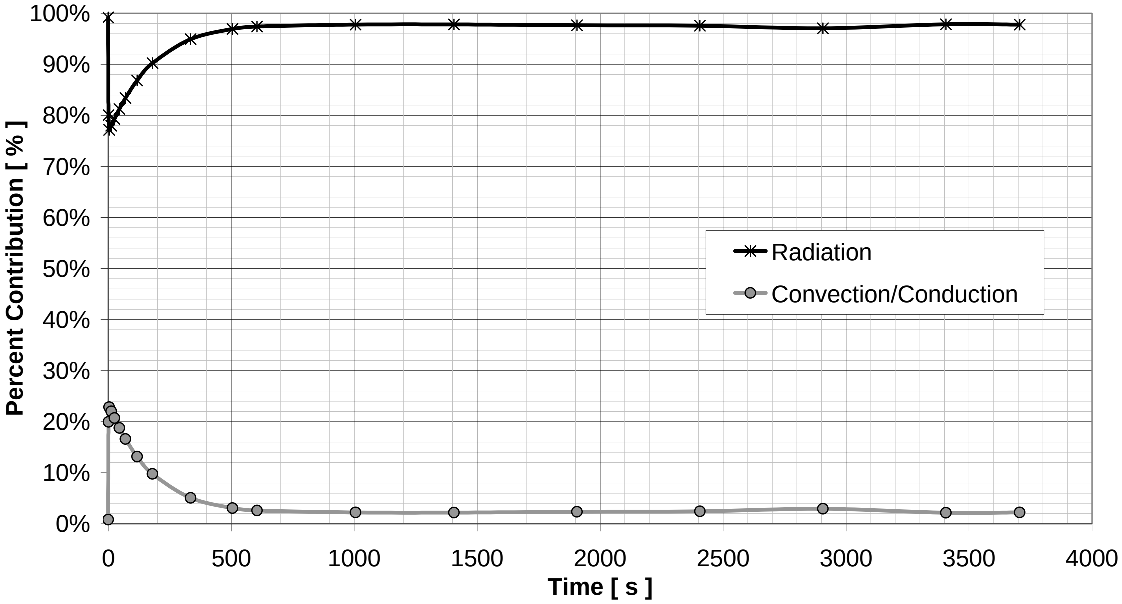

Figure 51: Percent radiation contribution on obstruction: 2D, aspect ratio 1/3, shaft ratio 2/5, and right boundary temperature 950 K

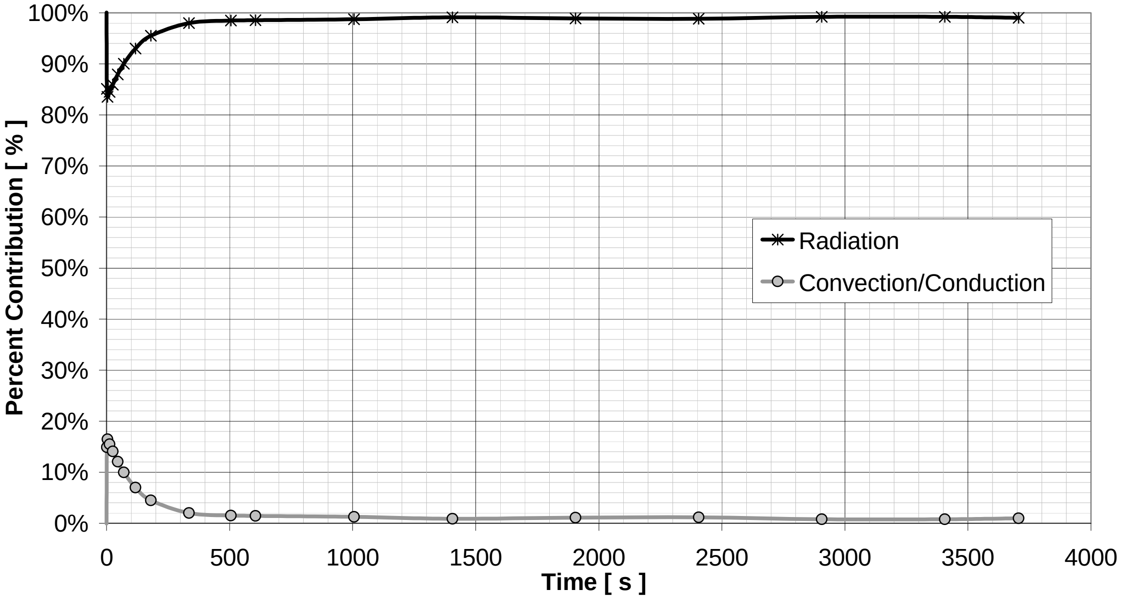

Figure 52: Percent radiation contribution on obstruction: 2D, aspect ratio 1/3, shaft ratio 2/5, and right boundary temperature 1100 K

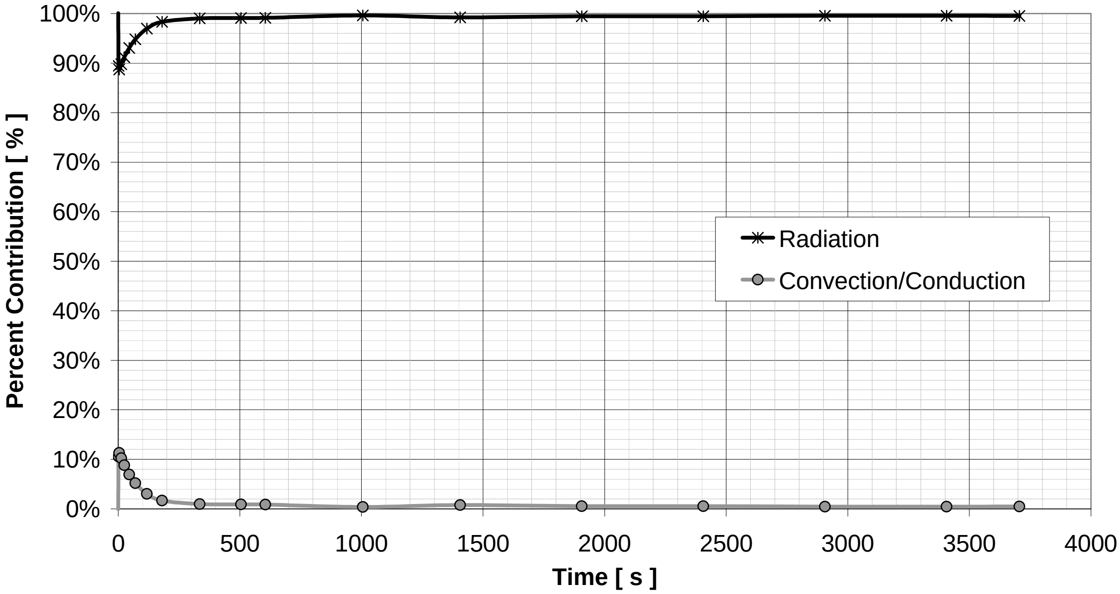

Figure 53: Percent radiation contribution on obstruction: 2D, aspect ratio 1/3, shaft ratio 2/5, and right boundary temperature 1275 K

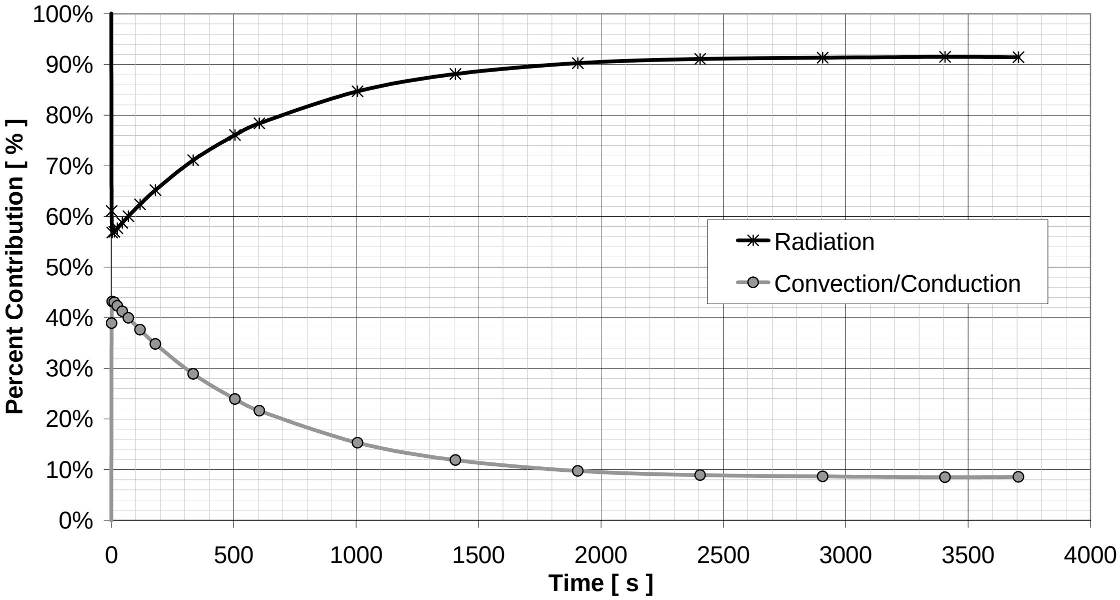

Figure 54: Percent radiation contribution on obstruction: 2D, aspect ratio 1/2, shaft ratio 2/5, and right boundary temperature 600 K

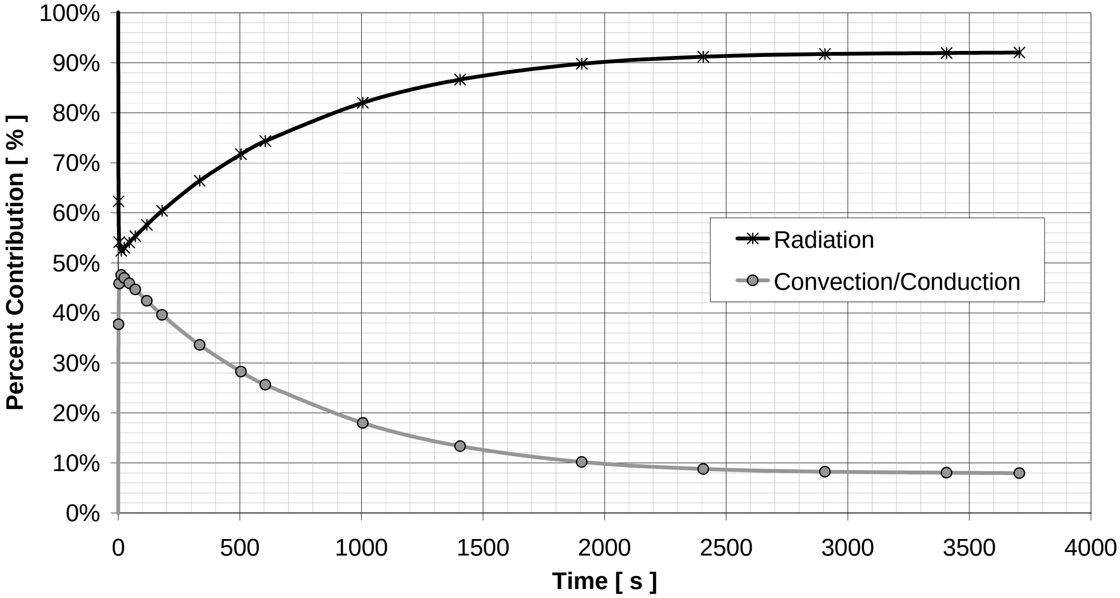

Figure 55: Percent radiation contribution on obstruction: 2D, aspect ratio 1/4, shaft ratio 2/5, and right boundary temperature 600 K

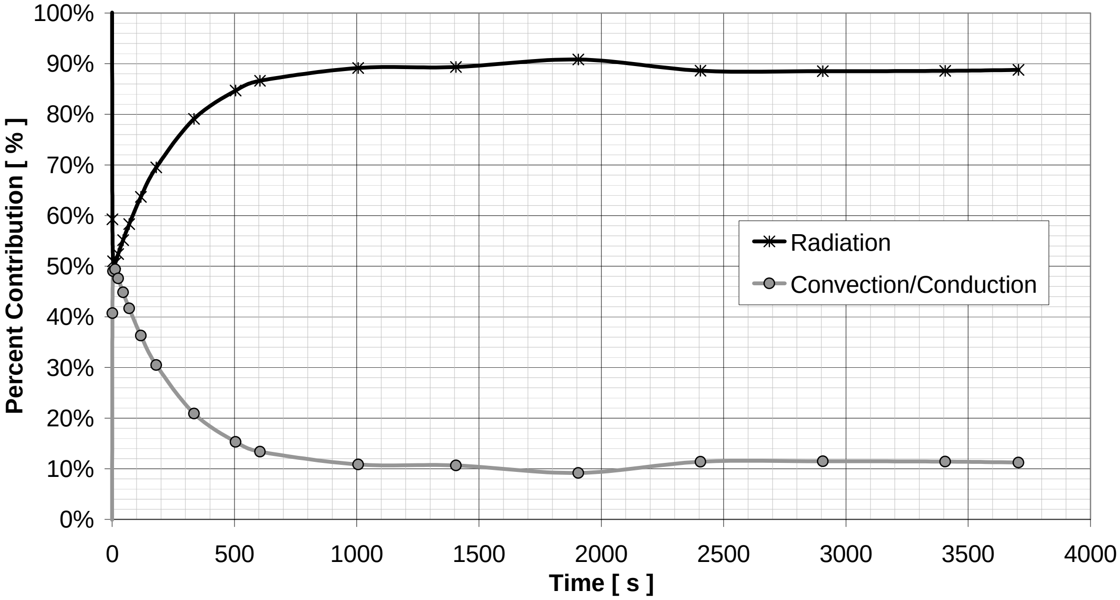

Figure 56: Percent radiation contribution on obstruction: 2D, aspect ratio 1/3, shaft ratio 1/5, and right boundary temperature 600 K

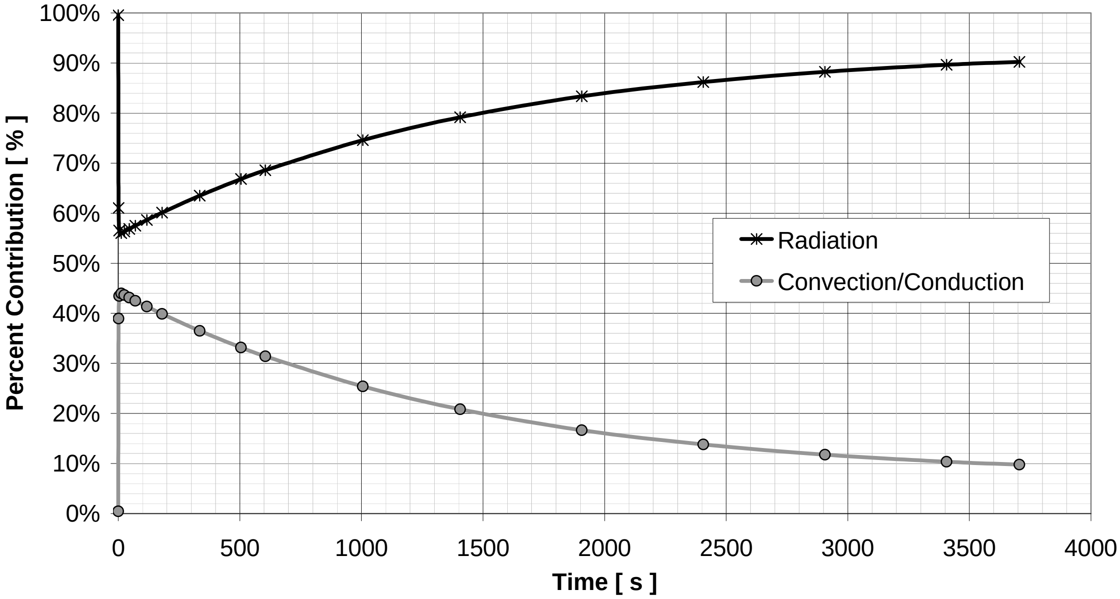

Figure 57: Percent radiation contribution on obstruction: 2D, aspect ratio 1/3, shaft ratio 3/5, and right boundary temperature 600 K

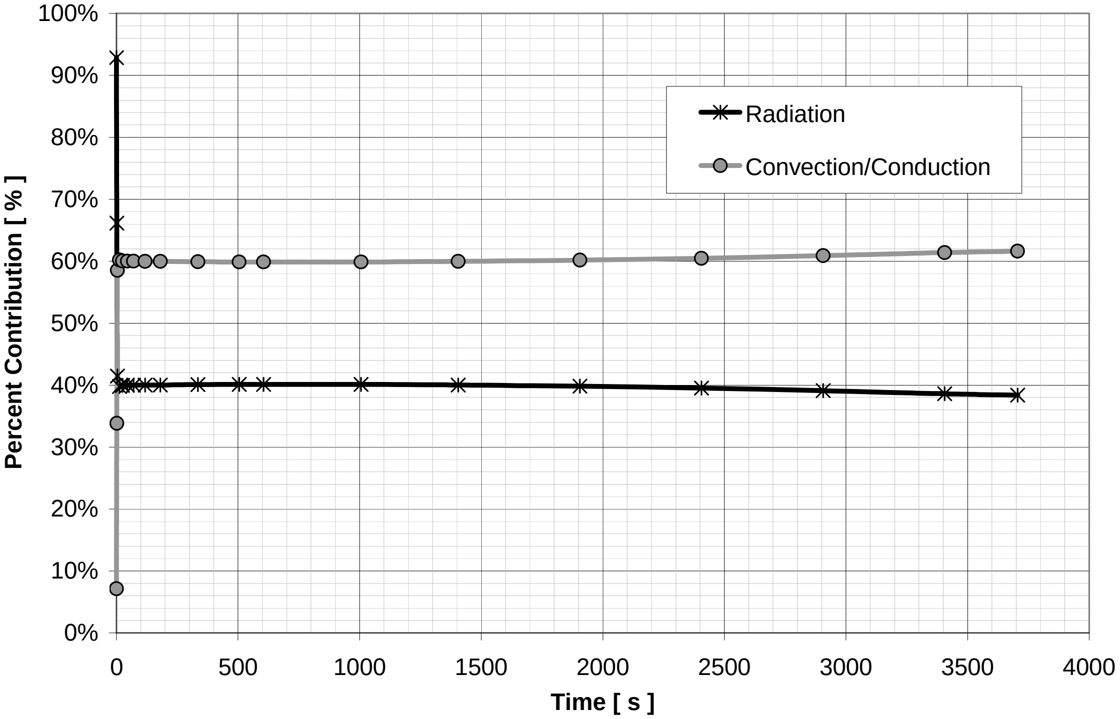

Figure 58: Percent radiation contribution on obstruction: 3D, aspect ratio 1/3, shaft ratio 2/5, and right boundary temperature 310 K

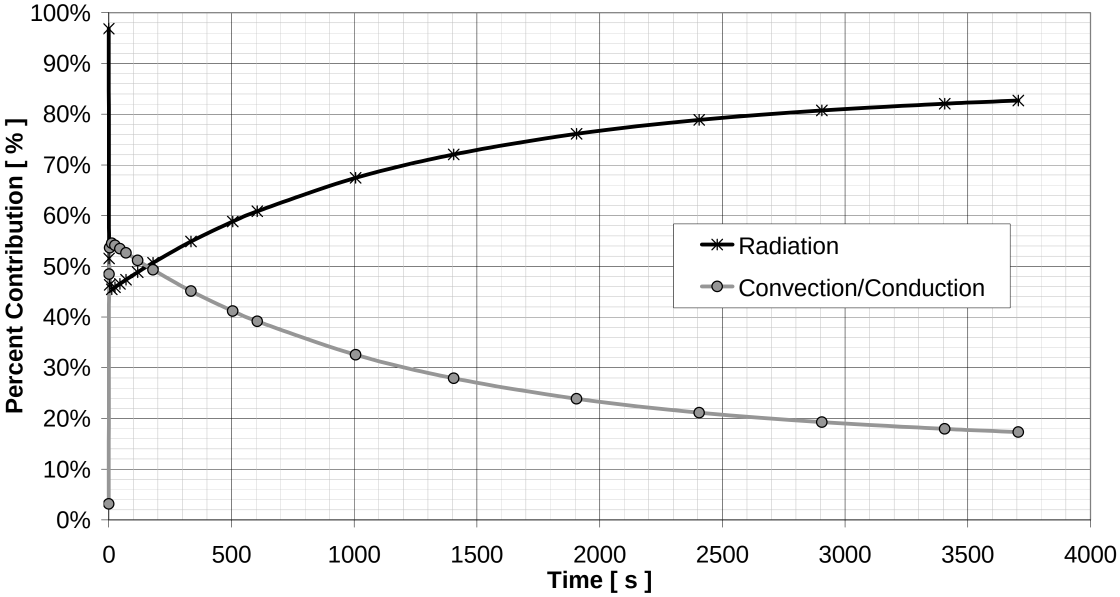

Figure 59: Percent radiation contribution on obstruction: 3D, aspect ratio 1/3, shaft ratio 2/5, and right boundary temperature 500 K

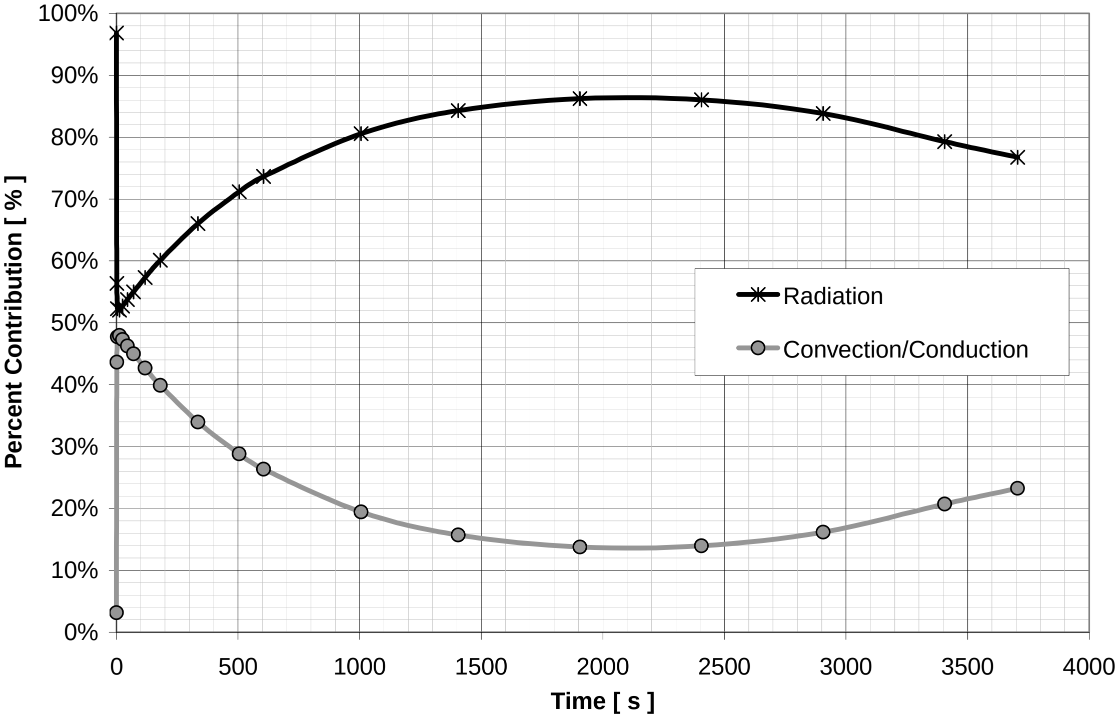

Figure 60: Percent radiation contribution on obstruction: 3D, aspect ratio 1/3, shaft ratio 2/5, and right boundary temperature 600 K

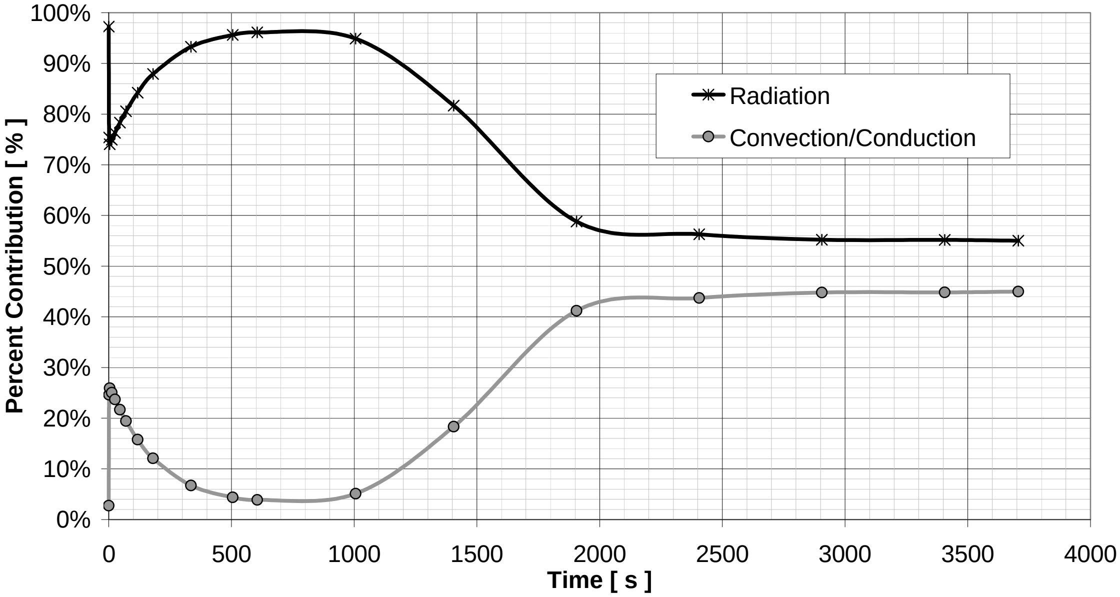

Figure 61: Percent radiation contribution on obstruction: 3D, aspect ratio 1/3, shaft ratio 2/5, and right boundary temperature 950 K

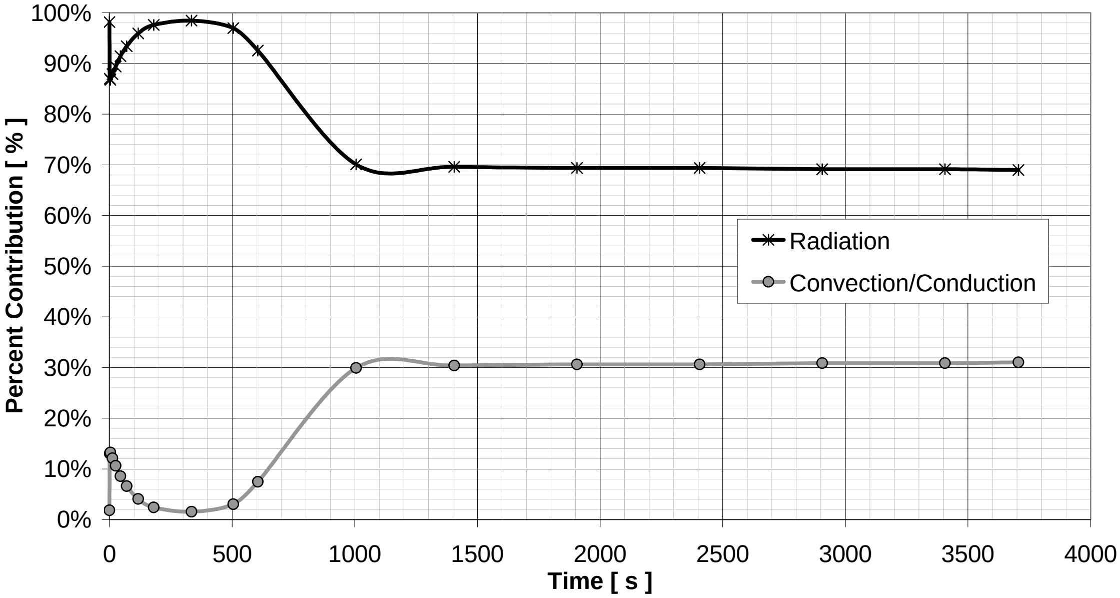

Figure 62: Percent radiation contribution on obstruction: 3D, aspect ratio 1/3, shaft ratio 2/5, and right boundary temperature 1275 K

VITA

Jimmy L. Lloyd entered Texas A&M University in August 1997 to work on a Bachelor of Science degree in mechanical engineering. In December 2001, he was awarded the B.S. degree, Summa Cum Laude and Texas A&M Engineering Scholar Program honors. Work on his M.S. degree in mechanical engineering began in January 2002. He received his degree in December 2003. While at A&M, Mr. Lloyd has had the opportunity to work for a variety of companies and industries such as Ford Motor Company, Schlumberger, and Sandia National Laboratories. His permanent address is 2048 FM 812 Dale, TX 78616.